



國立中山大學材料科學研究所

碩士論文

金基塊狀非晶質合金機械性質與微成形能力之探討

Mechanical Properties and Micro-Forming Ability of Au-Based
Bulk Metallic Glasses

研究生：湯振緯 撰

指導教授：黃志青 博士

中華民國 九十七 年 七 月

國立中山大學研究生學位論文審定書

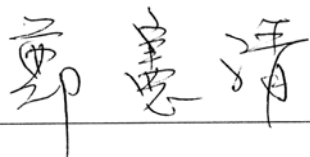
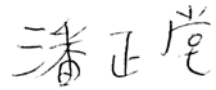

本校材料科學研究所碩士班

研究生湯振緯（學號：M963060006）所提論文

金基塊狀非晶質合金機械性質與微成形能力之探討
Mechanical Properties and Micro-Forming Ability of Au-based
Bulk Metallic Glasses

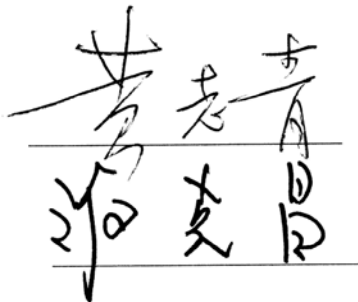
經本委員會審查並舉行口試，符合碩士學位論文標準。

學位考試委員簽章：

	 
_____	_____
_____	_____
_____	_____

指導教授

系主任/所長



致謝

五年前的夏天，回憶的片段像口試時撥放的投影片，沒有翻箱倒櫃地搜尋，靜靜地從五樓材料所的陽台向外望去，蔚藍的海洋逐著波浪，白色的燈塔就輕輕地架起了投影機，把一切毫無保留地投影在心頭。和西子灣的邂逅，那是一個萬里無雲的好日子，就像任何一天高雄的夏日，陽光刺著雙眼，讓你不得不謙卑地低頭避開那遠從一百五十萬公里來的強力射線，激烈地核融合反應似乎狂妄地想把所有的海水蒸發。凝視著母親，她似乎還沒有從唯一的犬子要離鄉背井負笈高雄的不捨中釋懷，這樣的相遇可不比李白詩中對西施的描寫「出自苧蘿山。秀色掩古今，荷花羞玉顏。」那般富有情治詩意，倒是這句「皓齒信難開，沉吟『豔陽』間」，貼切地描寫著當時的心境。

「阿湯，你快要畢業了」當我把論文初稿交給黃老師志青時，他和緩並帶著他慣有的微笑對我這麼說道，不知怎麼地突然紅了眼眶，隔著一層鏡片，鏡片上映著的是無數材料相關的書籍和達文西最後的晚餐，老師充滿慧黠又慈祥的瞳仁在哪瞬間溫柔地把時間給凝住了。五年間發生了很多事，球場上的汗水，工廠電弧滿目瘡痍的銅坩堝，海堤旁的空啤酒罐，遺留在沙灘上的腳印，停留在月色的髮香，躺在E棟四二零宿舍的友情碎片，滴在西裝外套上男人間的感情和難過，這一切的一切都默默地存在腦中，直到老師的話語像晶種般，引發一連串的晶粒成長恣意地蔓延，在西子灣的無限柔情的懷裡慢慢地沈澱靜置。

生命是由生活的篇章所構成的，這一千八百多個日子，謝謝黃老師志青和材料所的每一位老師帶領學生認識材料科學之美，在學生的心中灑下神的種子，還有師母在每一個星期天早晨樂以教和，讓詩歌悠揚的音符縈繞我心。義守大學風趣幽默的鄭老師憲清，讓敝人的研究和日本、西安之行格外精彩豐富。機械所的潘老師正堂提供實驗和口試的指導。地下所長，千杯不醉的華大哥應麒，系辦三朵花朱小姐惠敏，顏小姐秀芳，陳小姐秀玉，溫情的照顧。

感謝黃幫的所有成員，瀋陽第一名的博士後研究杜博士興蒿。黃幫楷模，研究精神

滿分的敬仁學長。比孤狗大神還神的博士雞排店店長，智多星育誠學長。嚴謹認真扣子總是扣得很好的志溢學長。個性恬淡，具有客家「硬頸」精神，打死不結婚的的子翔學長猴爺。一直擔心禿頭立志取小二十歲老婆的優秀 BMG VI 最佳論文得主 MD 模擬達人友杰學長。人見人愛，開朗熱心一百分，佛羅里達台灣同學會會長宇庭學長。從大專生研究就給予敝人指導，熱心搞笑有活力的海明學長。好好先生，個性溫和總有削不完 pillar 的炎輝學長。有敬仁學長般研究熱血，不吃青菜的泡麵攝影達人鴻昇學長。專業籃球 C 級裁判，講話中肯犀利，連續當了敝人兩次學長的浩然學長。內斂實在，韜光養晦之術值得敝人效法的名哲學長。瘦身之後定能恢復往日排球身手，直升博士班的巧克力男孩哲男同學。辯才無礙稱霸兩岸，在上海街頭直接跳起街舞，一直很想紅的大豪同學。台灣第一深情，中秋應景水果愛好者，做事很帶勁的碩陽學弟。捲毛都不捲毛，英文嚇嚇叫的柏佑學弟。拿書香獎如一塊小蛋糕一般的逸志學弟。材光系所有的同學和學弟們。還有我親愛的家人們無限的支持，跟思華在線上的支持讓我在寫作論文時可以當個快樂的陽光宅男，站在巨人的肩膀上，有你們的陪伴持讓我的生命更為豐盈精彩。

朋友對我說道：「要畢業了，應該很高興吧！」我什麼也沒說，回以一個似笑非笑的表情，記得優子曾經這樣告訴我：「每一次分離，一部份的你也將死去」心中的一股惆悵，抑鬱在心中吐也吐不掉，只想用快切把胸口切開讓西子灣的水帶走這份感傷，就像她把貨輪帶走一般，送到世界的其他角落。我沒有像徐志摩那般不帶走一片雲彩的灑脫，但願敝人無盡的思念能讓緣分感應到我真摯的情感，讓我們得以再次相聚，就像神又把敬仁和宇庭學長再次送到我們身邊。人生是一連串的選擇，我很驕傲地說我做了一個美麗的決定，留在黃幫，駐足西子灣。



湯振緯 謹誌

於 國立中山大學材料科學研究所

中華民國九十七年七月

Content

Content.....	i
Tables List.....	iv
Figures List.....	v
Abstract.....	xi
Chapter 1 Introduction.....	1
1.1 Amorphous metallic alloys	1
1.2 The evolution of Au-based amorphous alloys	1
1.3 The motivation of this research.....	2
Chapter 2 Background and literature review	4
2.1 The developments of bulk metallic glasses (BMGs)	4
2.2 Thermal stability and glass forming ability of BMGs	6
2.3 Mechanical behavior of amorphous metallic alloys	9
2.3.1 Deformation mechanisms	9
2.3.2 Shear bands	13
2.3.3 Size effects in plasticity	15
2.4 Comparison between metallic glasses and engineering materials	16
2.5 The birth of Au-based BMG ($\text{Au}_{49}\text{Ag}_{5.5}\text{Pd}_{2.3}\text{Cu}_{26.9}\text{Si}_{16.3}$).....	18
2.6 The parameters to distinguish plasticity or brittleness.....	20
2.7 Applications of bulk metallic glasses	21
2.7.1 Golf club heads	21
2.7.2 Cases for consumer electronics.....	22
2.7.3 Liquidmetal rebounds	23
2.7.4 Medical applications	23
2.7.5 Defense and aerospace.....	24

2.8	Viscous flow behavior	24
Chapter 3	Experimental procedures.....	26
3.1	Materials	26
3.2	Sample preparation	26
3.2.1	Arc melting	26
3.2.2	Suction casting.....	27
3.2.3	Micro-sample fabrication using Focused Ion Beam milling.....	27
3.3	Property measurements and analyses.....	28
3.3.1	X-ray diffraction	28
3.3.2	Qualitative and Quantitative constituent analysis.....	28
3.3.3	DSC thermal analysis.....	28
3.3.4	Density measurement.....	29
3.3.5	TMA analysis.....	29
3.3.6	Micro-hardness testing.....	30
3.3.7	Macro-compression testing.....	30
3.3.8	Micro-compression testing.....	30
3.3.9	Microstructure examination	31
3.3.10	Hot embossing of micro-lens and V-groove	31
3.3.11	Surface morphologies	32
Chapter 4	Results.....	33
4.1	Sample preparations.....	33
4.2	XRD analyses.....	33
4.3	SEM/EDS observations	33
4.4	TEM observations.....	33
4.5	DSC analyses	34
4.6	Density measurement.....	34

4.7	Micro-hardness testing.....	35
4.8	Macro-compression testing.....	35
4.9	Compressive fracture characteristics	36
4.10	Micro-compression testing.....	37
4.11	TMA Analysis.....	38
4.12	Hot embossing of V-groove on Au-based BMG	39
4.13	Hot embossing of micro-lens array on Au-based BMG	40
Chapter 5	Discussions.....	42
5.1	Variation in compositions of Au-based BMG	42
5.2	The glass forming ability of Au-based BMG	42
5.3	Bulk and micro-scale compressive behavior of Au-based BMG.....	43
5.4	Viscous flow behavior for Au-based BMG	45
5.5	Hot embossing on Au-based BMG.....	47
Chapter 6	Conclusions.....	50
References.....		52
Tables.....		56
Figures.....		57

Tables List

Table 2.1	Bulk metallic glasses and their developed year [30].	56
Table 2.2	The composition of representative BMG systems, their glass transition temperature T_g , onset temperature of crystallization, T_x , and onset melting point, T_m , and glass forming ability represented by reduced glass transition temperature, T_{rg} [30]. .	57
Table 2.3	Properties of the elements in the Au-based BMG alloy.	58
Table 2.4	Possible application fields for BMGs [30].	59
Table 4.1	The composition analyses of the $Au_{49}Ag_{5.5}Pd_{2.3}Cu_{26.9}Si_{16.3}$ rods by SEM/EDS. ...	60
Table 4.2	Summary of the macro-compressive of Au-based BMG at different strain rates.	61
Table 4.3	Summary of the micro-compressive of Au-based BMG at different strain rates. .	62
Table 4.4	Variation in distance and average height under different conditions for V-groove.	63
Table 4.5	Variation in height and width under different conditions for micro-lens array.....	64
Table 5.1	The negative heat of mixing in unit of kJ/mol of the Au, Ag, Pd, Cu, and Si elements.	65
Table 5.2	Thermal properties of the $Mg_{65}Cu_{25}Gd_{10}$ (Mg-based BMG) and $Au_{49}Ag_{5.5}Pd_{2.3}Cu_{26.9}Si_{16.3}$ (Au-based BMG) obtained from DSC at a heating rate of 10 K/min.	66

Figures List

Figure 2.1	The critical casting thickness versus the year in which alloys were discovered. Over 40 years, the critical casting thickness has increased by more than three orders of magnitude [19].....	67
Figure 2.2	The picture of as-cast alloy BMG system [30].	68
Figure 2.3	Relationship between the critical cooling rate for glass formation (R_c), maximum sample thickness for glass formation (t_{max}) and reduced glass transition temperature (T_g/T_m) for bulk amorphous alloys. The data of the ordinary amorphous alloys, which require high cooling rates for glass formation, are also shown for comparison [31].	69
Figure 2.4	Relationship between R_c , t_{max} and the temperature interval of the supercooled liquid region between T_g and T_x for bulk amorphous alloys [31].	70
Figure 2.5	A comparison of critical cooling rate between reduced glass transition temperature, T_{rg} , among BMG, silicate glasses and conventional metallic glasses [30].	71
Figure 2.6	The correlation between the critical cooling rate and the parameter γ_m for metallic glasses [39].	72
Figure 2.7	Two-dimensional schematics of the atomistic deformation mechanisms proposed for amorphous metals, including (a) a shear transformation zone (STZ), after Argon [40], and (b) a local atomic jump, after Spaepen [50].	73
Figure 2.8	Scanning electron micrographs illustrating the “slip steps” or surface offsets associated with shear bands in deformed metallic glasses. In (a), a bent strip of $Zr_{57}Nb_5Al_{10}Cu_{15.4}Ni_{12.6}$ illustrates slip steps formed in both tensile and compressive modes of loading, on the top and bottom surfaces, respectively. In (b) the side of a compression specimen of $Zr_{52.5}Cu_{17.9}Ni_{14.6}Al_{10}Ti_5$ is shown, for which the loading axis was vertical; here the slip steps document shear	

	deformation at an inclined angle to the applied compressive load [63].	74
Figure 2.9	Calculations from the work of (a) Argon and (b) Steif et al. illustrating the process of strain localization in metallic glasses. In (a), a history of strain rate is shown for both the forming shear band and the surrounding matrix; these quantities are normalized by the applied shear strain rate. In (b), the history of strain in the shear band is shown [51, 64].....	75
Figure 2.10	Examples of mechanical test data that illustrate serrated flow of metallic glasses, through repeated shear band operation in confined loading. In (a), the compression response of a $\text{Pd}_{77.5}\text{Cu}_6\text{Si}_{16.5}$ specimen of low aspect ratio is shown, while (b) is an instrumented indentation curve for $\text{Pd}_{40}\text{Cu}_{30}\text{Ni}_{10}\text{P}_{20}$ glass. Because (a) represents a displacement controlled experiment, serrations are represented as load drops, while the load-controlled experiment in (b) exhibits displacement bursts [65].	76
Figure 2.11	Average shear band spacings are plotted as a function of characteristic specimen dimensions for a variety of metallic glasses (and some derivative composites) deformed in constrained modes of loading, after Conner et al [67].	77
Figure 2.12	Amorphous metallic alloys combine higher strength than crystalline metal alloys with the elasticity of polymers [19]......	78
Figure 2.13	Elastic limit σ_y plotted against modulus E for 1507 metals, alloys, metal matrix composites and metallic glasses. The contours show the yield strain σ_y / E and the resilience σ_y^2 / E [73].	79
Figure 2.14	Resilience σ_y^2 / E and loss coefficient for the same materials as Figure 2.13 [73].	80
Figure 2.15	Fracture toughness and modulus for metals, alloys, ceramic, glasses, polymers and metallic glasses. The contours show the toughness G_c in kJ m^{-2} [73].	81
Figure 2.16	Toughness and elastic limit for the same materials. The contours show the	

process-zone size d in mm [73].	82
Figure 2.17 Composition dependence of ΔT and d_c for $(\text{Au}_{58.5}\text{Ag}_{6.6}\text{Pd}_{2.8}\text{Cu}_{32.1})_{86-x}\text{Si}_{14+x}$ for $x = 0-6\%$. A strong dependence on the Si content of both d_c and ΔT is observed. No obvious correlation of d_c and ΔT is seen [9].	83
Figure 2.18 Position dependence of ΔT and d_c for $(\text{Au}_{60.1}\text{Ag}_{6.8}\text{Cu}_{33.1})_{83.7-y}\text{Pd}_y\text{Si}_{16.3}$ for $y = 0-5\%$. A strong dependence on the Pd content of both d_c and ΔT is observed. No obvious correlation of d_c and ΔT is seen [9].	84
Figure 2.19 The relationship between v and μ/β .	85
Figure 2.20 The correlation of fracture energy G with elastic modulus ratio μ/B for all the as-cast (unannealed) metallic glasses for which relevant data are available (all compositions in at.%). Elastic constants were used to convert fracture toughness to fracture energy [79].	86
Figure 2.21 The correlation of fracture energy G with Poisson's ratio for all the data collected on metallic glasses (as-cast and annealed) as well as for oxide glasses [79].	87
Figure 3.1 Au-BMG micropillars fabricated by focus ion beam technique: (a) 1 μm in diameter and (b) 3.8 μm in diameter.	88
Figure 3.2 FIB-SEM micrographs of the flat-punch tip: a) top view and (b) side view.	89
Figure 3.3 Triangle marks made by flat punch	90
Figure 3.4 Hot embossing set-up for oil hydraulic system [92].	91
Figure 3.5 Ni-Co mold with gapless hexagonal micro-lens array. [92].	92
Figure 3.6 Profile of V-groove mold.	93
Figure 4.1 The appearance of the Au-based BMG rods with 2 and 3 mm.	94
Figure 4.2 XRD pattern of the 3 mm and 2 mm Au-based amorphous alloys.	95
Figure 4.3 TEM diffraction pattern of the 3 mm diameter Au-based BMG.	96
Figure 4.4 DSC plot of Au-based amorphous alloy with the heating rate of 40 K/ min.	97
Figure 4.5 The Au-Cu binary phase diagram.	98

Figure 4.6	DSC plot of Au-based amorphous alloy with the heating rate of 10 K/min.	99
Figure 4.7	The compressive stress-strain curves for the $\text{Au}_{49}\text{Ag}_{5.5}\text{Pd}_{2.3}\text{Cu}_{26.9}\text{Si}_{16.3}$ BMG..	100
Figure 4.8	The outer appearance showing fracture plan inclination of the Au-based BMG with a strain rate of $5 \times 10^{-5} \text{ s}^{-1}$	101
Figure 4.9	The fracture surface morphology of the Au-based BMG with a strain rate of $5 \times 10^{-5} \text{ s}^{-1}$	101
Figure 4.10	The fracture surface morphology of the Au-based BMG with a strain rate of $5 \times 10^{-5} \text{ s}^{-1}$	102
Figure 4.11	The outer appearance showing fracture plan inclination of the Au-based BMG with a strain rate of $1 \times 10^{-4} \text{ s}^{-1}$	103
Figure 4.12	The fracture surface morphology of the Au-based BMG with a strain rate of $1 \times 10^{-4} \text{ s}^{-1}$	103
Figure 4.13	The fracture surface morphology of the Au-based BMG with a strain rate of $1 \times 10^{-4} \text{ s}^{-1}$	104
Figure 4.14	The outer appearance showing fracture plan inclination of the Au-based BMG with a strain rate of $5 \times 10^{-4} \text{ s}^{-1}$	105
Figure 4.15	The fracture surface morphology of the Au-based BMG with a strain rate of $5 \times 10^{-4} \text{ s}^{-1}$	105
Figure 4.16	The fracture surface morphology of the Au-based BMG with a strain rate of $5 \times 10^{-4} \text{ s}^{-1}$	106
Figure 4.17	The outer appearance showing fracture plan inclination of the Au-based BMG with a strain rate of $1 \times 10^{-3} \text{ s}^{-1}$	107
Figure 4.18	The outer appearance showing fracture plan of the Au-based BMG with strain a rate of $1 \times 10^{-3} \text{ s}^{-1}$	107
Figure 4.19	The outer appearance of the Au-based BMG with a strain rate of $1 \times 10^{-3} \text{ s}^{-1}$...	108
Figure 4.20	The fracture surface morphology of the Au-based BMG with a strain rate of	

	$1 \times 10^{-3} \text{ s}^{-1}$	108
Figure 4.21	The fracture surface morphology of the Au-based BMG with a strain rate of $1 \times 10^{-3} \text{ s}^{-1}$	109
Figure 4.22	Compression load-displacement curves of the 1 μm Au-BMG at different strain rates.	110
Figure 4.23	Compression load-displacement curves of the 3.8 μm Au-BMG at different strain rates.	111
Figure 4.24	Time-and-displacement curves for the 1 μm Au BMG pillars.	112
Figure 4.25	Time-and-displacement curves for the 3.8 μm Au BMG pillars.	113
Figure 4.26	SEM micrographs showing the appearance of deformed pillars: (a) 3.8 μm , $\sim 1 \times 10^{-3} \text{ s}^{-1}$, (b) 3.8 μm , $\sim 1 \times 10^{-2} \text{ s}^{-1}$, (c) 3.8 μm , $\sim 6 \times 10^{-2} \text{ s}^{-1}$, (d) 1 μm , $\sim 1 \times 10^{-3} \text{ s}^{-1}$, (e) 1 μm , $\sim 1 \times 10^{-2} \text{ s}^{-1}$, and (f) 1 μm , $\sim 6 \times 10^{-2} \text{ s}^{-1}$	114
Figure 4.27	Typical TMA and DTMA curves measured at stress level of 7.1 kPa for the as-cast bulk Au-based BMG.	117
Figure 4.28	Measured viscosities of the Au-based and Mg-based BMG in the supercooled liquid region at a heating rate 10 K/min.	118
Figure 4.29	Replicated patterns by OM on the Au-based BMG materials imprinted at 177°C and 137 MPa for 1 min with (a) lower magnification by OM (b) higher magnification.	119
Figure 4.30	Replicated patterns by OM on the Au-based BMG materials imprinted at 177°C and 137 MPa for 5 min with (a) lower magnification by OM (b) higher magnification.	120
Figure 4.32	Replicated patterns by OM on the Au-based BMG materials imprinted at 177°C and 62 MPa for 10 min with (a) lower magnification by OM (b) higher magnification.	122
Figure 4.33	Replicated patterns by OM on the Au-based BMG materials imprinted at 177°C	

	and 156 MPa for 10 min with (a) lower magnification by OM (b) higher magnification.	123
Figure 4.34	The morphological curves of V-groove imprinted Au-based BMG at 177°C and 62 MPa, 137 MPa, and 156 MPa, respectively, for 10 min by the α step.	124
Figure 4.35	The morphological curves of V-groove imprinted Au-based BMG at 177°C and 137 MPa for 1, 5, 10 min, respectively, by the α step.	125
Figure 4.36	Replicated patterns by OM on the Au-based BMG materials imprinted at 177°C and 28 MPa for 10 min.	126
Figure 4.37	Replicated patterns by OM on the Au-based BMG materials imprinted at 177°C and 62 MPa for 10 min with (a) lower magnification (b) higher magnification	127
Figure 4.38	Replicated patterns by OM on the Au-based BMG materials imprinted at 177°C and 156 MPa for 10 min with (a) lower magnification (b) higher magnification	128
Figure 4.39	The morphological curves of micro-lens array on the Au-based BMG at 177°C and 28 MPa, 62 MPa, and 156 MPa, respectively, for 10 min by the α step. .	129
Figure 4.40	Replicated patterns by SEM on the Au-based BMG materials imprinted at 177°C and 156 MPa for 10 min with (a) lower magnification (b) higher magnification.	130
Figure 5.1	The strength-sample size relationship for the Au-based BMG with different pillar diameters from 2 mm down to 1 μ m.	131
Figure 5.2	Determination of the STZ size of the Au-based alloys based on the TMA data.	132
Figure 5.3	Extraction of the activation energy of the Au-based BMG during shear deformation within the supercooled temperature region.	133
Figure 5.4	XRD pattern of the hot embossing Au-based BMG with different pressures 62 MPa, 137 MPa, and 156 MPa, respectively.	134

Abstract

The mechanical properties and micro-forming of the Au-based bulk metallic glasses are reported in this thesis. The original ingots were prepared by arc melting and induction melting. The $\text{Au}_{49}\text{Ag}_{5.5}\text{Pd}_{2.3}\text{Cu}_{26.9}\text{Si}_{16.3}$ bulk metallic glasses with different diameters 2 and 3 mm were successfully fabricated by conventional copper mold casting in an inert atmosphere. By the observation of transmission electron microscopy diffraction pattern, there are crystalline phases among the amorphous matrix phase.

The $\text{Au}_{49}\text{Ag}_{5.5}\text{Pd}_{2.3}\text{Cu}_{26.9}\text{Si}_{16.3}$ bulk metallic glass shows the high glass forming ability and good thermal stability. By the Differential scanning calorimetry (DSC) results, the values of ΔT_x and ΔT_m are 50 and 21 K. And T_{rg} , γ , and γ_m values for the $\text{Au}_{49}\text{Ag}_{5.5}\text{Pd}_{2.3}\text{Cu}_{26.9}\text{Si}_{16.3}$ bulk metallic glass (BMG) at the heating rate of 0.67 K/s are 0.619, 0.430 and 0.774, respectively.

The mechanical properties of $\text{Au}_{49}\text{Ag}_{5.5}\text{Pd}_{2.3}\text{Cu}_{26.9}\text{Si}_{16.3}$ in terms of compression testing are examined using an Instron 5582 universal testing machine. Room temperature compression tests are conducted on specimens with various strain rates. To know the size effect, the micro-pillars were made by using a focus ion beam (FIB) technique. The micro-pillars were under the tests of compression at different strain rates, compared with macro-scale 2 mm rod specimens. In contrast to the brittle fracture in a bulk sample, these micro-pillar specimens show significant plasticity. The morphology of compressed pillar samples indicates that the number of shear bands increased with the sample size and strain rates.

論文摘要

本實驗為金基塊狀非晶質合金之機械性質及微成形能力之研究。 $\text{Au}_{49}\text{Ag}_{5.5}\text{Pd}_{2.3}\text{Cu}_{26.9}\text{Si}_{16.3}$ 合金經由傳統的銅模鑄造方式能夠成功的製作出直徑 2 和 3 mm 的棒材，藉由穿透式電子顯微鏡的觀察，發現其中絕大部分是非晶質，但有些許結晶相分佈在其中。

在熱性質方面， $\text{Au}_{49}\text{Ag}_{5.5}\text{Pd}_{2.3}\text{Cu}_{26.9}\text{Si}_{16.3}$ 非晶質合金顯示出寬的過冷液體區間，顯示其有良好的熱穩定性，另外，根據非晶質合金玻璃形成能力的參考指標，其結果顯示 $\text{Au}_{49}\text{Ag}_{5.5}\text{Pd}_{2.3}\text{Cu}_{26.9}\text{Si}_{16.3}$ 據有良好的玻璃形成能力。

機械性質測試上，以 $\text{Au}_{49}\text{Ag}_{5.5}\text{Pd}_{2.3}\text{Cu}_{26.9}\text{Si}_{16.3}$ 塊狀非晶質合金棒材不同形變速率進行壓縮測試。為了瞭解尺寸大小對材料機械性質的影響，直徑 3.8 微米和 1 微米的試片由聚焦離子束製作，試片經由不同形變速率進行測試，和巨觀直徑 2 mm 的棒材做比較，發現小尺寸的試片具有顯著的延展性，此外，經由外觀形貌觀察，發現當試片大小和形變速率的增加，剪切帶數量也會隨之增加。

藉由熱機械分析儀(TMA)的量測，在熱機性質方面得知在做壓印測試時，攝氏 177 度是其理想的工作溫度，為探討其成行能力，不同的壓力和壓延時間分別進行測試，發現較高的壓力和壓延時間，可獲得較佳的成形能力。金基塊狀非晶質合金優異的抗氧化和成形能力，讓其成為理想的微機電材料。

Chapter 1 Introduction

1.1 Amorphous metallic alloys

Amorphous alloys are metallic materials with a disordered atomic-scale structure. Compared with other metals, which are crystalline and hence have a highly ordered arrangement of atoms, amorphous alloys are non-crystalline. Materials with such a disordered structure formed directly from the liquid state during rapid cooling are called "glasses", and therefore they are commonly referred to as "metallic glasses" or "glassy metals." Still, there are several other methods to fabricate, including physical vapor deposition, solid-state reaction, ion irradiation, melt spinning, and mechanical alloying.

1.2 The evolution of Au-based amorphous alloys

Ever since human history has taken place, people are obsessed with the charm of gold which has high electrical conductivity, high thermal conductivity, and high corrosion resistance. And that is why gold earn the value as the noblest metal on the earth, and plays an incomparable role in the variety of areas such as jewelry, medical, electronics, and so forth. It becomes more exciting after Turnbull estimated the possibility of formation of metallic glass if heterogeneous nucleation could be restrained [1], the metallic glass made its first debut in the composition of $\text{Au}_{75}\text{Si}_{25}$ in 1960 by Clement et al. at Caltech, USA [2]. They developed the rapid quenching techniques to fabricate the metallic liquids at very high rates of 10^5 - 10^6 K/s; however, the high cooling rate limited the metallic glass geometry to thin sheet, below 50 microns. In order to improve the glass forming ability of this alloy, Si was partially replaced by Ge, but the new composition can only moderately increase the glass forming

ability (GFA) and the width of supercooled liquid region [3,4] which is the parameter for processing large supercooled liquid region gives access to a low forming viscosity.

In an effort to fabricate bulk metallic glasses over the last two decades, several alloys based on Pd [5], Fe [6], Pt [7], and so on were successfully formed. And the researchers found out that the intrinsic GFA and critical casting thickness, d_{\max} , were characterized by the critical cooling rate, R_c [8]. In 2005, by the contribution of Schriers et al. [9], gold based amorphous, $\text{Au}_{49}\text{Ag}_{5.5}\text{Pd}_{2.3}\text{Cu}_{26.9}\text{Si}_{16.3}$, gets on the stage once again showing good glass forming ability; furthermore, the maximum cast thickness can exceed 5 mm in the best glass former and the Vickers hardness of the alloy in this system is approximately 350 H_v , twice of conventional 18-karat crystalline gold alloys which are rather soft and vulnerable to be scratched. With those attractive properties, it becomes the potential material for medical, dental, and jewelry applications.

1.3 The motivation of this research

Size effects in the deformation of sub-micro crystalline Au columns have been reported by Volkert et al. [10]. Unlike in bulk materials, dislocations inside small crystals can travel only small distance before annihilating at the free surface and have little chance for multiplication, leading to dislocation starvation [11]. For the crystalline materials, the dislocation density is expected to be lower in the small pillars due to the loss of dislocations through the sample surface, the applied stress required to nucleate or activate dislocation sources can be argued to increase with decreasing column diameter. However, for the short-range ordered materials, bulk metallic glasses, the model should be another story. To explore this newly invented bulk metallic glass (BMG) material and its size effects, we fabricate a few 2mm Au-based rods with the same composition as reported by Schriers et al.

From the cast glassy rods, the micro-scale pillar specimens are made and subject to compression experiments to research their mechanical response as a function of specimen size and strain rate compared by the macro-scale 2 mm specimens.

Since this new invented Au-based BMG shows high Poisson's ratio (0.406), the mechanical properties were of interested and it was expected to have plasticity that most BMG materials lack of. With the anti-oxidation and anti-corrosion, the glass forming ability was investigated to see whether the Au-based BMG may be a material with high potential for micro-electro-mechanical systems (MEMS) applications.

Chapter 2 Background and literature review

2.1 The developments of bulk metallic glasses (BMGs)

The first metallic glass of $\text{Au}_{75}\text{Si}_{25}$ was produced by California Institute of Technology, Caltech, USA, in 1960 [2]. Duwez et al. discovered that if a molten metal is undercooled uniformly and rapidly enough, e.g. at 1×10^6 K/s, the heterogeneous atoms will not have enough time to rearrange into crystalline state. The liquid then reaches the glass transition temperature, T_g , and solidifies as a metallic glass. This brand new material has application potential for human beings to lead a better life compared with the old fashion way to fabricate which costs more money and fails to meet our expectancy [12–15]. This technique of rapid quenching has been widely used and innovated. In 1969, Chen and Turnbull fabricated amorphous spheres of ternary Pd-M-Si (with M = Ag, Cu, or Au) at critical cooling rates of 100 to 1000 K/s. The $\text{Pd}_{77.5}\text{Cu}_6\text{Si}_{16.5}$ glassy sphere has a diameter of 0.5 mm. With the endless efforts of researches from all over the world, in the early 1970s and 1980s, the continuous casting processes for commercial manufacture of metallic glasses ribbons, lines, and sheets [15] were developed. However, the size of this material is limited to the form of wires and sheets by the high cooling rate.

The first so called bulk metallic glass, compared the wires and thin sheets, was the ternary Pd–Cu–Si alloy prepared by Chen in 1974 [16]. They used simple suction-casting methods to fabricate millimeter-diameter rods of Pd–Cu–Si metallic glass at a lower cooling rate of 103 K/s [16]. In 1982, Turnbull and coworkers [17,18] successfully produced the famous Pd–Ni–P BMG by using boron oxide fluxing method. Nevertheless, the discovery of Pd-based BMG is an extraordinary milestone for metallic glasses research, due to the high

cost of Pd metal, the possibility of commercial usage seems to be impractical. Yet the passion for new BMG systems still persists. An overview of critical casting thickness and the date of discovery is shown in Figure 2.1 [19]. Progress has been significant and is outlined below. And in the 1980s, a number of vitrification techniques, such as mechanical alloying, diffusion induced vitrification in multi-layers, ion beam mixing, hydrogen absorption, and inverse melting, had been emerged.

Since the 1980s, Akihisa Inoue, of Institute for Materials Research, Tohoku University, and William L. Johnson of Caltech have discovered a variety of amorphous systems, such as La- [27], Mg- [20], Zr- [21,22], Pd- [25], Fe- [23,24], Cu- [25], and Ti- [26,27] based alloys with large undercooling and low critical cooling rates of 1-100 K/s. That enables a greater critical casting thickness (>10 mm) by conventional molding. In 1988, Inoue discovered that the La-Al-TM (TM = Ni, Cu) BMGs. By using Cu molds, they cast glassy $\text{La}_{55}\text{Al}_{25}\text{Ni}_{20}$ up to 5 mm thick in 1988, glassy $\text{La}_{55}\text{Al}_{25}\text{Ni}_{10}\text{Cu}_{10}$ up to 9 mm in 1991 [28]. The Mg-TM-Y system was also shown in 1991 to have high glass-forming ability in the form of $\text{Mg}_{65}\text{Cu}_{25}\text{Y}_{10}$ [29]. Another promising system is the Zr-Al-Ni-Cu based alloy, for example, $\text{Zr}_{65}\text{Al}_{7.5}\text{Ni}_{10}\text{Cu}_{17.5}$ with a critical casting thickness of 15 mm [30]. Johnson and Peker in Caltech developed $\text{Zr}_{41.2}\text{Ti}_{13.8}\text{Cu}_{12.5}\text{Ni}_{10.0}\text{Be}_{22.5}$ in 1991, as part of a US Department of Energy and NASA funded project to develop new aerospace materials. With critical casting thickness of up to 100 mm, the alloy was known as Vitreloy 1 (Vit1), the first commercial BMG. Figure 2.2 exhibits the as-cast Zr-based BMGs in different shapes prepared by the Institute of Physics, Chinese Academy of Sciences, China [31]. Groups at the Institut National Polytechnique de Grenoble, France, the Leibniz Institute for Solid State and Materials Research Dresden, European Synchrotron Radiation Facility, the Institute of Metallurgy and Materials Science in Krakow, Universidad Complutense Madrid, Universitat Autònoma de Barcelona, and the Universities of Cambridge, Sheffield, Ulm, and Turin collaborated on the

development of Zr-, Mg-, Fe-, Al-, Pd-, Hf-, and Nd-based alloys. Research aimed at increasing the concentrations of light elements such as Ti, Al, and Mg in environmentally safe, as well as Be-free Zr-based alloys. Table 2.1 lists the typical BMG systems and the year in which they were first reported. It is clear that the BMGs were developed in the sequence beginning with the expensive metallic based Pd, Pt and Au, followed by less expensive Zr-, Mg- Ti-, Ni- and Ln-based BMGs [31].

2.2 Thermal stability and glass forming ability of BMGs

Metallic glasses could be fabricated by rapid quenching from the melt liquid when the quenching rate exceeds its critical cooling rate. Glass forming ability (GFA), which is related to the ease of devitrification, is vital for understanding the origins of glass formation. The GFA of an alloy is evaluated in terms of the critical cooling rate (R_c) for forming metallic glasses, which is the minimum cooling rate necessary to keep the melt amorphous without forming any crystal during the solidification process. The smaller R_c , the higher the GFA. However, the value of R_c is difficult to evaluate precisely. So many criteria have been proposed to elucidate the relative GFA of bulk metallic glasses by characteristic temperatures measured by differential thermal calorimetry (DSC).

For GFA concern, Figure 2.3 illustrates the relationship between the critical cooling rate (R_c), maximum sample thickness (t_{max}) and reduced glass transition temperature (T_g/T_m), where T_g glass transition temperature and T_m v.s. solidus temperature for amorphous alloys reported to date [33-36]. And the lowest R_c is as low as 0.10 K/s [37] for the $Pd_{40}Cu_{30}Ni_{10}P_{20}$ alloy and the t_{max} reaches values as high as about 100 mm. It is also noticed that the recent improvement of GFA reaches 6-7 orders lower for the critical cooling rate and 3-4 orders higher for the maximum thickness. What is more, there is a clear trend for GFA to increase

with increasing T_g/T_m . Figure 2.4 elucidates the relationship between R_c , t_{max} and the temperature interval of a supercooled liquid, ΔT_x , defined by the difference between T_g and crystallization temperature (T_x), $(T_x - T_g)$ [33-36]. One can see a clear tendency for GFA to increase with increasing ΔT_x . The value of ΔT_x exceeds 100 K for several amorphous alloys in Zr-Al-Ni-Cu and Pd-Cu-Ni-P systems and the largest ΔT_x reaches 127 K for the Zr-Al-Ni-Cu base system.

The most extensively used criterion is the reduced glass transition temperature, T_{rg} [38] ($= T_g/T_l$, where T_l is the liquidus temperature) and the supercooled liquid region, ΔT_x . T_{rg} shows a better correlation with GFA than that given by T_g/T_m for bulk metallic glasses. Usually the ΔT_x and T_{rg} are used as indicators of the GFA for metallic glasses. The tendency for R_c to decrease with increasing T_{rg} is shown in Figure 2.5 [33]. From the view point of T_{rg} ($= T_g/T_l$), liquidus temperature T_l can be used to indicate the relative stability of stable glass forming liquids; the lower T_l the larger stability of the liquid, so the liquid can remain stable to a lower temperature with no formation of any solid phase. Table 2.2 shows the composition of representative BMG systems, their glass transition temperature, T_g , onset temperature of crystallization, T_x , and onset melting point, T_m , and glass forming ability represented by reduced glass transition temperature, T_{rg} . For another parameter ΔT_x ($= T_x - T_g$), a larger ΔT_x value may indicate that the undercooled liquid can remain stable in a wider temperature region without crystallization [31]. The onset crystallization temperature T_x could be used to roughly compare the crystallization resistance during glass formation for metallic liquids, although in some compositions the decisive competing solid phase during cooling might be different from that on devitrification [39]. The larger T_x value suggests a higher crystallization resistance, so the larger GFA. Lu and Liu [40] proposed that the new parameter γ ($= T_x / (T_g + T_l)$) was defined for inferring the relative GFA among bulk metallic glasses. Regardless of alloy system, the relationship between γ and the critical cooling rate R_c

(K/s) as well as critical section thickness Z_c (mm) has been formulated as follows:

$$R_c = 5.1 \times 10^{21} \exp(-117.19\gamma), \quad (1)$$

$$Z_c = 2.8 \times 10^{-7} \exp(41\gamma). \quad (2)$$

Note that these two equations can be utilized to estimate R_c and Z_c when γ is measured from DSC. The parameter γ reveals that a stronger correlation with GFA than T_{rg} , and has been successfully applied to glass formation in the bulk metallic glass systems. In 2007, Du et al. [41] proposed a new parameter for GFA, $\gamma_m = (2T_x - T_g)/T_l$, which comprised the idea that overall liquid phase stability is positively related to the quantity of $(T_x - T_g)/T_l$ while the crystallization resistance is proportional to T_x .

In order to compare the efficiency of the currently proposed GFA criteria γ_m with previous parameters such as $\gamma (= T_g / (T_x + T_l))$, T_x / T_l , ΔT_x , T_{rg} , and $T_x / (T_l - T_g)$, they are all plotted against R_c , the critical cooling rate for glass formation. Figure 2.6 shows the correlation between the critical cooling rate and the parameter γ_m for metallic glasses.

Data were taken from the previous reseachers. A linear regression analysis shows that the relation between R_c with γ_m can be expressed as:

$$\log R_c = 14.99 - 19.441\gamma_m. \quad (3)$$

The fitting parameter R^2 value gives the idea of the effectiveness and consistency of different GFA parameters. The higher the R^2 value, the better is the correlation between the proposed GFA parameter and R_c . Compared with other parameters invented before, γ_m exhibits the best correlation with the glass forming ability.

Over the past decade, various empirical BMG formation criteria have been developed. The first one is the multi-component alloy systems consisting of more than three elements. And the second criterion is to pick elements with large differences in size, which leads to a complex structure for crystallization unfavorable. The third one is the negative heat of mixing among the major elements. From the thermodynamic point of view, by the generally known relation of $\Delta G = \Delta H_{\text{mix}} - T\Delta S_{\text{mix}}$, the low ΔG value can be obtained if the value of ΔH_{mix} is small and ΔS_{mix} is large. The large ΔS_{mix} is expected to be obtained in multi-component alloys systems because ΔS_{mix} is proportional to the number of component. The necessity of large negative heat of mixing is a result of the fact such distinct atoms tend to bond together. Therefore, if there are three different elements mixed together and the difference in atomic size is large, the atomic configuration tends to appear as high dense random packing. The last effective step is to find out alloy compositions with deep eutectics, which form liquids that are stable to relatively low temperatures [42].

2.3 Mechanical behavior of amorphous metallic alloys

2.3.1 Deformation mechanisms

Due to the fact that the bonding in amorphous alloys is of metallic character, strain can be readily accommodated at the atomic scale through changes in neighborhood; atomic bonds can be broken and deformed at the atomic scale without substantial concern. On the other hand, unlike crystalline metals and alloys, metallic glasses only exhibit short-range order. Crystal dislocations provide the deformation mechanism at low energies in crystals, the local rearrangement of atoms in metallic glasses is a relatively high-energy or high-stress process. The mechanism of rearrangement is depicted in the two-dimensional schematic of illustrations Figure 2.7, originally proposed by Argon and Kuo [43] in 1979 on the basis of an

atomic-analog bubble-raft model. The diagram depicted in Figure 2.7 has been referred to as a “flow defect” or “s defect” [44,45], a “local inelastic transition” [46–48] and, increasingly commonly, a “shear transformation zone” (STZ) [45,47]. The STZ is essentially a cluster of atoms that undergo an inelastic shear deformation from one relatively low energy configuration to a second such configuration, crossing an activated configuration of higher energy and volume. After the original analog model of Argon and his colleague [41,48], more sophisticated computer models have been employed to study glass deformation in both two and three dimensions [44,45,49,50].

STZs are common for deformation in all amorphous metals, although details of the structure, size and energy scales of STZs may change from one case to another. It needs to be noted that an STZ is not a defect in an amorphous metal, however, lattice dislocation is a crystal defect. An STZ is defined at an instant—it is observed only when a change from one moment in time to the next. In other words, an STZ is an event defined in a local volume, not a feature of the glass structure. For instance, the local distribution of free volume is believed to control deformation of metallic glasses [43,50,51,52], and it is easy to envision that sites of higher free-volume would more readily accommodate local shear. The first quantitative model of STZ behavior was developed by Argon [53]. The STZ operation takes place within the elastic confinement of a surrounding glass matrix, and the shear distortion leads to stress and strain redistribution around the STZ region. Argon calculated the free energy, ΔF , for STZ activation in 1979 in terms of the elastic constants of the glass as below [53]:

$$\Delta F = \left[\frac{7-5\nu}{30(1-\nu)} + \frac{2(1+\nu)}{9(1-\nu)} \beta^2 + \frac{1}{2\gamma_o} \cdot \frac{\tau_o}{\mu(T)} \right] \cdot \mu(T) \cdot \gamma_o^2 \cdot \Omega_o, \quad (4)$$

where ν is the Poisson's ratio, τ_0 is the athermal shear stress at which the STZ transforms, and $\mu(T)$ is the temperature dependent shear modulus. The second term in the brackets captures the dilatational energy associated with STZ operation, and β is the ratio of the dilatation to the shear strain. Based on analog models of glass plasticity [43,50], the characteristic strain of an STZ, γ_0 , is usually taken to be of order 0.1, although this quantity can certainly be expected to vary across glass compositions and structural states. The characteristic volume of the STZ, Ω_0 , is generally believed to encompass about 100 atoms, as supported by simulations and many indirect experimental measurements.

An alternative aspect on the mechanism of plastic flow in amorphous alloys is given by the classical free-volume model, proposed by Turnbull and co-workers [54,55] and applied to the case of glass deformation by Spaepen [52]. This model essentially takes deformation as a series of discrete atomic jumps in the glass, as shown schematically in Figure 2.7; these jumps are obviously favored near sites of high free volume which can readily accommodate them. Because of the diffusion-like character of the process, the characteristic energy scale is of the order of the activation energy for diffusion [52,55,56], which is quite similar to the lower end of the range for the expected energy for an STZ operation. However, whereas the STZ activation energy corresponds to a subtle redistribution of many atoms over a diffuse volume, the activation energy in the free volume model corresponds to a more highly localized atomic jump into a vacancy in the glass structure.

The free volume model introduces a simple state variable to the problem of glass deformation, and allows constitutive laws to be developed on the basis of free volume creation and annihilation through a simple mechanism. Although the differences in the STZ-type model and the diffusive-jump-type model, these atomic-scale mechanisms share

many common features that are crucial to understanding the macroscopic deformation response of metallic glasses: Both mechanisms show characteristics of a two-state system; forward jumps or STZ operations compete with backward ones, and these can occur at the same spatial position in sequence. This behavior has implications for the rheology of flowing glass, as well as anelastic and cyclic deformation. Both of them are thermally activated, and exhibit similar energy scales; strength and flow character are significantly dependent upon temperature, and can be predicted on the basis of transition-state theory activated processes. And they are dilatational. Such dilatation is vital for flow localization and pressure dependency of mechanical properties.

Some researchers have attempted to explain plasticity in amorphous alloys in terms of dislocation models, for example, the attempt by Gilman in 1975 [57], although linear structural defects are not easily defined in an amorphous structure. The general definition of a dislocation is the boundary between a region of material which sheared and a region which has not. Under conditions where glass deformation proceeds through shear localization, an ongoing shear band may spread by propagation of a shear front, which therefore represents a kind of dislocation. Professor Li indicated in 1978 that the stress concentration associated with such a shear front (which he viewed as a Somigliana dislocation) can contribute to shear localization [58]; that is equal to state that the stress concentration activates STZs ahead of the shear front, causing it to advance. Interactions between the so called Somigliana dislocation and microstructure do not determine the mechanical properties of amorphous alloys as crystalline solids. For example, metallic glasses do not show strain harden, even with high shear band densities. The atomic scale mechanisms described above, STZ- and free-volume-type models, form the foundation for more quantitative understanding of metallic glass deformation.

2.3.2 Shear bands

At high stresses and lower temperatures, metallic glasses deform through localization processes. Under most loading, localization usually takes place through the formation of shear bands, which forms very rapidly and can accommodate displacements apparently up to nearly the millimeter scale [59]. The definition of “shear band”, a term which is variously used to describe an event, the residual trace of that event seen as a surface offset, a transient structural feature of a deforming body, or a permanently altered region within a metallic glass. Two experimental of SEM micrographs illustrating shear “slip steps” associated with shear band operations in metallic glasses are shown in Figures 2.8 (a) and 2.8 (b).

Homogeneous flow is well described by using rheological models, but inhomogeneous flow of metallic glasses is not. However, the inhomogeneous formation of shear bands has important practical results for the strength, ductility, and toughness. Shear localization or shear band formation is generally recognized as a direct consequence of strain softening—an increment of strain applied to a local volume element softens that element, enabling continued local deformation. For amorphous alloys, there are many causes for strain softening and localization, including the local formation of free volume due to flow dilatation, local evolution of structural order due to STZ operations, redistribution of internal stresses associated with STZ operation, and local heat generation. Despite all of these have been discussed by researchers, the dominant theory is generally believed to be a local change in the state of the glass.

Argon in 1979 [53] modeled localization as a result of strain softening from free volume accumulation. By the STZ model, he took the origin of a shear band as a local perturbation in strain rate, and examined the growth of this perturbation with applied strain in a

one-dimensional model. He introduced the dynamics of free volume accumulation with strain, and its softening effect. Furthermore, he derived and solved a bifurcation equation describing the divergence of strain rate in the band and in the surrounding matrix. Figure 2.9 (a) elucidates the acceleration of strain development in the shear band as the shear strain γ increases, and meanwhile the decrease of shear strain rate in the surrounding matrix. On the other hand, the free volume model was proposed by Steif et al. [60]. In this case, the perturbation was taken as a fluctuation of free volume, and tracked by numerically solving equations for free volume and strain rate evolution. The works of Steif et al. are illustrated in Figure 2.9 (b), and complement those of Argon from Figure 2.9 (a).

Both of the models imply the same basic notion for events upon loading a metallic glass in the inhomogeneous regime. When stress is increased, strains are first accommodated elastically, until the stress level increases to a threshold where it can activate flow in a locally perturbed region.

Plastic shearing within a shear band ceases when the driving force for shear decreases below some threshold value, i.e, when the applied strain is fully accommodated by the shear accumulated within the band, relaxing the stress. This phenomenon happens usually in constrained modes of loading, for example, indentation [61], or compression. In these cases, shear bands form exclusively to accommodate the imposed shape change, and strain only to the extent required for this purpose. The result shows a single shear band operates and arrests, the material can be deformed further through sequent shear banding operations. Load–displacement responses from such experiments exhibit characteristic patterns of flow serration, as shown in Figures 2.10 (a) and 2.10 (b) for constrained compression and indentation loading. Each serration is a relaxation event associated with the formation of a shear band, registered as a load drop when the experiment is displacement controlled (Figure

2.10 (a)), or a displacement burst under load-control (Figure 2.10 (b)). Under constrained loading, the net flow of metallic glasses is manifested through a series of shear banding events, and is typically characterized, as elastic–perfectly plastic [62,63]. The operation of secondary shear bands can be influenced by prior operation of a primary one [64,65]. Actually, secondary shear bands sometimes can operate directly stop primary ones [64,66]; it turns out to be more than one shear banding event on the same shear plane.

2.3.3 Size effects in plasticity

For metallic glasses, the intrinsic structural length scales of the system are generally believed to be of atomic dimensions, 10–100 atom volumes associated with the STZ activity. For most experiments, the scale of the test (or specimen) is much larger than this intrinsic scale; hence, complications due to size-related constraints on the deformation mechanism can be neglected. But, the process of shear localization introduces additional length scales to the deformation of metallic glasses, including the width of a shear band (cited as 10–1000 nm in the earlier discussion), its shear displacement, and the characteristic spacing between shear bands. Due to these different scales, size effects play an important role in mechanical experiments.

If one performs experiment with a smaller specimen size, then it is obvious that the characteristic shear band spacing on the specimen will decrease if the shear banding events are to individually accommodate the same amount of strain. As a result, shear band spacing and shear displacement of a single shear band are proportional to the characteristic specimen size, an effect proposed by Conner et al., Ravichandran, and Molinari [63-67], as illustrated in Figure 2.11. This effect has significant meaning for the fracture of metallic glasses because fracture is generally believed to take place along a shear band once a critical level of

displacement has been reached. For this phenomenon in a scale dependent fracture, the thinner specimens may be bent to larger plastic strains without fracture and thicker plates are apparently brittle [63-67]. The size effect described above is basically geometrical in nature, and has been discussed without consideration of kinetic effects. What is more, shear band spacing and shear offset are also affected by strain rate and temperature. Although the details of shear band formation are not yet fully resolved, the process of localization is characterized by intrinsic time and length scales larger than those of STZs and, indeed, large enough to measure deformation behavior at small scales. Both the geometric and intrinsic size effects may have practical implications for the toughness and ductility of structural bulk metallic glasses, and are certainly germane for applications involving thin films or micro-devices.

2.4 Comparison between metallic glasses and engineering materials

Due to the fact that metallic glasses lack of periodic arrangement, they show a distinctive localization of the plastic deformation into shear bands instead of dislocations [68], which results in special properties, for instance, as compared with crystalline steel and Ti alloys in Figure 2.12, glassy alloys have similar densities but high Young's modulus and elastic strain-to-failure limit. The glasses have high tensile yield strength, i.e. a high strength-to-weight ratio, making them a possible replacement for Al, but with a much greater resistance to permanent plastic deformation.

With enough data of metallic glasses, BMGs, Ashby and Greer [69] make quantitative comparisons of their properties with conventional engineering materials. Figure 2.12 shows the elastic limit σ_y and Young's modulus E for more than 1500 metals, alloys and metal-matrix composites. The ellipses enclose the range of values associated with given materials and material groups. The data on the conventional metallic materials are from a

standard database [70]; the metallic glasses are identified by their compositions (in at.%). The metallic glasses show at the upper edge of the plot. They have high strength (the highest known exceeds 5 GPa [71]), which shows a correlation with Young's modulus. The shading shows the theoretical strength ($\sigma_y = E/20$), which the metallic glasses approach more closely than any other bulk metallic crystalline material. The contours on Figure 2.13 imply the material indices σ_y/E and σ_y^2/E . And the first one is the yield strain; the second one is called the resilience, a measure of the ability of the material to store elastic energy. By the diagram, it shows that the metallic glasses is the best among them, having a larger yield strain and storing more elastic energy per unit volume than any of the other 1500 materials on the same plot.

Figure 2.14 shows the resilience, σ_y^2/E and loss coefficient, η , a parameter of the mechanical damping or energy loss in an elastic load cycle. High resilience is associated with low loss coefficient, implying the contribution of local plastic flow to energy loss. Once again the metallic glasses show excellent property. Their combination of high resilience and low energy loss is attractive for vibrating-reed systems such as springs. Figure 2.15 illustrates fracture toughness K_c (a parameter of load bearing capacity before fracture) and modulus E for some 2000 metals, ceramics, glasses and polymers. The metallic glasses (data from Ref. [72]) are identified by their compositions. For many applications, failure is energy-limited rather than load-limited; the appropriate material parameter is then not K_c , but rather the toughness $G_c (=K_c^2/E)$. The toughest metallic glasses lie above the metals. In the view of brittle materials, there is a basic limit: G_c cannot be less than 2γ , where γ is the surface energy.

Figure 2.16 shows the fracture toughness against elastic limit σ_y . The diagonal contours show the process-zone size, $d (=K_c^2/\sigma_y^2)$. Suppose the ultimate size, d , of the plastic zone at

the tip of a sharp crack is much smaller than the sample size, fracture will take place. On the other hand, if d is greater than the sample size, brittle failure is not expected. Although for some cases of metallic glasses that have very high fracture toughness K_{IC} , they still have small zone sizes ($d < 1$ mm) in that σ_y is so large. The high toughness of some metallic glasses appears to exhibit no ductility (in tension experiments), which results from shear localization. But, their plasticity in compression is measurable and can be impressive in some cases [73,74].

2.5 The birth of Au-based BMG ($\text{Au}_{49}\text{Ag}_{5.5}\text{Pd}_{2.3}\text{Cu}_{26.9}\text{Si}_{16.3}$)

The metallic glasses with high Poisson's ratio are expected to have good plasticity. By the aid of the periodic table, there are only three pure elements that have Poisson's ratios higher than 0.4 – 0.45 for Tl, 0.44 for Pb, and 0.44 for Au. Due to the shortcomings of toxicity and health problems found in Tl and Pb, Au-based BMG seemed to be the good choice for investigating the relationship between plasticity and Poisson's ratio and applications. A suitable Au-based BMG for most applications requires a T_g of at least 370 K for the sake of thermal stability, a large gold content (~18 karat or higher), high hardness, good processibility, and a critical casting thickness that permits fabrication of net-shaped articles such as jewelry. In a view of processing, it is desirable to have a large supercooled liquid region, which in turn enables thermoplastic processing.

The binary gold silicon composition was the first alloy found to exhibit metallic glass formation. However, the critical casting thickness, d_c , is below 50 microns. By partially substituting Si by Ge, increases in both the glass forming ability and the width of the supercooled liquid region were observed [75]. However, the result properties are not good enough to meet the needs as mentioned above. In 2005, Schroers et al. [9] invented a

Au-based BMG ($\text{Au}_{49}\text{Ag}_{5.5}\text{Pd}_{2.3}\text{Cu}_{26.9}\text{Si}_{16.3}$) by using the Au-Cu-Si ternary system extending to higher alloys by adding one or more alloying elements. Basically, Ag and Pd are used to replace Au. The atomic radius of the five elements in the alloys is listed in Table 2.3. It can be seen that Au, Ag, and Pd belong to the relatively larger atoms, Cu the medium one, and Si the smaller atom.

Schroers et al. [9] divided the composition into three groups. One is the partial substitution of Au, one group for Cu, and then still another group is for partial substitution of Si. In such an embodiment, Ag is a preferred additional alloying element. Researchers have found that adding Ag to the Au-based alloys of the current invention improve glass forming ability, the supercooled liquid region, and the glass transition temperature. Another additive alloying element is Pd. When Pd is added, it should be added at the expense of Au, where the Pd to Au ratio can be up to 0.3. A preferable range of Pd to Au ratio is in the range of from about 0.05 to about 0.2. Pt has a similar effect on processibility and properties of the Au-based alloy, and it should be added in a similar way as for Pd.

During the development of $\text{Au}_{49}\text{Ag}_{5.5}\text{Pd}_{2.3}\text{Cu}_{26.9}\text{Si}_{16.3}$ alloy, the Au content was varied between 40% and 60%, Ag content was varied from 0-20%, Pd from 0-5%, Cu from 0-35%, and Si from 14-20% (all atomic percent). Among the compositions of these alloys, the Si and Pd have the strongest influence on the glass forming ability and ΔT . This is illustrated in Figures 2.17 and 2.18, which illustrate the relationship of the critical casting thickness and ΔT on Si and Pd content. The Si content was varied between 14 and 20%, resulting in a variation of d_c from 1 to 5 mm, and a variation of ΔT from 35 to 60 K. By varying the Pd content from 0% to 5%, ΔT increases continuously with some scatter whereas d_c reaches a maximum at Pd = 2.3%. In both cases, a strong dependence of ΔT and d_c on the composition variations can be observed. And this composition, $\text{Au}_{49}\text{Ag}_{5.5}\text{Pd}_{2.3}\text{Cu}_{26.9}\text{Si}_{16.3}$, can be fabricated maximum casting thickness as high as 5 mm [9].

2.6 The parameters to distinguish plasticity or brittleness

By the inspiration of that the intrinsic plasticity or brittleness of crystalline metals correlates with the ratio of the elastic shear modulus μ to the bulk modulus B ; μ/B , Lewandowski et al. [76] proposed that the amorphous alloys would show the same relationship. For example, when the ratio μ/B exceeds a critical value, the material is brittle. The resistance to plastic deformation is proportional to the shear modulus, μ . In either case, the resistance to dilatation caused by the hydrostatic stress state present near the crack is proportional to the bulk modulus, B . And the relationship between ν and μ/B can be shown as below:

$$\nu = \frac{1 - 2\mu/3B}{2 + 2\mu/3B}, \quad (5)$$

From this equation, it can be seen that ν increases with decreasing μ/B , as shown in Figure 2.19. With the contributions of the researchers, Figure 2.20 shows a clear correlation between fracture energy G and μ/B . With low values of μ/B , the glasses based on palladium, zirconium, copper or platinum, all with fracture energies well in excess of 1 kJ m^{-2} , exhibit extensive shear banding, and have vein-patterns fracture surfaces. With high μ/B the magnesium-based glass approaches the ideal brittle behavior associated with oxide glasses. The report [77] of platinum-based glasses with low μ/B and exceptionally high toughness and fit well on the same correlation. This correlation between G and μ/B is similar to crystalline metals. For a metallic glass, the value of μ/B is typically about two-thirds of the value for the polycrystalline pure metal on which it is based. The glasses might therefore be expected to show more plasticity, but this is offset by the shift in value of $(\mu/B/B)_{\text{crit}}$ which divides plasticity and brittle fracture. For metallic glasses, the value is in the range 0.41–0.43, where

there is a large drop in G with increasing μ/B , and G approaches the toughness of oxide glasses. This is lower than the range of $(\mu/B)_{\text{crit}}$ values reported earlier for polycrystalline pure metals. Overall, it would appear that glassy alloys are slightly more likely than their crystalline counterparts to show brittle behaviour. The correlation between fracture energy and elastic constants can also be expressed in terms of Poisson's ratio. Higher values of ν give higher fracture energy, as shown in Figure 2.21. In a word, metallic glasses with $\mu/B > 0.41\text{--}0.43$ (or with $\nu < 0.31\text{--}0.32$) are brittle and vice versa.

2.7 Applications of bulk metallic glasses

With the unique and extraordinary characteristics, BMG materials are useful for application in various fields. One of the great advantages of BMGs is the ease of fabrication into complicated shapes. So far, BMGs have already been used as sporting equipment (Zr-Ti-Cu-Ni-Be and Zr-Ti-Ni-Cu BMGs) and electrode materials (Pd-Cu-Si-P BMG). The development of Fe-based BMGs has reached the final stage for application as soft magnetic materials for common mode choke coils. Success in this area will result in the increasing importance of BMGs. Table 2.4 summarizes the present and future application potentials for the BMGs [31]. The company that fabricates BMGs is Liquidmetal Technologies, co-founded in 1987 as Amorphous Technologies International with Caltech's Johnson as vice chairman and Peker as vice president, was the first company to produce amorphous metal alloys in viable bulk form. With an exclusive worldwide license for the Zr-based alloy Vitreloy (also known as 'Liquidmetal'), principal areas for products are sports and luxury merchandises, electronics, medical, and defense.

2.7.1 Golf club heads

The first application to be found was as golf club heads. According to the literature of the BMG golf plate manufacturer [19], steel club heads transfer about 60% of the input energy to the ball and titanium transfers 70%, whereas the metallic glass transfers 99%. With Higher strength-to-weight ratio allows mass to be distributed differently, enabling various shapes and sizes of head. High production costs, however, led to Liquidmetal Technologies to terminate manufacture in favor of licensing the technology to established club makers. Figure 39 shows the outer shapes of commercial golf clubs in wood-, iron- and putter-type forms where the face materials are composed of Zr-Al-Ni-Cu-Be bulk amorphous alloys.

2.7.2 Cases for consumer electronics

The possibility of moulding into components with thin sections allows BMG to challenge magnesium alloys in the electronic appliances market. With the trend of miniaturization of personal electronic devices such as MP3 players and personal digital assistants (PDA), there is a pressing need to make the casing thinner while retaining sufficient mechanical strength. BMGs exhibit obvious advantages over polymeric materials and conventional light alloys. Mobile phones and digital cameras with BMG casing are already developed [19].

For example, Vitreloy can also yield stronger, lighter, and more easily molded casings for personal electronic products. In September 2002, at a new \$45 million factory in Pyongtaek, South Korea, Liquidmetal began making components for liquid crystal display casings on cell phones. But, again, costs became a problem. Manufacturing process limitations, higher-than-expected production costs, unpredictable customer adoption cycles, short product shelf-life, and intense pricing pressures have made it difficult to compete profitably in this commodity-driven market. The company is now focusing on manufacturing

selected, higher-margin cell phones (mainly for Samsung), value-added sports and medical products, as well as research development and prototyping. Liquidmetal Technologies' is also working with design firm Ideo to create a Vitreloy-encased laptop that rolls up like a piece of paper [19].

2.7.3 Liquidmetal rebounds

Liquidmetal Technologies also produced leisure equipment that requires good rebound. It teamed with Rawlings Sporting Goods Company, Inc. to produce baseball and softball bats. Meanwhile it worked with HEAD on skis and snowboards. Other potential applications in sporting goods include fishing equipment, hunting bows, guns, scuba gear, marine applications, and bicycle frames. Vitreloy can also be used for watch cases to substitute Ni and other metals, which may cause allergic reactions, and. A few years ago, Liquidmetal Technologies teamed up with the watch and jewelry division of LVMH, whose luxury watchmaker TAG Heuer launched a special edition "Microtimer Concept Watch" last April featuring Vitreloy as the scratch- and dent-resistant, and high-gloss casing [19].

2.7.4 Medical applications

Another area is a biocompatible, non-allergic form of the glassy material that would be suitable for medical components such as prosthetic implants and surgical instruments. The unique properties of BMGs for orthopedic applications include: (1) biocompatible; (2) excellent wear resistance; (3) high strength-to-weight ratio compared to titanium and/or stainless steel; (4) more than twice the strength compared to titanium or stainless steel; (5) possibility of precision net-shape casting with desirable surface texture which results in significant reduction in post-processing.

For example, DePuy Orthopaedics, Inc. is using the material in knee-replacement devices. Other applications include pacemaker casings. In 2002, Surgical Specialties began producing ophthalmic scalpel blades using the Vitreloy alloy. They are higher quality but less expensive than diamond, sharper and longer lasting than steel, and more consistently manufacturable, since they are produced from a single mold [19].

2.7.5 Defense and aerospace

Metallic glasses can also play the role as military materials that are stronger, lighter, and more effective at high temperatures and stresses. These can replace depleted uranium penetrators in antitank armor-piercing projectiles because of their similar density and self-sharpening behavior.

NASA's Genesis spacecraft, the first mission to collect and return samples of the solar wind—fast moving particles from the Sun—will help scientists to refine the basic definition of the Sun's characteristics, and understand how the solar nebula, a large cloud of gas and dust, gave rise to our complex solar system. Genesis has received its final piece of science equipment: a solar wind collector made of a new formula of bulk metallic glass [19].

2.8 Viscous flow behavior

Amorphous alloys are metallic materials with a disordered atomic-scale structure. Compared with other metals, which are crystalline and hence have a highly ordered arrangement of atoms, amorphous alloys are non-crystalline. Bulk Metallic glasses (BMGs) show some special physical properties such as excellent elasticity and strength as compared

to crystalline alloys. What is more, significant plasticity occurs in the supercooled liquid region, $\Delta T_x (= T_x - T_g$, where T_x is the crystallization temperature and T_g the glass transition temperature), due to a tremendous drop in viscosity at temperatures above T_g upon heating [78]. Thus, it is feasible to produce structural parts with complicated shapes in this temperature region [79,80]. Generally, low viscosity and high thermal stability of a supercooled liquid are the two main properties of BMGs for superplastic microforming or imprinting of micro-electro-mechanical (MEMS) devices. The temperature dependence of viscosity in the Zr, Mg, La, and Pd based BMGs has been measured using various thermomechanical techniques to assess the glass fragility before [81-85].

The viscosity, η , is calculated by the Stefan equation [86] with the geometrical correction of viscous flow,

$$\eta = \left(\sigma / 3 \dot{\epsilon} \right) \cdot \left[1 + d_0^2 / 8 l_0^2 (1 + \epsilon_n)^2 \right]^{-1}, \quad (6)$$

where σ , $\dot{\epsilon}$, d_0 and ϵ_n are the true stress, strain rate, initial sample diameter and nominal strain, respectively. In the equation (11), the true compressive stress σ is calculated using $\sigma = (F/A_0)(l/l_0)$, where F , A_0 , l , and l_0 are the applied load, initial cross-sectional area, length after deformation, and initial length, respectively.

Chapter 3 Experimental procedures

3.1 Materials

The elements used in this study were purchased from Well Being Enterprise Co., Ltd, Taipei, Taiwan. Moreover, the purities of the elements are of concern; that gold is as pure as 99.99%, silver is as pure as 99.99%, copper is as pure as 99.99%, palladium is as pure as 99.99%, and silicon is as pure as 99.99%.

3.2 Sample preparation

3.2.1 Arc melting

In order to prepare the multi-component amorphous alloys, the arc melting method was used in this study. Pure elemental pieces are used in this route. The maximum operating temperature is 3500°C.

Before the starting of arc melting process, because crystallization will result from the oxygen impurity, the argon gas needs to be continuously purged into the furnace to flush the oxygen and maintain a positive argon pressure to ensure a low oxygen vapor pressure environment inside the furnace. Cold water also needs to be poured into and flowing through the bottom of the Cu mold to increase the heat exchange rate. Finally, the chosen component placed on the Cu mold will be melt by the high voltage arc under a Ti getter argon atmosphere. It should be repeated for more than four times to confirm the homogeneous mixing of composition. Besides, the cooling rate of arc process is not fast enough to form

amorphous alloys, so it needs to further conduct the injection casting or melt spinning process.

3.2.2 Suction casting

After the ingots are melted homogeneously by arc melting, the melt is immediately sucked into a water-cooled copper mold that has internal cylindrical-shaped cavities to fabricate the Au-Ag-Pd-Cu-Si glassy rod under an argon atmosphere. The different molds with a cylindrical shape inside could be replaced to prepare the cylindrical alloy rods with various diameters. The suction casting was prepared by Prof. J.S.C Jang's Lab in I-Shou University.

3.2.3 Micro-sample fabrication using Focused Ion Beam milling

The BMG was sliced to a disk of 1.5 mm height by a diamond cutter, and then ground with the abrasive paper from #1200 to #4000. The surfaces of focus ion beam (FIB) machining specimens was polished to a mirror finish with a diamond polishing paste, from 1 μm grit to 0.25 μm for FIB machining. Compression samples were prepared using the dual focus ion beam system of Seiko, SMI3050 SE, following the method developed previously [87]. First of all, Ga beam of 30 keV and 7-12 nA currents in FIB was used to mill a crater with a bigger size island located in the center. Then the same voltage and smaller currents of 3 down to 0.2 nA were used to refine the preserved central island to a desired diameter and height of pillars. A series of concentric-circle patterns were utilized to machine the pillars. Three different kinds of micropillars with diameters of 3.8 μm and 1 μm were fabricated, as shown in Figure 3.1. These pillars are tapered because the divergence of ion beam, and the convergence angle is about 2.5° from the longitudinal direction. For the experiments of

micro-compression, those are the contributions by Dr. C.J. Lee.

3.3 Property measurements and analyses

3.3.1 X-ray diffraction

The amorphous nature of the Au-based BMG was examined by X-ray diffraction (XRD) and transmission electron microscopy (TEM). The SIEMENS D5000 X-ray Diffractometer with Cu K α radiation ($\lambda = 1.5406 \text{ \AA}$) at 40 kV and 30 mA is utilized. The range of the diffraction angle 2θ is within 20° to 80° scanning rate of 0.1° per four seconds.

3.3.2 Qualitative and Quantitative constituent analysis

To identify the constituent components and confirm the composition percentage of the bulk metallic glasses, the specimens are characterized with a scanning electron microscope (SEM) with energy dispersive X-ray spectrometer (EDS). The cross-sectional surface of alloys sliced from bulk metallic glass rods is selected to examine the quantity of the designed compositions by EDS.

3.3.3 DSC thermal analysis

Glass forming ability parameters associated with the glass transition temperature (T_g), the crystallization temperature (T_x), the supercooled liquid region (ΔT_x), the solidus temperature (T_m) and the liquidus temperature (T_l) are determined by differential scanning calorimeter (DSC). In this study, the thermal behavior of Au₄₉Ag_{5.5}Pd_{2.3}Cu_{26.9}Si_{16.3} bulk metallic glasses is analyzed using a SETARAM DSC131 differential scanning calorimeter under an argon

atmosphere, at the constant heating rate of 40 K/min and the heating range from 300 to 700 K. The pre-presence air in the DSC chamber is flushed by pure Ar and it is keep the positive Ar pressure while heating.

3.3.4 Density measurement

The well-know principle of Archimedes is used as an appropriate means to measure the density of amorphous alloys. In this technique, the specimen contained in a vessel is weighted in air and gets a value of mass W_1 . Then, the specimen is weighted in a liquid of known density β and gets a value of mass W_2 . Therefore, the density of amorphous alloy can be evaluated by the following equation :

$$\rho = \frac{W_1}{W_1 - W_2 / \beta} \quad (7)$$

The atomic configurations of amorphous alloys are different from those for the crystalline alloys.

3.3.5 TMA analysis

The relationship among temperature, relative displacement, effective viscosity, and effective linear expansion coefficient were measured using a thermomechanical analyzer (TMA, Perkin Elmer Diamond) under the isochronal (or non-isothermal) condition at a heating rate of 10 K/min and a fixed compression load of 50 mN. The load was applied by a tip with a diameter of 3.8 mm. Temperature was calibrated by using pure In and Zn samples as standards. The diameter of the specimen is 3 mm with aspect ratio around 2. Displacement

data under various pressures and temperatures were collected simultaneously upon heating.

3.3.6 Micro-hardness testing

The sample hardness testing was conducted using a SHIMADZU HMV-2000 Vicker's micro-hardness tester. In this testing, the parameter was carried out using a load of 200-500 g with 10 second duration, and the hardness value of each sample was average from 10 datum points.

3.3.7 Macro-compression testing

The compressive strength, elastic modulus and compressive strain were evaluated by using an Instron 5582 universal testing machine and the cylindrical specimens fabricated by the Cu mold casting method with a diameter of about 2 mm and a height of 4 mm. The compression specimens were sliced from $\text{Au}_{49}\text{Ag}_{5.5}\text{Pd}_{2.3}\text{Cu}_{26.9}\text{Si}_{16.3}$ BMG rods.

All the surfaces are ground by silicon carbide abrasive papers from #1200 to # 2000 with water and polished. Before the compression specimen was fixed into the crossheads of the Instron machine, BN plate used as lubricant to decrease friction between the test samples and compression platens. The fracture surface morphologies were examined by SEM. Ambient temperature compression tests were conducted on the specimens at different strain rates of 5×10^{-5} , 1×10^{-4} , 5×10^{-4} , and $1 \times 10^{-3} \text{ s}^{-1}$.

3.3.8 Micro-compression testing

At room temperature, micro-compression tests were performed with an MTS

nanoindenter XP under the Continuous Stiffness Measurement (CSM) mode using a flat punch, which was machined out of a standard Berkovich indenter also by FIB. The projected area of the tip of the punch is an equilateral triangle of 13.5 μm , as shown in Figure 3.2. In order to check the alignment and calibrate the distance, the pre-compressed experiment to 1.5 μm depth was conducted in locations away from the pillar sample; the distance between the indented position and the pillar was within one hundred microns, as shown in Figure 3.3. A perfect equilateral triangle impression is considered the system is well aligned. Prescribed displacement rates of 0.25-500 nm/s, corresponding to the initial strain rates of 6×10^{-5} – $6 \times 10^{-2} \text{ s}^{-1}$, were used to deform the pillars. This work was performed by Dr. C.J. Lee.

3.3.9 Microstructure examination

The fracture surface morphologies of BMG specimens after macro-compression, and micro-compression testing, and hot embossing were examined by JEOL JSM-6400 scanning electron microscopy (SEM). The different fracture features after compression testing would also be examined in order to study the deformation mechanisms for BMGs.

3.3.10 Hot embossing of micro-lens and V-groove

To know the formability of the Au-based BMG, hot embossing of micro-lens array and V-groove were performed. Originally, the viscous forming was intended to be conducted by hot pressing at low loads. Transforming into the compressive stress, the forming stress should be in the 100 to 1000 kPa range. However, the oil hydraulic plate system provides large embossing load from 20 kg to 400 kg for the hot embossing process. The Au-based BMGs were tested under the applied load of 27 MPa, 62 MPa, and 156 MPa, respectively, for micro-lens array for a duration of 10 minutes. For the case of V-groove, the Au-based BMGs

were tested under the loads of 62 MPa, 137 MPa, and 156 MPa for durations of 1, 5, and 10 minutes. Figure 3.4 shows the hot embossing set-up of the oil hydraulic system. Figure 3.5 illustrates the Ni–Co mold with gapless hexagonal micro-lens array [88]. Figure 3.6 shows the profile of V-groove mold.

3.3.11 Surface morphologies

In order to see the surface morphologies of the Au-based BMG after hot embossing testing, the α step system and atomic force microscope (AFM) were utilized. Since the height difference of V-groove mold is over limitation of AFM, in the case, the samples could only be observed by the α step. For micro-lens array, both AFM and α step were in use.

Chapter 4 Results

4.1 Sample preparations

The rods of the Au-based BMGs with different diameters 2 and 3 mm were fabricated by copper mold casting under an argon atmosphere in ISU University, as shown in Figures 4.1. The surface appearances of injection cast Au-based BMGs rods with different diameter 2 and 3 mm all show lustrous and shinning surface. This indicates that complete filling of the cavities was obtained during injection casting.

4.2 XRD analyses

The amorphous structure of the $\text{Au}_{49}\text{Ag}_{5.5}\text{Pd}_{2.3}\text{Cu}_{26.9}\text{Si}_{16.3}$ rods fabricated by copper mold cast method was identified by XRD. Figure 4.2 shows the XRD patterns of the $\text{Au}_{49}\text{Ag}_{5.5}\text{Pd}_{2.3}\text{Cu}_{26.9}\text{Si}_{16.3}$ alloy rods with diameters 2 and 3 mm, consisting of a broad diffraction peak over the 2θ range from 30° to 50° , which shows the amorphous structure property.

4.3 SEM/EDS observations

The composition analyses of the $\text{Au}_{49}\text{Ag}_{5.5}\text{Pd}_{2.3}\text{Cu}_{26.9}\text{Si}_{16.3}$ rods with 2 and 3 mm diameters were identified by SEM/EDS. By the EDS results, all the composition of the $\text{Au}_{49}\text{Ag}_{5.5}\text{Pd}_{2.3}\text{Cu}_{26.9}\text{Si}_{16.3}$ rods is close to the designed composition, as shown in Table 4.1.

4.4 TEM observations

Figure 4.3 shows the selected area diffraction (SAD) pattern of the $\text{Au}_{49}\text{Ag}_{5.5}\text{Pd}_{2.3}\text{Cu}_{26.9}\text{Si}_{16.3}$ alloy with 300 keV and 150 cm camera length. For the fully amorphous material, there should be concentric diffuse rings or halos without any discrete spots which stand for the crystalline phase. From the observation of Figure 4.3, that shows the material is not fully amorphous.

4.5 DSC analyses

The thermal properties of the $\text{Au}_{49}\text{Ag}_{5.5}\text{Pd}_{2.3}\text{Cu}_{26.9}\text{Si}_{16.3}$ BMGs were examined by DSC with the heating rate of 0.67 K/s (40 K/min), as shown in Figure 4.4. The crystallization exothermic reactions for the $\text{Au}_{49}\text{Ag}_{5.5}\text{Pd}_{2.3}\text{Cu}_{26.9}\text{Si}_{16.3}$ BMGs in the DSC curves appear as one single peak, indicating one major phase was induced during DSC heating. The Au-Cu binary diagram is shown in Figure 4.5. The glass transition temperature (T_g), the onset crystallization temperature (T_x), the solidus temperature (T_m) and the liquidus temperature (T_l) are all marked by arrows in the DSC traces. From the plot, it exhibits distinct T_g and T_x , followed by a wide supercooled liquid region and then the exothermic reactions due to crystallization followed by the endothermic reactions due to melt. The T_g , T_x , T_m and T_l of the $\text{Au}_{49}\text{Ag}_{5.5}\text{Pd}_{2.3}\text{Cu}_{26.9}\text{Si}_{16.3}$ BMGs at a heating rate of 0.67 K/s are 400, 450, 625 and 646K, respectively. The values of ΔT_x and ΔT_m are 50 and 21 K. The T_{rg} , γ , and γ_m values are parameters to estimate the glass forming ability. From the DSC plot, we can get the T_{rg} , γ , and γ_m values for the $\text{Au}_{49}\text{Ag}_{5.5}\text{Pd}_{2.3}\text{Cu}_{26.9}\text{Si}_{16.3}$ BMGs at the heating rate of 0.67 K/s are 0.619, 0.430 and 0.774, respectively. Figure 4.6 shows the thermal properties with the heating rate of 0.167 K/s (10 K/min). The T_g and T_x are 403 and 442 K, respectively.

4.6 Density measurement

The simplest method to detect whether the volume is changed is to measure the density. The Au-based BMG has the density value of 13.5 g/cm^3 . The value is smaller than the pure gold (19 g/cm^3), since the Au-based contains many other light elements and free volumes.

4.7 Micro-hardness testing

The hardness of the injection cast $\text{Au}_{49}\text{Ag}_{5.5}\text{Pd}_{2.3}\text{Cu}_{26.9}\text{Si}_{16.3}$ BMGs are measured by using the HMV-2000 micro-hardness tester. Ten positions are randomly chosen for each samples, then the Vickers hardness (H_v) are obtained by indenting each sample at the load of 200 g and with the duration time of 10 second. The value of micro-hardness is about 348 ± 10 which is much higher than ordinary gold alloys.

4.8 Macro-compression testing

The compressive mechanical properties at room temperature of the injection cast $\text{Au}_{49}\text{Ag}_{5.5}\text{Pd}_{2.3}\text{Cu}_{26.9}\text{Si}_{16.3}$ BMGs were measured by using an Instron 5582 type machine. Compression tests are conducted on specimens with various strain rates 5×10^{-5} , 1×10^{-4} , 5×10^{-4} , and $1 \times 10^{-3} \text{ s}^{-1}$ with an h/d ratio of ~ 2 .

The engineering compressive stress-strain curves for the injection cast $\text{Au}_{49}\text{Ag}_{5.5}\text{Pd}_{2.3}\text{Cu}_{26.9}\text{Si}_{16.3}$ BMGs are shown in Figure 4.7. Table 4.2 shows the summary of the macro-compressive of the Au-based BMGs at different strain rates. The compressive fracture strength and fracture elongation at the strain rate of $5 \times 10^{-5} \text{ s}^{-1}$ are $\sim 1003 \text{ MPa}$ and $\sim 1.85 \%$. At the strain rate of $1 \times 10^{-4} \text{ s}^{-1}$, the values are $\sim 1122 \text{ MPa}$ and $\sim 1.97 \%$, respectively. For the strain rate of $5 \times 10^{-4} \text{ s}^{-1}$, they are $\sim 933 \text{ MPa}$ and $\sim 1.59 \%$. And the compressive

fracture strength and fracture elongation at the higher strain rate of $1 \times 10^{-3} \text{ s}^{-1}$ are $\sim 827 \text{ MPa}$ and $\sim 2.00 \%$. The highest value of compressive fracture strength is the one at a strain rate of $1 \times 10^{-4} \text{ s}^{-1}$, and the highest fracture strain is the one at a strain rate of $1 \times 10^{-5} \text{ s}^{-1}$.

4.9 Compressive fracture characteristics

The outer appearance and fracture surface morphologies of the Au-based BMG are examined after compression testing by using SEM, as shown in Figures 4.8-4.21. The angle of the fracture plane inclination for the specimen at a strain rate of $5 \times 10^{-5} \text{ s}^{-1}$ is 38.4° , as shown in Figure 4.8. And Figure 4.9 illustrates the fracture surface morphology for the specimen after compression testing; the fracture surface reveals the features of the vein-like patterns. In an enlarged micrograph as shown in Figure 4.9, there shows the so called river-like morphology which appears in the form of islands surrounded by vein-like patterns and intermittent smooth regions that sometimes contain fine striations. The characteristic of vein-like patterns is due to a local change of viscosity in the fracture along shear band in metallic glasses. That shows the evidence for shear band propagation during compression testing.

Figure 4.11 illustrates that the angle of the fracture plane inclination is 38.8° for the specimen at a strain rate of $1 \times 10^{-4} \text{ s}^{-1}$. Figure 4.12 and Figure 4.13 illustrates the fracture surface morphology for the specimen after compression testing; the fracture surface reveals the vein-like patterns.

Figure 4.14 illustrates that the angle of the fracture plane inclination is 41.0° for the sample loaded at a strain rate of $5 \times 10^{-4} \text{ s}^{-1}$. Figure 4.15 shows the fracture surface morphology for the specimen after compression testing. The fracture surface reveals the

typical vein-like patterns. Furthermore, in an enlarged magnification, Figure 4.16 shows that the fracture surface for specimen consisting some spots around the vein-like patterns, those spots are another evidence to support the fact that this Au-based BMG is not fully amorphous.

Figure 4.17 shows that the angle of the fracture plane inclination is 39.2° for the specimen at a strain rate of $1 \times 10^{-3} \text{ s}^{-1}$. Figure 4.18 illustrates an enlarged micrograph of the outer appearance fracture plane of the Au-based BMG with a strain rate $1 \times 10^{-3} \text{ s}^{-1}$. Figure 4.19 is the micrograph of the side view. Figure 4.20 and Figure 4.21 show the fracture surface of Au-based BMG with strain rate $1 \times 10^{-3} \text{ s}^{-1}$. As shown in the pictures, the vein-like characteristics are denser than the others, indicating that the propagation of shear band is more intense and complicated. And that meets the results of Figure 4.7, the specimen with higher engineering strain, the more ductile one, is the one with more intense vein-like patterns.

4.10 Micro-compression testing

The micro-compression experiments were performed with an MTS nanoindenter XP under the Continuous Stiffness Measurement (CSM) mode using a flat punch. The load-displacement data are presented in Figures 4.22 and 4.23. Traditionally, the curves are converted to the engineering stress and strain curves, with the assumption that the sample is uniformly deformed. But the assumption is violated since a bulk metallic glass is deformed by the highly localized shear bands. Therefore, we present both the load-displacement data and the “apparent” stress-strain data.

The yield strengths of the 3.8 and 1 μm pillars range from 1629 to 1580 MPa, which are

much higher than that for the bulk $\text{Au}_{49}\text{Ag}_{5.5}\text{Pd}_{2.3}\text{Cu}_{26.9}\text{Si}_{16.3}$ samples (900-1100 MPa). These data are summarized in Table 4.3. From Table 4.3 it is obvious that average strength of the 1 μm pillar (1849 MPa) is higher than that of the 3.8 μm pillar (1693 MPa). The improved strength is a natural consequence of decreasing defect population and, thus, reducing probability of shear band initiation in smaller samples.

Figures 4.24 and 4.25 indicate the displacement occurred almost at a sudden, which means that the strain does not happen in a gradual way but in the form of burst, even the experiments were performed under strain rate control conditions. Every strain burst event, independent of the strain rate, proceeds within approximately one second. The strain burst illustrates a rapid propagation of localized shear band.

Figure 4.26 shows the morphology of compressed pillar samples. Shear band is anticipated to initiate from the corner of contact between specimen and compression punch due to the sample experiences the maximum stress, not only because it has the minimum cross section as a result of sample taper, but also due to the large constraint caused by the friction between the test specimen and punch. A finer shear band spacing was seen to form at a faster strain rate, as evident from Figure 4.22. The 1 μm pillars has less shear bands than the larger one. This implies that as the size decreases, it needs more energy to form shear bands, further enhancing the yield strength. It seems the shear band number would increase with increasing specimen size and strain rate.

4.11 TMA Analysis

Figure 4.27 illustrates the typical TMA and differential thermo-mechanical analyzer (DTMA) curves measured at a stress level of 7.1 kPa on Au-based BMG. The DTMA curve

is obtained from the derivative of the displacement with respect to time. The onset temperature for the viscous flow (T_{onset}), the semi-steady-state viscous flow temperature (T_{vs}), and the finish temperature for the viscous flow (T_{finish}), are marked on the TMA or DTMA curve. The values of T_{onset} , T_{vs} , and T_{finish} are 436 K, 456 K, and 473 K, respectively. The T_g and T_x measured from the DSC curves without loading are 400 and 450 K, respectively. Those differ from the T_{onset} and T_{finish} obtained from TMA under loading.

Figure 4.28 shows the viscosity data on the Au-based and Mg-based BMG. The viscosity of the Au-based BMG is ranged from 10^8 to 10^{11} Pa.s. At first, the curve decreases with increasing temperature and reach a minimum point when the temperature is near the supercooled liquid region. Above the temperature of T_{vs} , crystallization starts to occur and viscosity increases.

4.12 Hot embossing of V-groove on Au-based BMG

Since the semi-steady-state viscous flow temperature (T_{vs}) of the Au-based BMG is around 183°C (456 K), the temperature of the hot embossing experiment is set at 177°C (450 K). Figures 4.29, 4.30, and 4.31 show the replicated patterns, V-groove, on the Au-based BMG materials by optical microscopy (OM), formed at 177°C and 137 MPa for 1 minute, 5 minutes, and 10 minutes, respectively. By the observation of the OM pictures, with the same experimental temperature and pressure, the specimen with longer forming time, 10 minutes, has a longer interspacing between two bands, 153 μm , as shown in Figure 4.31. This could be explained that longer duration time enables the viscous flow of the BMG material to fill up the Ni–Co mold more completely. As a result, better surface quality and formability can be achieved. The value of band interspacing of the specimen at 177°C and 137 MPa for 1 minute is 143 μm . And the value of band distance of the specimen at 177°C and 137 MPa for 5

minutes is 148 μm . The data are all listed in Table 4.3.

Figure 4.32 illustrates the replicated patterns, V-groove, on the Au-based BMG materials by OM at 177°C and 62 MPa for 10 minutes. And Figure 4.33 shows the replicated patterns, V-groove, on the Au-based BMG materials by OM at 177°C and 156 MPa for 10 minutes. To know the exact difference of the specimens under different pressures, the α step system was utilized. Figure 4.34 shows clearly the heights of specimens under 62 MPa, 137 MPa, and 156 MPa, respectively. The average height of the specimen at 177°C and 62 MPa for 10 minutes is 11 μm . The average height of the specimen at 177°C and 137 MPa for 10 minutes is 45 μm . And the average height of the specimen at 177°C and 156 MPa for 10 minutes is 84 μm . All the data and mold information are all listed in Table 4.4 as well. Figure 4.35 shows The morphological curves of V-groove imprinted Au-based BMG at 177°C and 137 MPa for 1, 5, 10 min, respectively, by the α step.

4.13 Hot embossing of micro-lens array on Au-based BMG

For hot embossing of micro-lens array, Figure 4.36 shows replicated patterns on Au-based BMG materials imprinted at 177°C and 27 MPa for 10 minutes. Figure 4.37 shows replicated patterns on the Au-based BMG materials imprinted at 177°C and 62 MPa for 10 minutes. Figure 4.38 shows replicated patterns on Au-based BMG materials imprinted at 177°C and 156 MPa for 10 minutes. Figure 4.39 illustrates the morphological curves of mold and micro-lens array on Au-based BMG at 177°C and 27 MPa, 62 MPa, and 156 MPa, respectively, for 10 minutes by α step. The height and width of individual specimen under different pressure and mold information are all listed in Table 4.5. Figure 4.40 shows the replicated micro-lens array patterns on the Au-based BMG materials at 177°C and 156 MPa for 10 minutes by SEM

Before the embossing process, there are some marks on the surface of Au-based BMG , which is produced during its manufacturing process. To eliminate that, the surface was polished with abrasive papers from No. 1200 to No. 2000. However, parallel bands and marks on the surface can still be observed clearly in all the pictures no matter by OM or SEM.

Chapter 5 Discussions

5.1 Variation in compositions of Au-based BMG

As shown in the previous chapter, in the course of the development of the $\text{Au}_{49}\text{Ag}_{5.5}\text{Pd}_{2.3}\text{Cu}_{26.9}\text{Si}_{16.3}$ alloy, the Au content was varied between 40% and 60%, Ag content was varied from 0-20%, Pd from 0-5%, Cu from 0-35%, and Si from 14-20% (all in atomic percent). Among the compositions of these alloys, the Si and Pd have the strongest influence on the glass forming ability and ΔT . Regarding the differences in negative heat of mixing between the components, as shown in Table 5.1, the importance of Si and Pd can also be seen. The value of the heat of mixing is -30 kJ/mol for Au–Si, -20 kJ/mol for Ag–Si, and -55 kJ/mol for Pd–Si. Those values are quite high compared with those with other elements. With this composition, the $\text{Au}_{49}\text{Ag}_{5.5}\text{Pd}_{2.3}\text{Cu}_{26.9}\text{Si}_{16.3}$ alloy can be fabricated to a maximum casting diameter as high as 5 mm [7].

However, according to the current research, by the X-ray diffraction patterns and the TEM picture, the evidence shows that the Au-based BMGs fabricated are not fully amorphous even in the 2 mm diameter rod specimens, not to mention about the ones with larger diameters. And maybe a variation in compositions would solve this problem. By the observation of Table 5.1, the value of the heat of mixing is just -9 kJ/mol for Au–Cu. What is more, the atomic percent of Cu is 26.9, only less than Au. If the quantity of Cu in the Au-based BMG is lower, the fully amorphous Au-based may be expected. In the future, the trial for a composition with a lower Cu content might be feasible.

5.2 The glass forming ability of Au-based BMG

The properties of $\text{Au}_{49}\text{Ag}_{5.5}\text{Pd}_{2.3}\text{Cu}_{26.9}\text{Si}_{16.3}$ BMGs were investigated by DSC. By the previous researches, the Au-based BMG and Mg-based BMG have something in common, in terms of mechanical and thermal properties. Table 5.2 shows thermal properties of the $\text{Mg}_{65}\text{Cu}_{25}\text{Gd}_{10}$ and $\text{Au}_{49}\text{Ag}_{5.5}\text{Pd}_{2.3}\text{Cu}_{26.9}\text{Si}_{16.3}$ obtained from DSC at a heating rate of 10 K/min.

The interval of supercooled liquid region ΔT_x (50 K) for the Au-based BMG amorphous alloy is lower than the ΔT_x (60 K) for $\text{Mg}_{65}\text{Cu}_{25}\text{Gd}_{10}$, indicating that the Au-based BMG has a lower thermal stability than the $\text{Mg}_{65}\text{Cu}_{25}\text{Gd}_{10}$ amorphous alloy. The liquidus temperature (646 K) for Au-based BMG amorphous alloy is also lower than the liquidus temperature (726 K) for $\text{Mg}_{65}\text{Cu}_{25}\text{Gd}_{10}$. The lower liquidus temperature of the Au-based BMG indicates the higher stability of liquid phase for this alloy. This should be more promising to fabricate bulk metallic glasses.

In Table 5.2, the T_{rg} for the Au-based BMG is 0.619, which is higher than that for the $\text{Mg}_{65}\text{Cu}_{25}\text{Gd}_{10}$ amorphous alloy (0.565). The higher T_{rg} value is also considered to be the origin for the larger GFA. Meanwhile, the γ value for the Au-based BMG is 0.430, which is higher than that for $\text{Mg}_{65}\text{Cu}_{25}\text{Gd}_{10}$ alloy (0.414). For γ_m , the value for the Au-based BMG is 0.774, which is also higher than that for $\text{Mg}_{65}\text{Cu}_{25}\text{Gd}_{10}$ alloy (0.730). All the GFA criteria, except for ΔT_x , show that the Au-based BMGs possess higher GFA, favorable for future development. Recently, the Mg-based BMGs have been advanced to form an amorphous rod measured around 25 mm [91]. Compared with the Mg-based BMGs, the Au-based BMGs might still on their early development stage. By adjusting or replacing other appropriate elements, much larger BMGs rod over 10 mm or even 20 mm diameter should be possible.

5.3 Bulk and micro-scale compressive behavior of Au-based BMG

As shown in Figure 4.6, the compression testing of the Au-based BMG exhibits no evidence of plastic yielding before fracture, as Mg-based BMGs. And the fracture surfaces for the specimens were examined by SEM.

For room temperature compression tests, the Pd-based and Zr-based BMGs demonstrate a pure shear fracture process and can deform with a certain level of plasticity. The limited compressive plasticity is caused by localized shear bands. The compressive fracture morphology commonly exhibits the vein-like structures spreading over the whole surfaces along the propagation of the shear band. The fracture angle is normally close to 42° . Another phenomenon worth mentioning is that the specimen with higher engineering strain has more and tenser vein-like patterns. With such a high Poisson's ratio (0.406), the Au-based BMG surprisingly shows no plasticity. Besides, Au-based BMG has higher fracture stress than $\text{Mg}_{65}\text{Cu}_{25}\text{Gd}_{10}$. That is coherent with the results of micro-hardness tests. The value of H_v micro-hardness for Au-based is 350, which is higher than the value of $\text{Mg}_{65}\text{Cu}_{25}\text{Gd}_{10}$ H_v (232).

For micro-scale compression, the deformation of the Au-based BMG micro-pillars is dominated by the emission of shear bands in a manner of “strain burst” to release the energy, similar to that in crystalline solids. The yield strengths of the 3.8 and 1 μm pillars range from 1629 to 1580 MPa, as shown Table 4.3, which are much higher than that for the bulk $\text{Au}_{49}\text{Ag}_{5.5}\text{Pd}_{2.3}\text{Cu}_{26.9}\text{Si}_{16.3}$ samples (900-1100 MPa) as shown in Table 4.3. From Table 4.3, it is evident that the strength of the micro-pillars is a function of specimen size. The improved strength is a natural consequence of decreasing defect population and, thus, reducing probability of shear band initiation in smaller samples. However, by the observation of Table 4.3, the effect of strain rate is not clear, as compared with the macro-scale compression.

The phenomenon of the strength increasing with decreasing sample size can be rationalized by the Weibull statistics. Schuster et al. [90], Wu et al. [91] and Lee et al. [92] proposed the ideas to explain. For brittle materials, the variability of their strength is expected to be based on their flaw sensitivity described by the Weibull statistics. The Weibull equation expresses the fracture probability P_f as a function of a uniaxial stress σ in the form of [93],

$$P_f = 1 - \exp \left[-V \left(\frac{\sigma - \sigma_u}{\sigma_0} \right)^m \right], \quad (8)$$

where σ_0 is a scaling parameter, m is the Weibull modulus, and V is the volume of the tested sample. The parameter σ_u represents the stress at which there is zero failure probability, and is usually taken to be zero. Using data listed in Table 4.3, and assuming V is proportion to d^3 , where d is the diameter of the pillar, the Weibull modulus is calculated to be 39.7, as shown in Figure 5.1. By the observation of Figure 4.6, for the bulk compression specimens, it shows a yielding point at the strain rate of $1 \times 10^{-4} \text{ s}^{-1}$. Thus, the value is more reliable compared with the others and selected to calculate the value of Weibull modulus. This modulus value is between the values for ductile alloys (~ 100) and brittle ceramics (~ 5) [94]. It is also within the range of the m values recently reported for the malleable $\text{Zr}_{48}\text{-Cu}_{45}\text{Al}_7$ ($m = 73.4$) [89] and brittle $(\text{Zr}_{48}\text{Cu}_{45}\text{Al}_7)_{98}\text{Y}_2$ ($m = 25.5$) [89]. The Weibull modulus value of the $\text{Mg}_{65}\text{Cu}_{25}\text{Gd}_{10}$ bulk metallic glasses alloys is 35, slightly smaller than the Au-based BMGs [94].

5.4 Viscous flow behavior for Au-based BMG

The temperature dependence of the relative displacement of the Au-based BMG is obtained by TMA operated in the compression mode at the constant stress. The transition

temperature region ΔT ($=T_{\text{finish}} - T_{\text{onset}}$) shown in the TMA curve for the Au-based BMG as shown in Figure 4.26 is smaller than the ΔT_x data obtained from the DSC trace at the same heating rate. For example, ΔT is about 37 K based on the TMA curve, and ΔT_x is about 50 K based on the DSC curve. The narrower transition temperature interval is probably due to the stress enhanced crystallization under the TMA loading.

The viscosities as a function of temperature for the Au-based and Mg-based BMGs are shown in Figure 4.27. The viscosity values for the Au-based BMG vary from 10^8 to 10^{11} Pa.s. On the other hand, the values for the Mg-based BMG vary from 10^7 to 10^9 Pa.s. The viscosity for the Au-based BMG is higher than the Mg-based BMG.

The homogeneous deformation of BMG can be described by a free-volume model developed by Spaepen [95] and Argon [51]. The stress-strain rate-temperature relationship follows:

$$\dot{\gamma} = 2 \exp\left(-\frac{\beta v^*}{v_f}\right) \left(\frac{\gamma_0 v_0}{\Omega}\right) J \exp\left(-\frac{\Delta G^m}{kT}\right) \sinh\left(\frac{\gamma_0 v_0 \tau}{2kT}\right), \quad (9)$$

where $\dot{\gamma}$ is the shear strain rate, β is a geometrical factor between 1 and 0.5, v^* is the effective hard-sphere size of the atom, v_f is the average free volume of an atom, γ_0 is the shear strain of a basic flow unit or shear transition zone (STZ), v_0 is the volume of a flow unit, Ω is the atomic volume, J is the atomic vibration frequency, ΔG^m is the thermal activation energy, k is the Boltzmann constant, T is the absolute temperature, and τ is the applied shear stress. Yang et al. [96] pointed out that Eq. (9), at low stresses and a fixed temperature Eq. (9) can be simplified to

$$\ln(\dot{\gamma}) = \frac{\gamma_0 v_0}{2kT} \tau + A, \quad (10)$$

where $A = \ln((\gamma_0 v_0 / \Omega) J) - (\beta v^* / v_f) - (\Delta G_m / kT)$ is a temperature dependent constant. It needs to be noted that the current TMA was conducted under the compressive mode. With the strain rate and the measured stress, the material constant $\gamma_0 v_0$ can be determined from by the slope in Eq. (10), as shown in Figure 5.2. Using $\gamma_0 = 0.125$ [97], the volume of a basic flow unit STZ during shear, v_0 is calculated to be 1.29 nm^3 . That is similar to the value, 1.25 nm^3 , calculated by Yang et al. [96] by high-temperature nanoindentation experiments with loading rates ranging from 0.1 to 100 mN/s.

Besides, at low stresses and a fixed strain rate, Eq. (9) can also be simplified to

$$\tau = BT + \frac{2\Delta G^m}{\gamma_0 v_0}, \quad (11)$$

where $B = (2k / \gamma_0 v_0) [\ln \dot{\gamma} - \ln((\gamma_0 v_0 / \Omega) J) + (\beta v^* / v_f)]$ is a strain rate dependent constant. The thermal activation energy of a single STZ, ΔG^m , can be determined from the intercept of the plot of Eq. (11), as shown in Figure 5.3 for a representative strain rate of 0.15 s^{-1} . The extracted thermal activation energy ΔG^m for the Au-based BMG is 1.86 eV or 179 kJ/mol. The estimated value calculated by Yang et al. [96] is about 3.2 eV or 308 kJ/mol. Those two values are of the same order of magnitude. The small activation energy for the Au-based BMG is consistent with a low inhomogeneous-homogeneous transition temperature and a lower glass transition temperature.

5.5 Hot embossing on Au-based BMG

The process of Micro-Electro-Mechanical Systems (MEMS) includes photoresist reflow technique. Hot embossing of micro-lens arrays and V-groove patterns were printed on the Au-based BMG. Table 4.4 shows the variation in band interspacing and average height under different conditions for the V-groove patterns. The values of band interspacing of the specimen at 177°C and 137 MPa for 1 minute, 5 minute, and 10 minutes are 143 μm , 148 μm , and 153 μm , respectively. It is noted that the longer the embossing time is, the better the imprinting quality is. On the other hand, the values of height of the specimen at 177°C and 62 MPa, 137 MPa, and 156 MPa for 10 minutes are 11 μm , 45 μm , and 84 μm , respectively. By the observation of Table 4.4, there is a clear trend that the forming ability increases with increasing forming time and pressure.

Table 4.5 shows the variation in height and width under different conditions for the micro-lens array. The width of the imprinted hexagonal lens at 177°C and 27 MPa, 62 MPa, and 156 MPa for 10 minutes are 183 μm , 315 μm , and 315 μm . And the height of the imprinted specimen at 177°C and 27 MPa, 62 MPa, and 156 MPa for 10 minutes are 7 μm , 21 μm , and 22 μm . From the Table 4.5, the values of width and height are almost the same for 62 MPa and 156 MPa. That implies the pressure level of 62 MPa is a good enough parameter to replicate a micro-lens array compared to others.

Due to the fact of instrument limitation, at least 20 kg, the pressure exerted on the Au-based BMG is quiet high as compared with TMA load, only 7.1 kPa. And that will cause crystallization and increase the viscosity of the Au-based BMG as shown in Figure 5.4.

To express the workability of metallic glasses in the supercooled region, the deformability d^* has been defined as [98]

$$d^*(\alpha) = \log[\eta(T_g^*)/\eta(T_{finish}(\alpha))], \quad (12)$$

where $\eta(T_{finish}(\alpha)) = \eta_{min}(\alpha)$ and $\eta(T_g^*)$ is defined as 10^{12} Pa.s by Vogel-Fulcher-Tammann (VFT) equation (8). With $\alpha = 0.167$ K/s in this study, $d^*(\alpha)$ can be calculated based on the information in Figure 4.28. In this study, the d^* value of the Au-based BMG is 4.5, only slightly lower than that of the $Mg_{58}Cu_{31}Y_{11}$ alloy ($d^* = 5.0$), but the Au-based BMGs own much better anti-oxidation and anti-corrosion abilities.

With the good anti-oxidation, anti-corrosion, and good forming ability, the Au-based BMG may be a material with high potential for the Micro-Electro-Mechanical Systems (MEMS) applications.

Chapter 6 Conclusions

- (1) The $\text{Au}_{49}\text{Ag}_{5.5}\text{Pd}_{2.3}\text{Cu}_{26.9}\text{Si}_{16.3}$ BMGs with different rod diameters from 2 to 3 mm were successfully fabricated by copper mold casting under an argon atmosphere. By the observation of transmission electron microscopy diffraction pattern, there are nano-crystalline phases among the amorphous matrix phase.
- (2) For the thermal properties of the Au-based BMG, the value of supercooled liquid region ΔT_x is 50 K and the values of glass forming criterion T_{rg} , γ , and γ_m are 0.619, 0.43, and 0.774, respectively. The Au-based BMG shows better thermal properties than the Mg-based one.
- (3) The micro-hardness H_v value of the Au-based BMG is 350, which is much higher than pure gold (<50) and the Mg-based BMG (270).
- (4) In macro-compression tests of the Au-based BMG, the average engineering stress and average engineering strain are ~970 MPa and 1.85 %, respectively. The current Au-based BMG shows no evidence of macroscopic yielding and plasticity.
- (5) For micro-compression, the strength of the micro-pillars is about 1629-1948 MPa, a prominent increase compared to ~970 MPa for the bulk specimens. In contrast to the brittle fracture in a bulk sample even with a high Poisson's ratio, these micro-pillar specimens show significant plasticity. The morphology of compressed pillar samples indicates that the number of shear bands increased with increasing sample size and strain rates.

- (6) For the Au-based BMG, the compressive strength and density of the $\text{Au}_{49}\text{Ag}_{5.5}\text{Pd}_{2.3}\text{Cu}_{26.9}\text{Si}_{16.3}$ BMG are about 970 MPa and 13.5 g/cm^3 , respectively. Therefore, the specific strength of the $\text{Au}_{49}\text{Ag}_{5.5}\text{Pd}_{2.3}\text{Cu}_{26.9}\text{Si}_{16.3}$ BMG is $72 \text{ MPa.cm}^3/\text{g}$.
- (7) With the strain rate and the measured stress, the material constant $\gamma_0 v_0$ can be determined from by the slope of the curve. Using $\gamma_0=0.125$, the volume of a basic flow unit STZ during shear, v_0 , is calculated to be 1.29 nm^3 .
- (8) The thermal activation energy of a single STZ, ΔG^m , can be determined from the intercept of the plot. The extracted thermal activation energy ΔG^m for the Au-based BMG is 1.86 eV, corresponding to 179 kJ/mol.
- (9) The viscosity values of the Au-based BMG vary from 10^8 to 10^{11} Pa.s , higher than the values of 10^7 to 10^9 Pa.s for the Mg-based BMG. And that is one reason why the Au-based BMG has higher density and micro-hardness.
- (10) From the hot embossing of the micro-lens and V-groove MEMS patterns, the current Au-based BMG shows good forming ability. With the anti-oxidation, anti-corrosion, and good forming ability, the Au-based BMG may be a material with high potential for Micro-Electro-Mechanical Systems (MEMS) applications.

References

- [1] Turnbull D, Cech RE. J Appl Phys 1950;21:804.
- [2] Clement W, Williens RH, Duwez P. Nature 1960;187.
- [3] Chen HS, Turnbull D. Appl Phys Lett 1967;10:284.
- [4] Chen HS, Krause JT, Coleman E. J Non-Cryst Solids 1975;18:157.
- [5] Kui HW, Greer AL, Turnbull D. Appl Phys Lett 1984;45:615.
- [6] Lu ZP, Liu CT, Thompson JR, Porter WD. Phys Rev Lett 2004;92:245503.
- [7] Schoroers J, Johnson WL. Appl Phys Lett 2004;84:3666.
- [8] Ponnambalam V, Poon SJ, Shiflet G. J. Appl Phys Lett 2003;83:1131.
- [9] Schroers J, Lohwongwatana B, Johnson WL, Peker A. Appl Phys Lett 2005;87:061912.
- [10] Volkertt CA, Lilleodden ET. Phil Mag 2005;86:33.
- [11] Greer JR, Nix WD. Appl Phys A 2005;80:1625.
- [12] Greer AL. Science 1995;267:1947.
- [13] Johnson WL. Prog Mater Sci 1986;30:81.
- [14] Daveis HA, Luborsky FE. Amorphous Metallic Alloys Butterworths London 1983;8.
- [15] Kavesh S, Gillman JJ, Leamy HL. Metallic Glasses ASM International Metals Park OH 1978.
- [16] Chen HS. Acta Metall 1974;22:1505.
- [17] Drehman AL, Greer AL, Turnbull D. Appl Phys Lett 1982;41:716.
- [18] Kui WH, Greer AL, Turnbull D. Appl Phys Lett 1984;45:615.
- [19] Telford M. Materials today 2004;7:36.
- [20] Inoue A, Ohtera K, Kita K, Masumoto T. Japanese J Appl Phys 1988;27: L2248.
- [21] Inoue A, Zhang T, Masumoto T. Mater Trans JIM 1990;31:177.
- [22] Inoue A, Johnson WL. Appl Phys Lett 1993;63:2342.

- [23] Inoue A, Gook JS. Mater Trans JIM 1995;36:1180.
- [24] Inoue A, Zhang T, Itoi T, Takeuchi. A. Mater Trans JIM 1997;38.
- [25] Inoue A, N. Nishiyama, and T. Matsuda, Mater Trans JIM 1996; 37.
- [26] Inoue A, Mater Trans JIM 1998;39:1001.
- [27] Zhang T, Inoue A Mater JIM 1999;40:301.
- [28] Inoue A, Mater Trans JIM 1989;3:965.
- [29] Inoue A, Mater Trans JIM 1991;32:609.
- [30] Inoue A. Mater Trans JIM 1993;34:1234.
- [31] Wang WH, Dong C, Shek CH. Mater Sci Eng 2004;44:45
- [32] Inoue A. Mater Trans JIM 1995;36:866.
- [33] Inoue A, Mater Sci Eng 1997;226:357.
- [34] Inoue A, Zhang T, Takeuchi A. Mater Sci Forum 1998;269:855.
- [35] Inoue A, Takeuchi A, T. Zhang. Metall Mater Trans 1998;29:1779.
- [36] Inoue A, Bulk Amorphous Alloys Trans Tech Publications Zurich 1998.
- [37] Inoue A, Nishiyama N. Mater Sci Eng 1997;226:401.
- [38] Chen HS, Miller CE. Rev Sci Instrum 1970;41:1237.
- [39] Lu ZP, Liu CT. Acta Mater 2002;50:3501.
- [40] Lu ZP, Liu CT. Phys Rev Lett 2003;91:115505.
- [41] Du XH, Hunag JC, Liu CT, Lu ZP. Appl Phys Lett 2007;101:086108.
- [42] Johnson WL. MRS Bull 1999;24:42.
- [43] Argon AS, Kuo HY. Mater Sci Eng 1979;39:101.
- [44] Srolovitz D, Vitek V, Egami T. Acta Metall Mater 1983;31:335.
- [45] Falk ML. Phys Rev B 1999;60:7062.
- [46] Bulatov VV, Argon AS. Model Sim Mater Sci Eng 1994;2:167.
- [47] Bulatov VV, Argon AS. Model Sim Mater Sci Eng 1994;2:185.
- [48] Bulatov VV, Argon AS. Model Sim Mater Sci Eng 1994;2:203.

- [49] Falk ML, Langer JS. Phys Rev E 1998;57:7192.
- [50] Argon AS, Shi LT, Phil Mag A 1982;46:275.
- [51] Yamamoto R, Matsuoka H, Doyama M. Phys Status Solidi A. 1979;163
- [52] Spaepen F. Acta Metall 1977;25:407.
- [53] Argon AS. Acta Metall 1979;27:47.
- [54] Cohen MH and Turnbull DJ. Chem Phys 1959;31:1164.
- [55] Polk DE, Turnbull D. Acta Metall 1972;20:493.
- [56] Shi FG, Nieh TG, Chou YT. Scripta Mater 2000;43:265.
- [57] Gilman JJ. J Appl Phys 1975;46:1625.
- [58] Li, JCM. Micromechanisms of deformation and fracture In: Metallic glasses. Materials Park, OH: American Society for Metals;1978 [Chapter 9].
- [59] Kimura H, Masumoto. Acta Metall 1983;31:231.
- [60] Steif PS, Spaepen F, Hutchinson JW. Acta Metall 1982;30:447.
- [61] Schuh CA, Nieh TG. J Mater Res 2004;19:46.
- [62] Schuh CA, Argon AS, Nieh TG, Wadsworth J. Phil Mag A 2003;83:2585.
- [63] Conner RD, Johnson WL, Paton NE, Nix WD. J Appl Phys 2003;94:904.
- [64] Pampillo CA, Chen HS. Mater Sci Eng 1974;13:181.
- [65] Hufnagel TC, Deiry PE, Vinci RP. Scripta Mater 2000;43:1071.
- [66] Moser B, Kuebler J, Meinhard H, Muster W, Michler J. Adv Eng Mater 2005;7:388.
- [67] Conner RD, Li Y, Nix WD, Johnson WL. Acta Mater 2004;52:2429.
- [68] Davis LA. Metallic Glasses Metals Park OH ASM 1978:191.
- [69] Ashby MF, Greer AL. Scripta Mater 2006;54:321.
- [70] Cambridge Materials Selector (software), Granta Design Ltd, Cambridge, UK.
- [71] Inoue A, Shen BL, Koshiba H, Kato H, Yavari AR. Nature Mater 2003;2:661.
- [72] Lewandowski JJ, Wang WH, Greer AL. Phil Mag Lett 2005;85:77.
- [73] Xing LQ, Li Y, Ramesh KT, Li J, Hufnagel TC. Phys Rev B 2001;64:180201.

- [74] Chen HS, Turnbull D. Appl Phys Lett 1967;10:284.
- [75] Chen HS, Turnbull D. J Chem Phys 1968;48:2560.
- [76] Lewandowski JJ, Wang WH, Greer AL. Phil Mag Lett 2005;85:77.
- [77] Schroers J, Johnson WL. Phys Rev Lett 2004;93:255506.
- [78] Busch R, Bakke E, Johnson WL. Acta Mater 1998;46:4725.
- [79] Kawamura Y, Inoue A. Mater Sci Forum 1999; 4:373.
- [80] Busch R, Bakke E, Johnson WL. Acta Mater 1998;46:4725.
- [81] Busch R, Liu W, Johnson WL. J. Appl Phys 1998;83:4134.
- [82] Chen HS. J Non-Cryst Solids 1978;27:257.
- [83] Fan GJ, Fecht HJ, Lavernia E. J Appl Phys Lett 2004;84:487.
- [84] Kawamura Y, Nakamura T, Inoue A, Masumoto T. Mater Trans JIM 1999;40:74.
- [85] Yamasaki T, Tatibana T, Ogino Y, Inoue A. Mater Res Soc Symp Proc 1999;554:63.
- [86] Stefan MJ. Akad Wiss Wien Math-Nat Klasse Abt 2 1874;69:713.
- [87] Michael, Uchick D, Dennis, Dimiduk M. Mater Sci Eng 2005;268:400.
- [88] Pan CT, Wu TT, Chen MF, Chang YC, Lee CJ, Huang JC. Sensor and Actuators
2008;141:422
- [89] Zheng Q, Xu J, Ma E. J. Appl Phys 2007;102:113519.
- [90] Schuster BE, Wei Q, Ervin MH, Hruszkewycz SO, Miller. Scripta Mater 2007;57:517.
- [91] Wu WF, Li Y.S. Phil Mag 2008;88:71.
- [92] Lee CJ, Huang JC, Nieh TG. Appl Phys Lett 2007;91:161913.
- [93] Weibull WJ. J Appl Mech 1951;18:293.
- [94] Askeland DR. Science and Engineering of Materials PWS Publishing Boston 1994:152.
- [95] Spaepen F. Acta Metall 1976;25:407
- [96] Yang B, Wadsworth J, Nieh TG. Appl Phy Lett 2007;90:061911.
- [97] Argon AS, Shi LT. Acta Metall 1983;31:499.
- [98] Kato H, Wada T, Hasegawa M, Saida J, Inoue A, Chen HS. Scripta Mater 2006;54:2023.

Table 2.1 Bulk metallic glasses and their developed year [30].

BMG system	Years
Pd–Cu–Si	1974
Pt–Ni–P	1975
Au–Si–Ge	1975
Pd–Ni–P	1982
Mg–Ln–Cu (Ln = lanthanide metal)	1988
Ln–Al–TM (TM = group transition metal)	1989
Zr–Ti–Al–TM	1990
Ti–Zr–TM	1993
Zr–Ti–Cu–Ni–Be	1993
Nd(Pr)–Al–Fe–Co	1994
Zr–(Nb, Pd)–Al–TM	1995
Cu–Zr–Ni–Ti	1995
Fe–(Nb, Mo)–(Al, Ga)–(P, C, B, Si, Ge)	1995
Pd–Cu(Fe)–Ni–P	1996
Co–(Al, Ga)–(P, B, Si)	1996
Fe–(Zr, Hf, Nb)–B	1996
Co–Fe–(Zr, Hf, Nb)–B	1996
Ni–(Zr, Hf, Nb)–(Cr, Mo)–B	1996
Ti–Ni–Cu–Sn	1998
LaAlNiCuCo	1998
Ni–Nb	1999
Ni–(Nb, Cr, Mo)–(P, B)	1999
Zr-based glassy composites	1999
Zr–Nb–Cu–Fe–Be	2000
Fe–Mn–Mo–Cr–C–B	2002
Ni–Nb–(Sn, Ti)	2003
Pr(Nd)–(Cu, Ni)–Al	2003

Table 2.2 The composition of representative BMG systems, their glass transition temperature, T_g , onset temperature of crystallization, T_x , and onset melting point, T_m , and glass forming ability represented by reduced glass transition temperature, T_{rg} [30].

BMG	T_g (K)	T_x (K)	T_m (K)	T_{rg}
Mg ₈₀ Ni ₁₀ Nd ₁₀	454.2	477.7	725.8	0.63
Mg ₆₅ Ni ₂₀ Nd ₁₅	459.3	501.4	743.0	0.62
Mg ₇₅ Ni ₁₅ Nd ₁₀	450.0	482.8	717.0	0.63
Mg ₇₀ Ni ₁₅ Nd ₁₅	467.1	494.1	742.5	0.63
Mg ₆₅ Cu ₂₅ Y ₁₀	424.5	484.0	727.9	0.58
Zr _{41.2} Ti _{13.8} Cu _{12.5} Ni ₁₀ Be _{22.5}	623.0	705.0	932.0	0.67
Zr _{46.25} Ti _{8.25} Cu _{7.5} Ni ₁₀ Be _{27.5}	622.0	727.0	909.0	0.68
Zr _{45.38} Ti _{9.62} Cu _{8.75} Ni ₁₀ Be _{26.25}	623.0	740.0	911.0	0.68
Zr _{42.63} Ti _{12.37} Cu _{11.25} Ni ₁₀ Be _{23.75}	623.0	712.0	933.0	0.67
Zr ₄₄ Ti ₁₁ Cu ₁₀ Ni ₁₀ Be ₂₅	625.0	739.0	917.0	0.68
Zr _{38.5} Ti _{16.5} Ni _{9.75} Cu _{15.25} Be ₂₀	630.0	678.0	921.0	0.68
Zr ₄₈ Nb ₈ Cu ₁₂ Fe ₈ Be ₂₄	658	751	1009	0.65
Zr ₄₈ Nb ₈ Cu ₁₄ Ni ₁₂ Be ₁₈	656	724	997	0.66
Zr ₅₇ Ti ₅ Al ₁₀ Cu ₂₀ Ni ₈	676.7	725.4	1095.3	0.62
Zr ₅₇ Nb ₅ Cu _{15.4} Ni _{12.6} Al ₁₀	687	751	1092	0.63
Zr ₅₃ Ti ₅ Cu ₁₆ Ni ₁₀ Al ₁₆	697	793	1118	0.62
Zr ₆₆ Al ₈ Cu ₇ Ni ₁₉	662.3	720.7	1117.3	0.59
Zr ₆₆ Al ₈ Cu ₁₂ Ni ₁₄	655.1	732.5	1109.1	0.59
Zr ₆₆ Al ₉ Cu ₁₆ Ni ₉	657.2	736.7	1110.9	0.59
Zr ₆₆ Al ₈ Ni ₂₆	672.0	707.6	1188.5	0.57
Zr ₆₅ Al _{7.5} Cu _{17.5} Ni ₁₀	656.5	735.6	1108.6	0.59
Pd ₄₀ Ni ₄₀ P ₂₀	590.0	671.0	877.3	0.67
Pd _{81.5} Cu ₂ Si _{16.5}	633.0	670.0	1008.8	0.63
Pd ₄₀ Cu ₃₀ Ni ₁₀ P ₂₀	586.0	678.0	744.8	0.79
Pd _{42.5} Cu ₃₀ Ni _{7.5} P ₂₀	574.0	660.0	808.0	0.71
Pd _{77.5} Cu ₆ Si _{16.5}	637.0	678.0	1019.4	0.62
Pd _{42.5} Cu _{27.5} Ni ₁₀ P ₂₀	572.0	666.0	752.0	0.76
Cu ₆₀ Zr ₃₀ Ti ₁₀	713.0	763.0	1110.0	0.64
Cu ₅₄ Zr ₂₇ Ti ₉ Be ₁₀	720.0	762.0	1090.0	0.66
Cu ₆₀ Zr ₂₀ Hf ₁₀ Ti ₁₀	754	797	1189	0.63
La ₆₆ Al ₁₄ Cu ₂₀	395.0	449.0	681.9	0.58
La ₅₅ Al ₂₅ Ni ₂₀	490.8	555.1	711.6	0.69
La ₅₅ Al ₂₅ Ni ₁₀ Cu ₁₀	467.4	547.2	662.1	0.71
La ₅₅ Al ₂₅ Cu ₂₀	455.9	494.8	672.1	0.68
La ₅₅ Al ₂₅ Ni ₅ Cu ₁₀ Co ₅	465.2	541.8	660.9	0.70
Nd ₆₀ Al ₁₀ Cu ₁₀ Fe ₂₀	485.0	610.0	773.0	0.63
Nd ₆₀ Al ₁₅ Ni ₁₀ Cu ₁₀ Fe ₅	430.0	475.0	709.0	0.61
Nd ₆₁ Al ₁₁ Ni ₈ Co ₅ Cu ₁₅	445.0	469.0	729.0	0.61
Ti ₃₄ Zr ₁₁ Cu ₄₇ Ni ₈	698.4	727.2	1119.0	0.62
Ti ₅₀ Ni ₂₄ Cu ₂₀ B ₁ Si ₂ Sn ₃	726.0	800.0	1230.0	0.59
Au _{77.8} Si _{8.4} Ge _{13.8}	293.0	293.0	606.0	0.48
Pr ₆₀ Cu ₂₀ Ni ₁₀ Al ₁₀	409	452	705	0.58
Pr ₅₅ Al ₁₂ Fe ₃₀ Cu ₃	551	626	845	0.65

Most of data were obtained by DSC or/and DTA at a heating rate of 20 K/min.

Table 2.3 Properties of the elements in the Au-based BMG alloy.

Symbol	Atomic weight	Structure	Atomic radius (pm)	Melting point (°C)	Density (g/cm ³)
Au	197	FCC	135	1064	19.3
Ag	108	FCC	160	962	10.1
Pd	106	FCC	140	1552	12.0
Cu	64	FCC	128	1085	8.9
Si	28	Diamond	110	1410	2.3

Table 2.4 Possible application fields for BMGs [30].

Properties	Application field
High strength	Machinery structural materials
High hardness	Cutting materials
High fracture toughness	Die materials
High impact fracture energy	Tool materials
High fatigue strength	Bonding materials
High elastic energy	Sporting goods materials
High corrosion resistance	Corrosion resistance materials
High wear resistance	Writing appliance materials
High reflection ratio	Optical precision materials
High hydrogen storage	Hydrogen storage materials
Good soft magnetism	Soft magnetic materials
High frequency permeability	High magnetostrictive materials
Efficient electrode	Electrode materials
High viscous flowability	Composite materials
High acoustic attenuation	Acoustic absorption materials
Self-sharpening property	Penetrator
High wear resistance and manufacturability	Medical devices materials

Table 4.1 The composition analyses of the $\text{Au}_{49}\text{Ag}_{5.5}\text{Pd}_{2.3}\text{Cu}_{26.9}\text{Si}_{16.3}$ rods by SEM/EDS.

	Au (at%)	Ag (at%)	Pd (at%)	Cu (at%)	Si (at%)
EDS composition 1	53.9	5.4	2.4	22.7	15.6
EDS composition 2	54.7	5.3	2.3	23.4	14.3
EDS composition 3	54.5	5.7	1.7	25.0	13.0
EDS composition 4	55.0	5.1	2.0	25.0	12.9
Average composition	54.5	5.4	2.1	23.8	14.0
Desighed composition	49.0	5.5	2.3	26.9	16.3

Table 4.2 Summary of the macro-compressive of Au-based BMG at different strain rates.

	$\dot{\epsilon} \sim 5 \times 10^{-5} \text{ s}^{-1}$	$\dot{\epsilon} \sim 1 \times 10^{-4} \text{ s}^{-1}$	$\dot{\epsilon} \sim 5 \times 10^{-4} \text{ s}^{-1}$	$\dot{\epsilon} \sim 1 \times 10^{-3} \text{ s}^{-1}$
Fracture strength (MPa)	1003	1122	933	827
Fracture elongation (%)	1.85	1.97	1.59	2.00

Table 4.3 Summary of the micro-compressive of Au-based BMG at different strain rates.

	$\dot{\epsilon} \sim 10^{-5} \text{ s}^{-1}$	$\dot{\epsilon} \sim 1 \times 10^{-4} \text{ s}^{-1}$	$\dot{\epsilon} \sim 1 \times 10^{-3} \text{ s}^{-1}$	$\dot{\epsilon} \sim 1 \times 10^{-2} \text{ s}^{-1}$	$\dot{\epsilon} \sim 6 \times 10^{-2} \text{ s}^{-1}$
Au base BMG, 1 μm (MPa)	--	--	1657	1941	1948
Input Depth (Response), nm	--	--	180 (266)	180 (362)	180 (456)
Au base BMG, 3.8 μm (MPa)	1409	2020	1689	1761	1629
Input Depth (Response), nm	600 (1230)	600 (2266)	600 (1469)	600 (1880)	600 (812)

Table 4.4 Variation in distance and average height under different conditions for V-groove.

	Pressure (MPa)	Time (min)	Band interspacing (μm)	Height (μm)
Mold	-	-	-	94
	137	1	143	38
177 K	137	5	148	52
	137	10	153	45
	62	10	-	11
177 K	137	10	153	45
	156	10	147	84

Table 4.5 Variation in height and width under different conditions for micro-lens array.

	Width (μm)	Height (μm)
Mold	330	24
27 MPa	183	7
62 MPa	315	21
156 MPa	315	22

Table 5.1 The negative heat of mixing in unit of kJ/mol of the Au, Ag, Pd, Cu, and Si elements.

	Au	Ag	Pd	Cu	Si
Au	-	-	0	-9	-30
Ag	-	-	-7	2	-20
Pd	0	-7	-	-14	-55
Cu	-9	2	-14	-	-19
Si	-30	-20	-55	-19	-

Table 5.2 Thermal properties of the $\text{Mg}_{65}\text{Cu}_{25}\text{Gd}_{10}$ (Mg-based BMG) and $\text{Au}_{49}\text{Ag}_{5.5}\text{Pd}_{2.3}\text{Cu}_{26.9}\text{Si}_{16.3}$ (Au-based BMG) obtained from DSC at a heating rate of 10 K/min.

	T_g (K)	T_x (K)	ΔT_x (K)	T_m (K)	T_l (K)	ΔT_m (K)	T_{rg}	γ	γ_m
Mg-based BMG	410	470	60	679	726	47	0.565	0.414	0.730
Au-based BMG	400	450	50	625	646	21	0.619	0.430	0.774

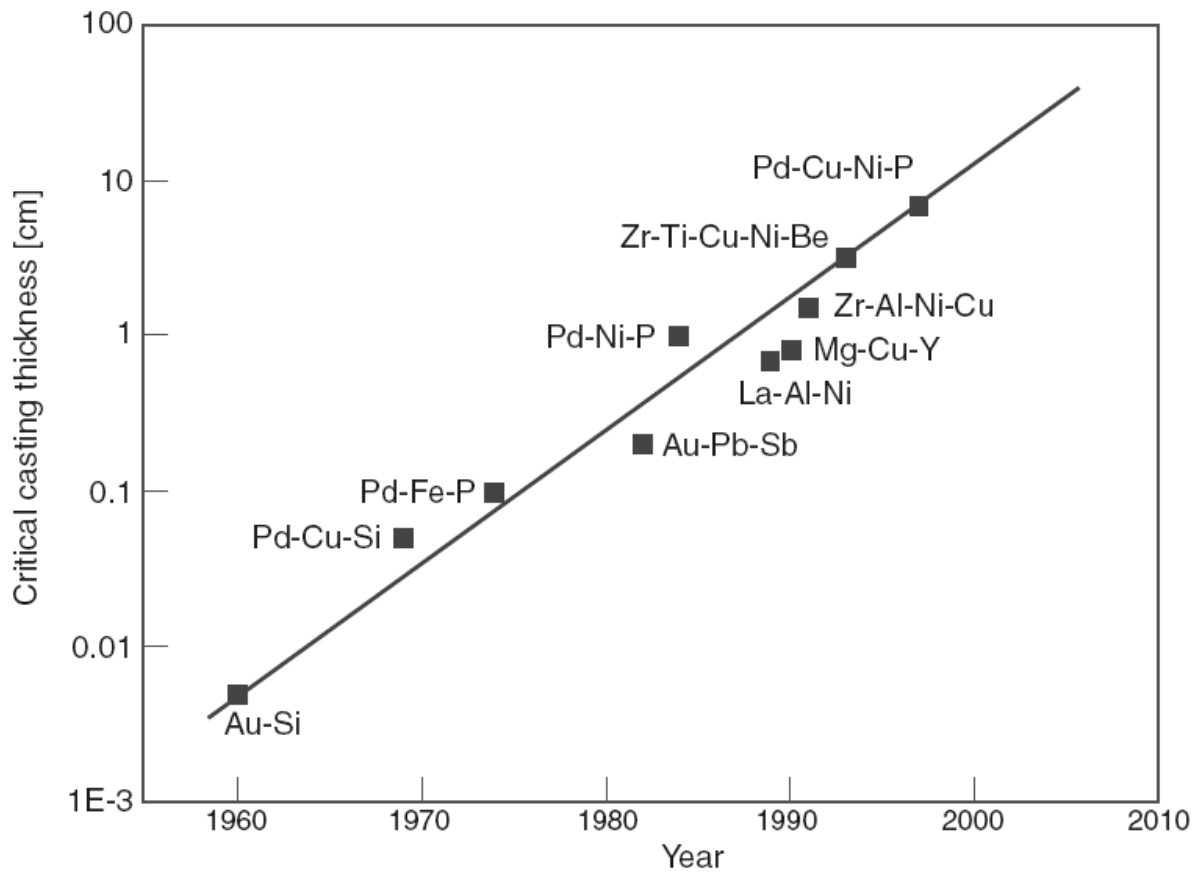


Figure 2.1 The critical casting thickness versus the year in which alloys were discovered. Over 40 years, the critical casting thickness has increased by more than three orders of magnitude [19].

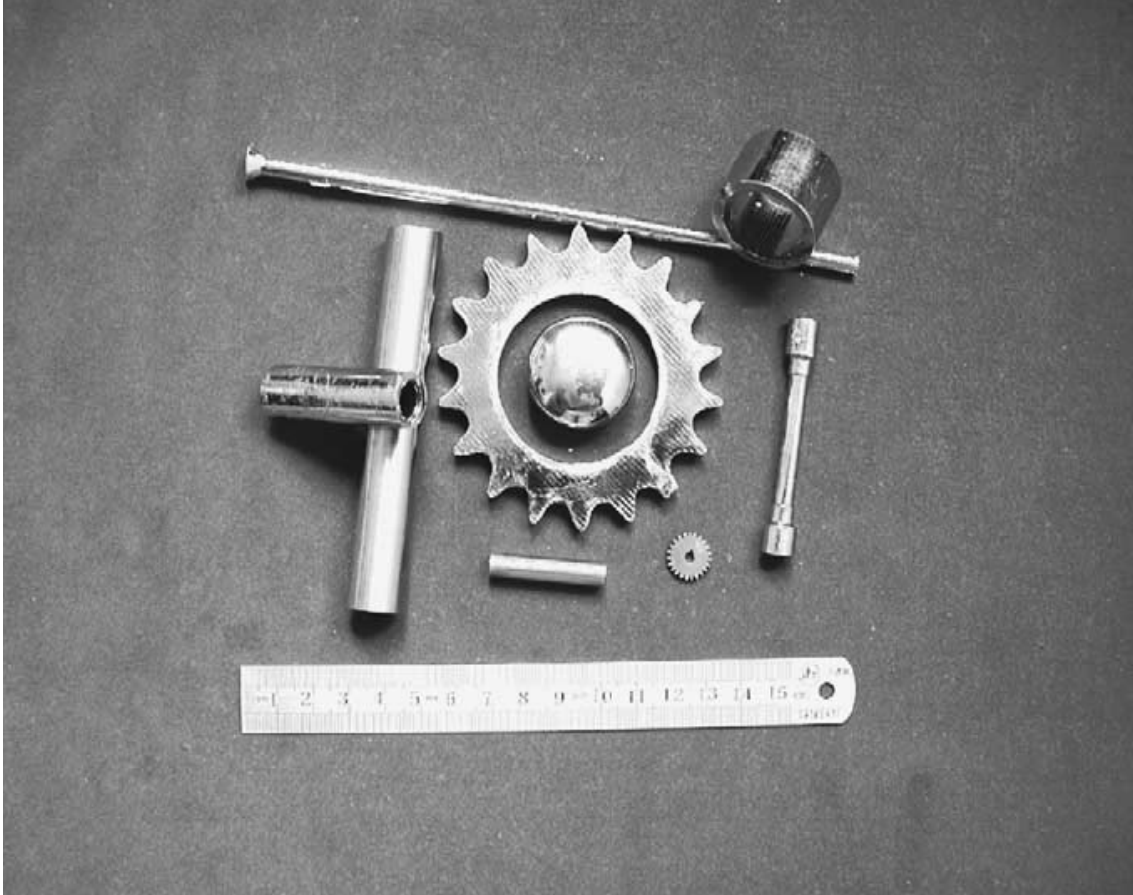


Figure 2.2 The picture of as-cast alloy BMG system [30].

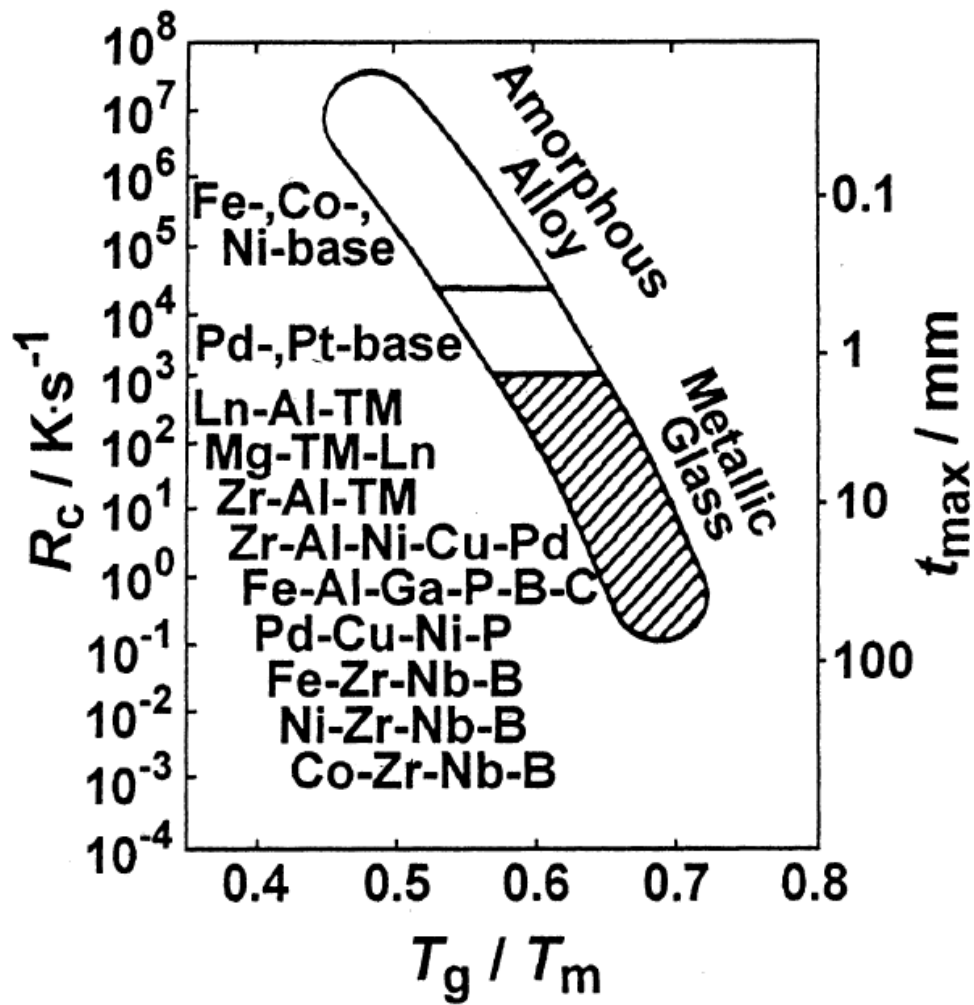


Figure 2.3 Relationship between the critical cooling rate for glass formation (R_c), maximum sample thickness for glass formation (t_{\max}) and reduced glass transition temperature (T_g/T_m) for bulk amorphous alloys. The data of the ordinary amorphous alloys, which require high cooling rates for glass formation, are also shown for comparison [31].

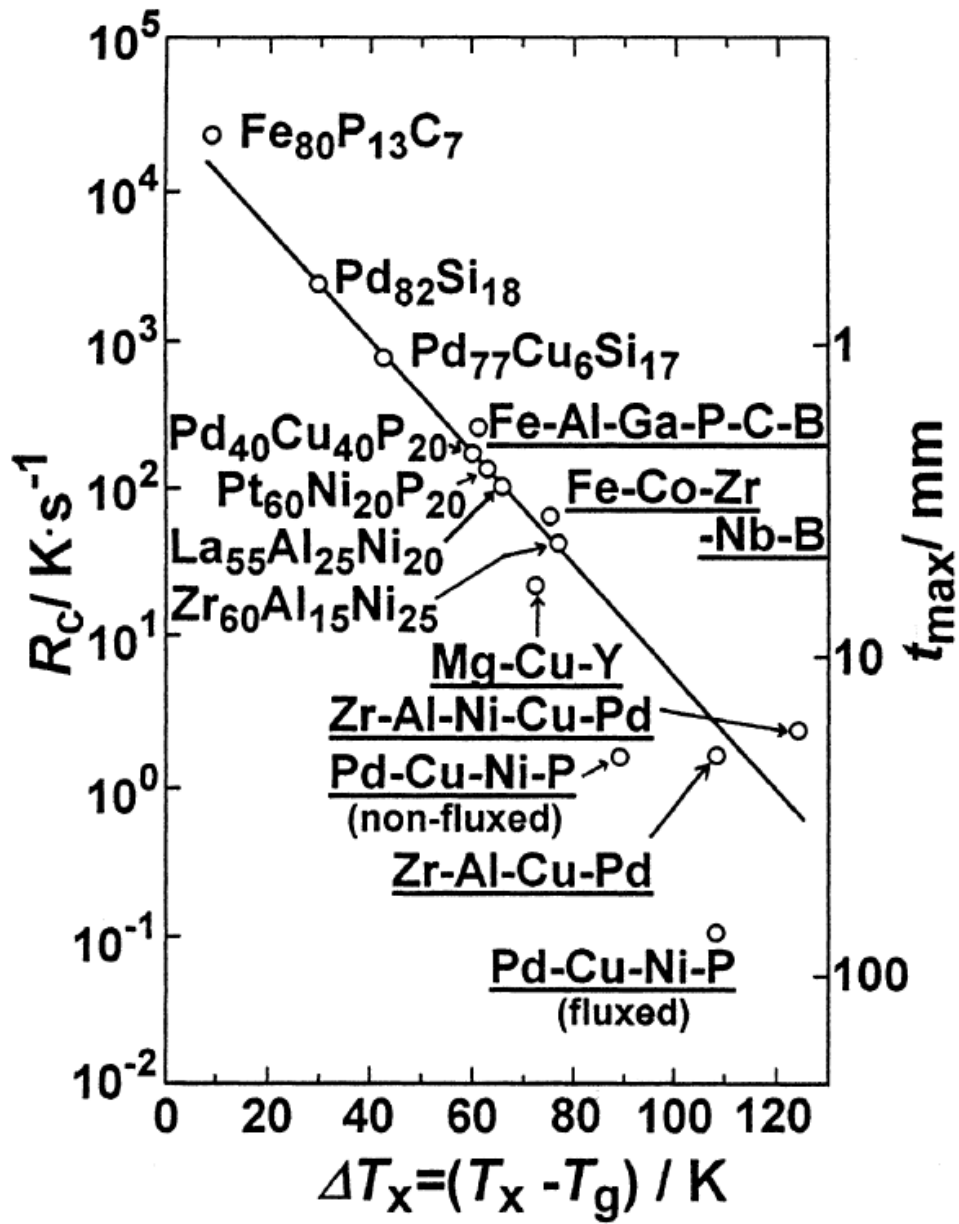


Figure 2.4 Relationship between R_c , t_{max} and the temperature interval of the supercooled liquid region between T_g and T_x for bulk amorphous alloys [31].

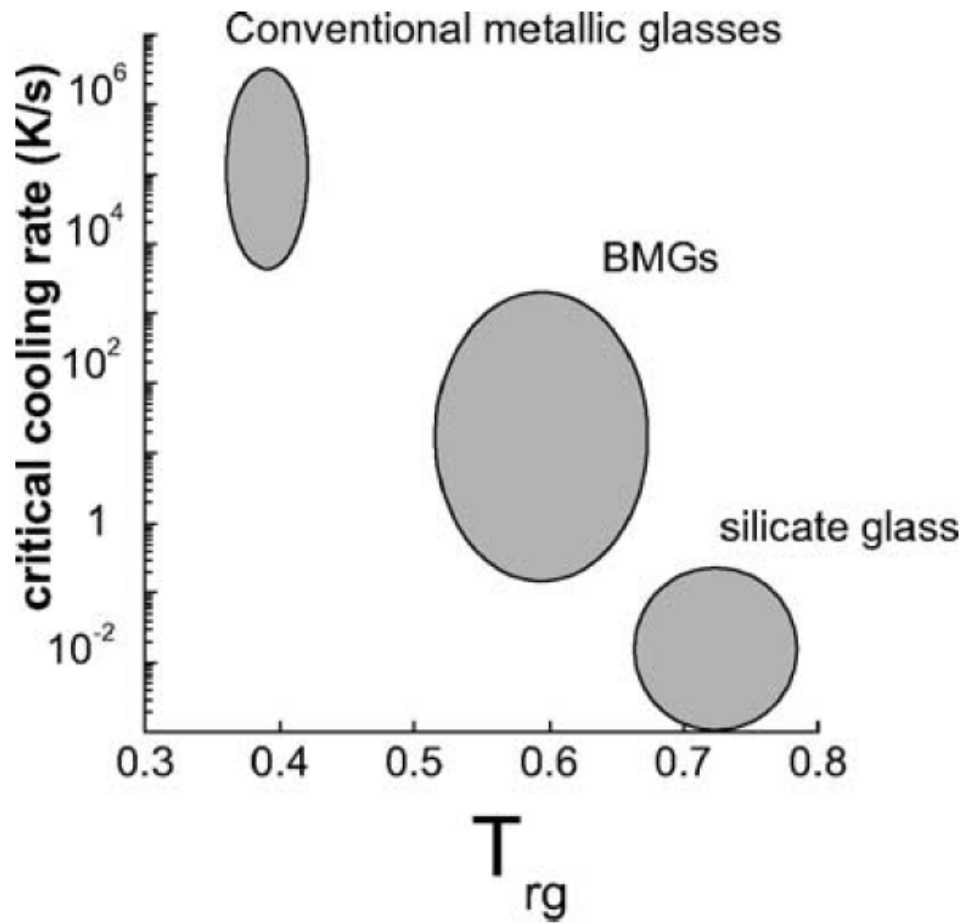


Figure 2.5 A comparison of critical cooling rate between reduced glass transition temperature, T_{rg} , among BMG, silicate glasses and conventional metallic glasses [30].

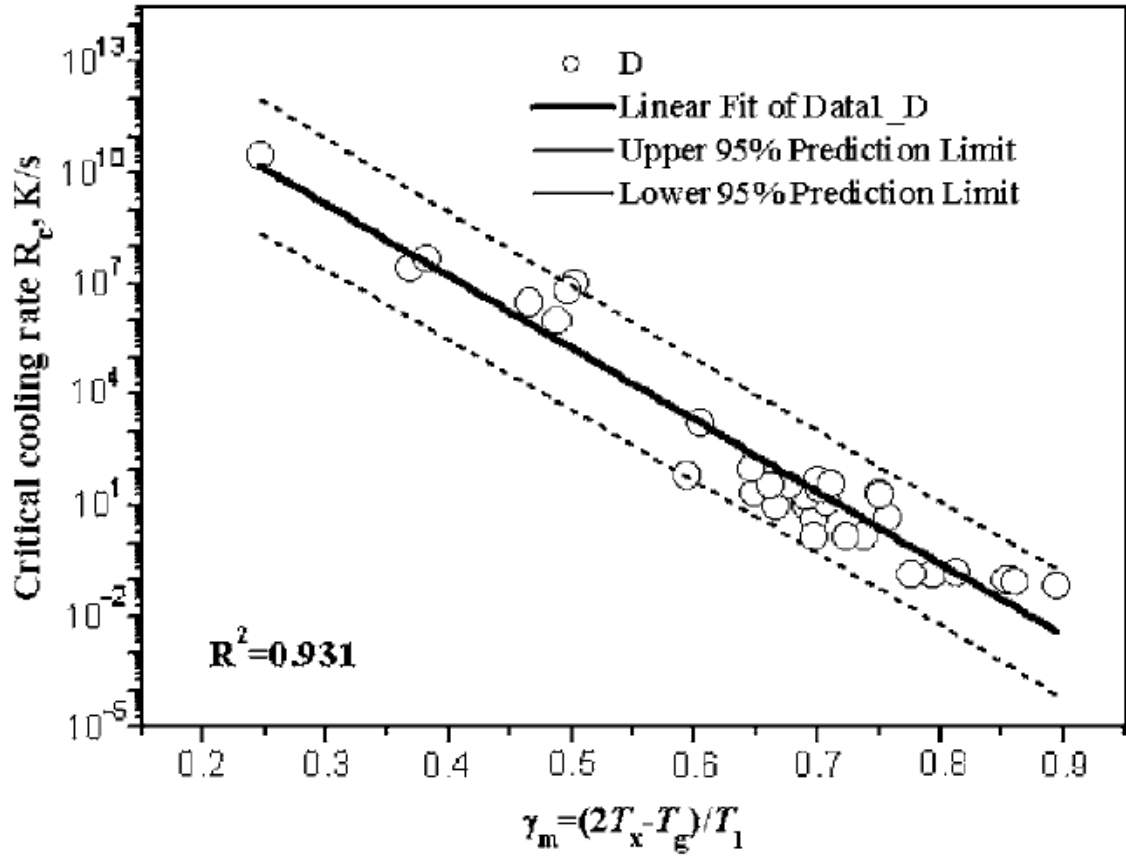


Figure 2.6 The correlation between the critical cooling rate and the parameter γ_m for metallic glasses [39].

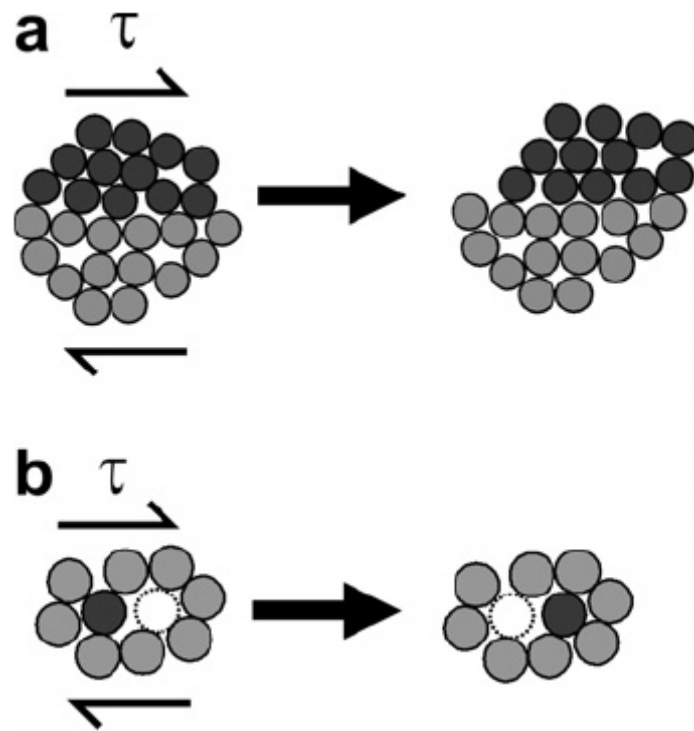


Figure 2.7 Two-dimensional schematics of the atomistic deformation mechanisms proposed for amorphous metals, including (a) a shear transformation zone (STZ), after Argon [40], and (b) a local atomic jump, after Spaepen [50].

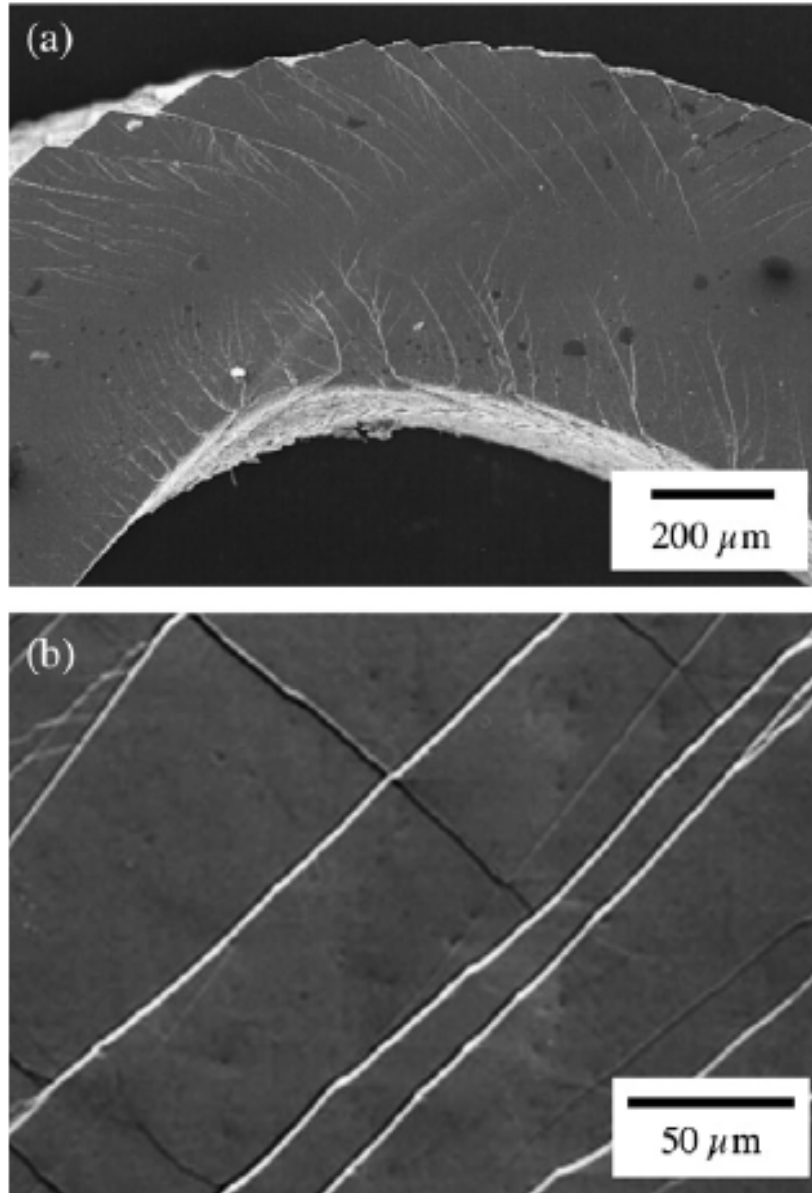


Figure 2.8 Scanning electron micrographs illustrating the “slip steps” or surface offsets associated with shear bands in deformed metallic glasses. In (a), a bent strip of $\text{Zr}_{57}\text{Nb}_5\text{Al}_{10}\text{Cu}_{15.4}\text{Ni}_{12.6}$ illustrates slip steps formed in both tensile and compressive modes of loading, on the top and bottom surfaces, respectively. In (b) the side of a compression specimen of $\text{Zr}_{52.5}\text{Cu}_{17.9}\text{Ni}_{14.6}\text{Al}_{10}\text{Ti}_5$ is shown, for which the loading axis was vertical; here the slip steps document shear deformation at an inclined angle to the applied compressive load [63].

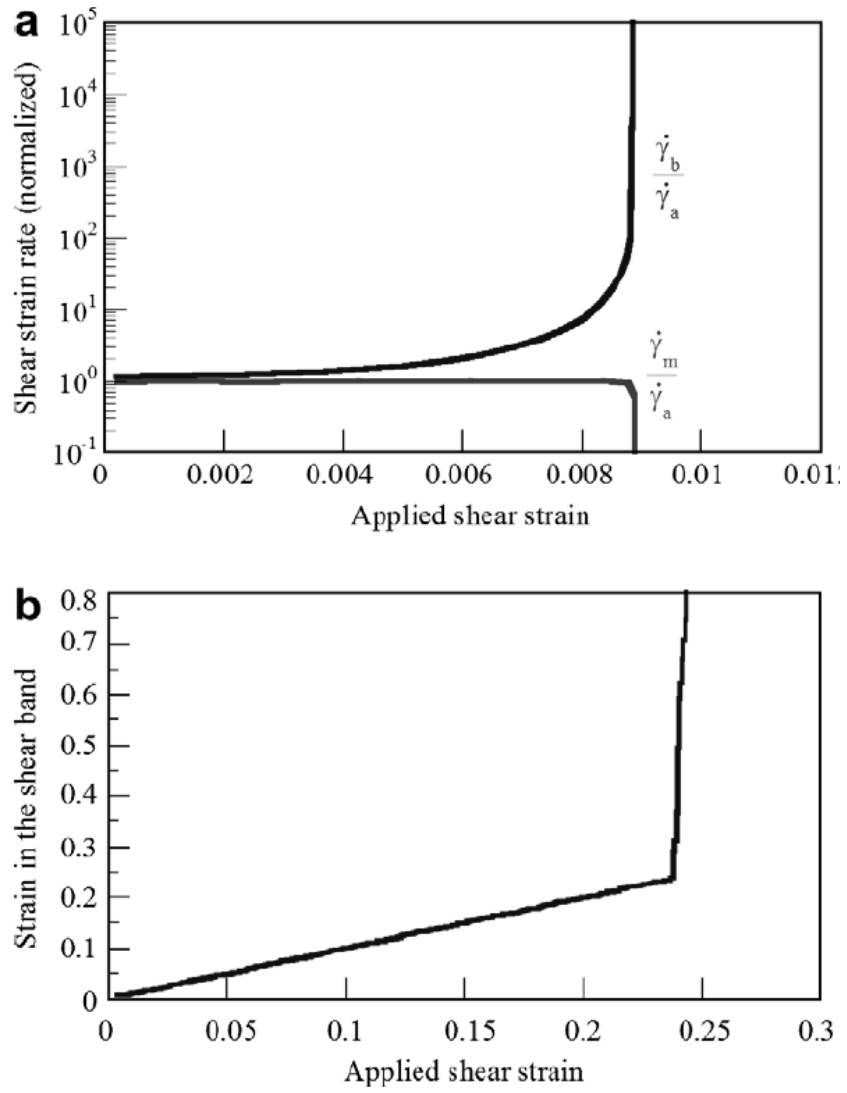


Figure 2.9 Calculations from the work of (a) Argon and (b) Steif et al. illustrating the process of strain localization in metallic glasses. In (a), a history of strain rate is shown for both the forming shear band and the surrounding matrix; these quantities are normalized by the applied shear strain rate. In (b), the history of strain in the shear band is shown [51, 64].

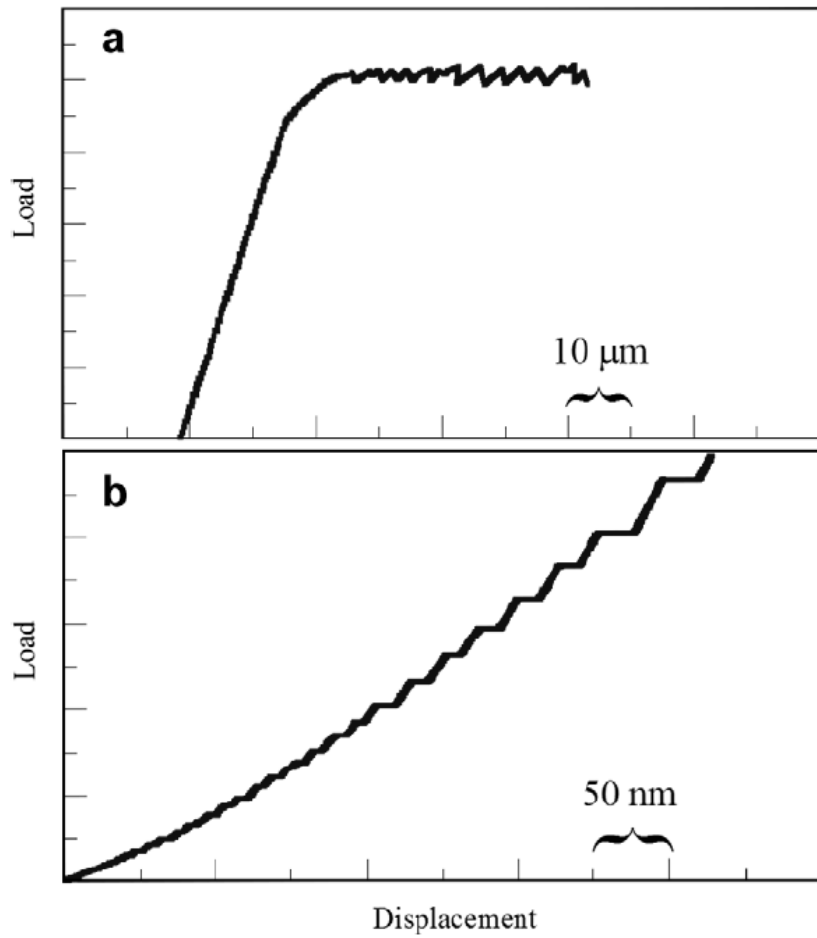


Figure 2.10 Examples of mechanical test data that illustrate serrated flow of metallic glasses, through repeated shear band operation in confined loading. In (a), the compression response of a $\text{Pd}_{77.5}\text{Cu}_6\text{Si}_{16.5}$ specimen of low aspect ratio is shown, while (b) is an instrumented indentation curve for $\text{Pd}_{40}\text{Cu}_{30}\text{Ni}_{10}\text{P}_{20}$ glass. Because (a) represents a displacement controlled experiment, serrations are represented as load drops, while the load-controlled experiment in (b) exhibits displacement bursts [65].

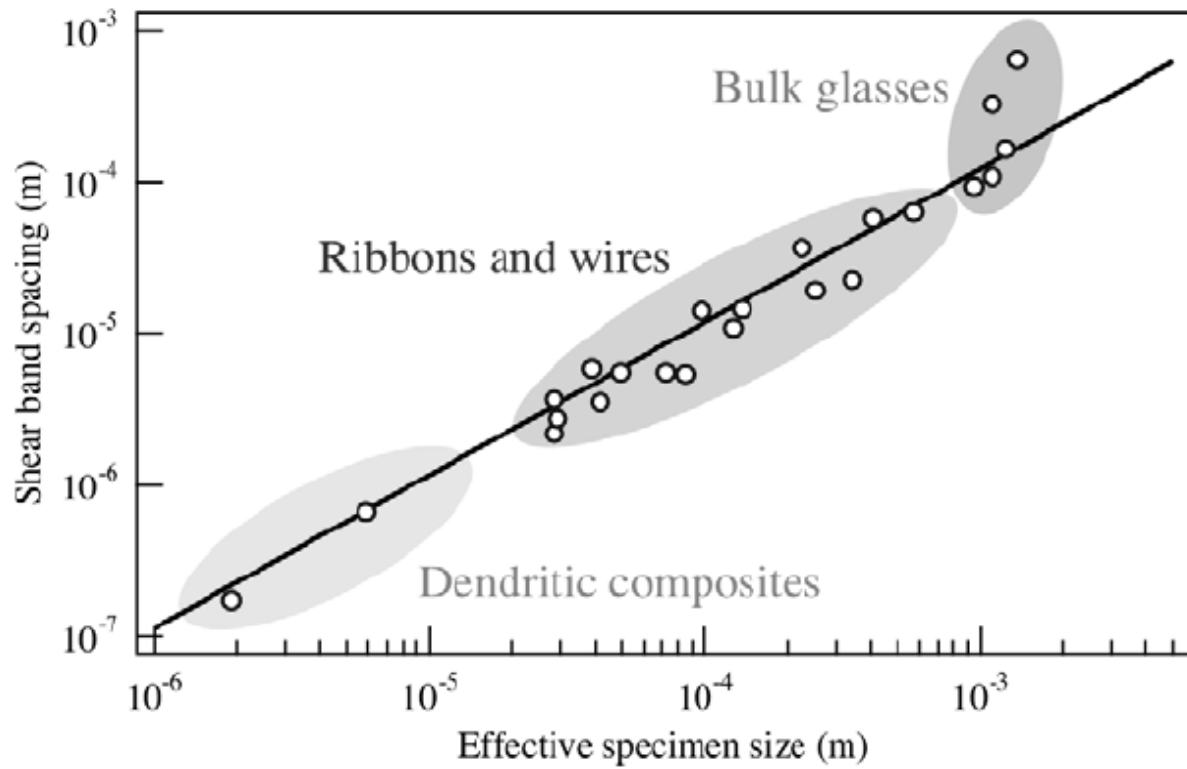


Figure 2.11 Average shear band spacings are plotted as a function of characteristic specimen dimensions for a variety of metallic glasses (and some derivative composites) deformed in constrained modes of loading, after Conner et al [67].

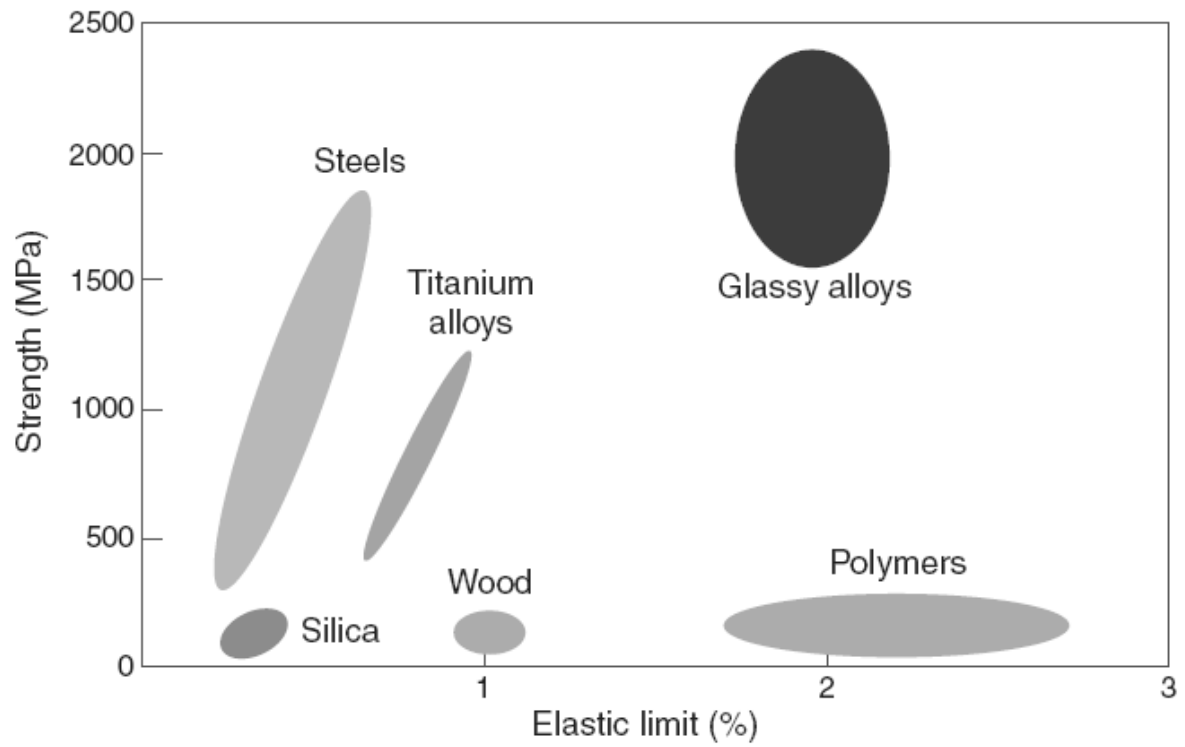


Figure 2.12 Amorphous metallic alloys combine higher strength than crystalline metal alloys with the elasticity of polymers [19].

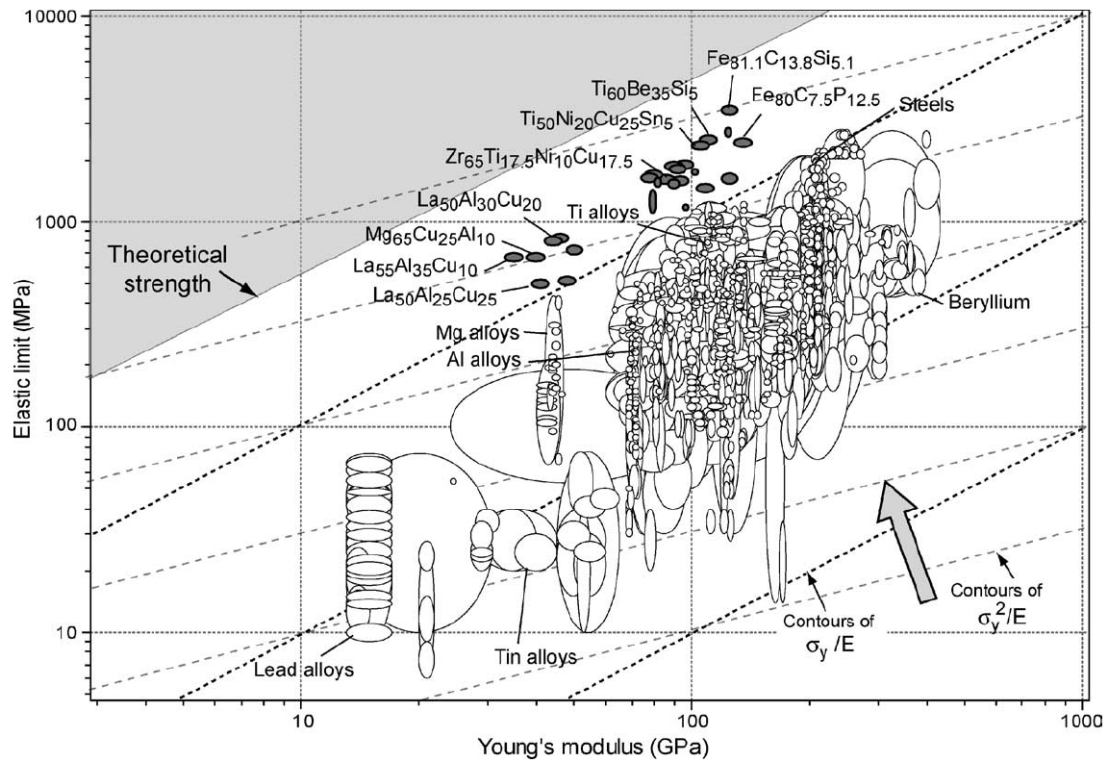


Figure 2.13 Elastic limit σ_y plotted against modulus E for 1507 metals, alloys, metal matrix composites and metallic glasses. The contours show the yield strain σ_y/E and the resilience σ_y^2/E [73].

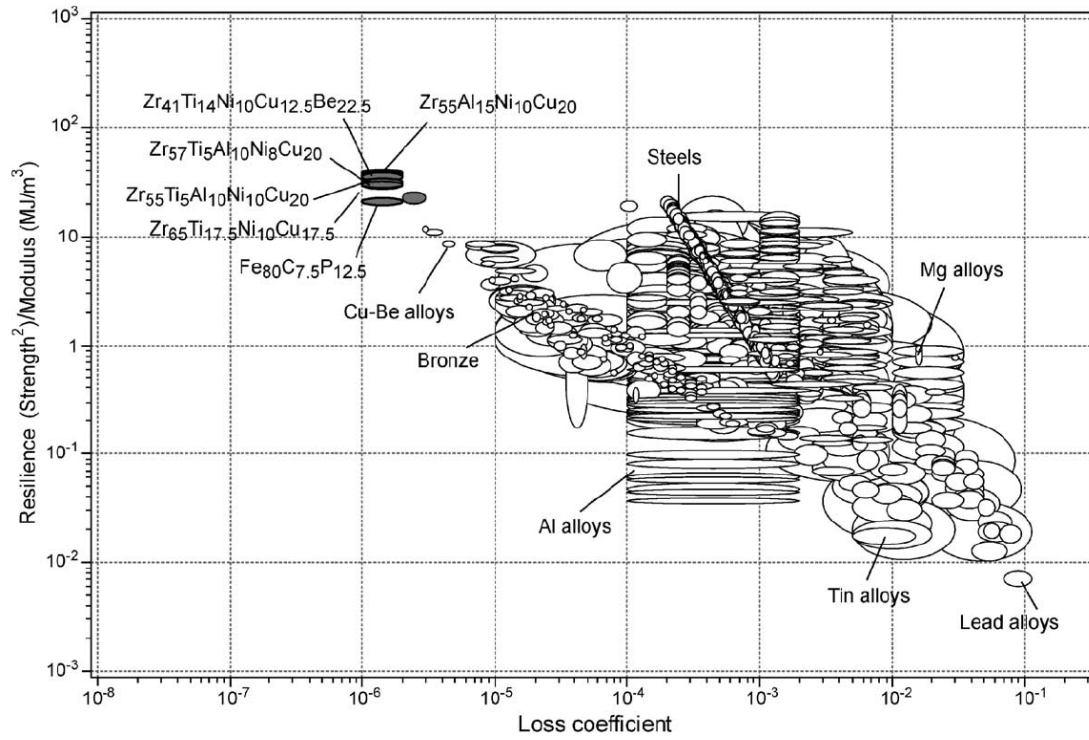
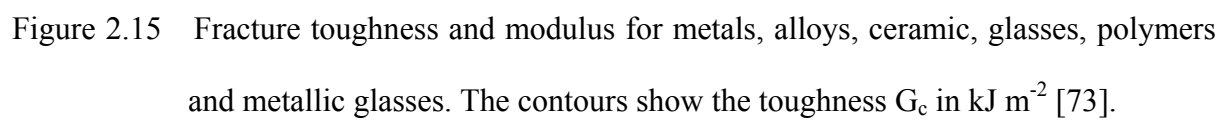


Figure 2.14 Resilience σ_y^2/E and loss coefficient for the same materials as Figure 2.13 [73].



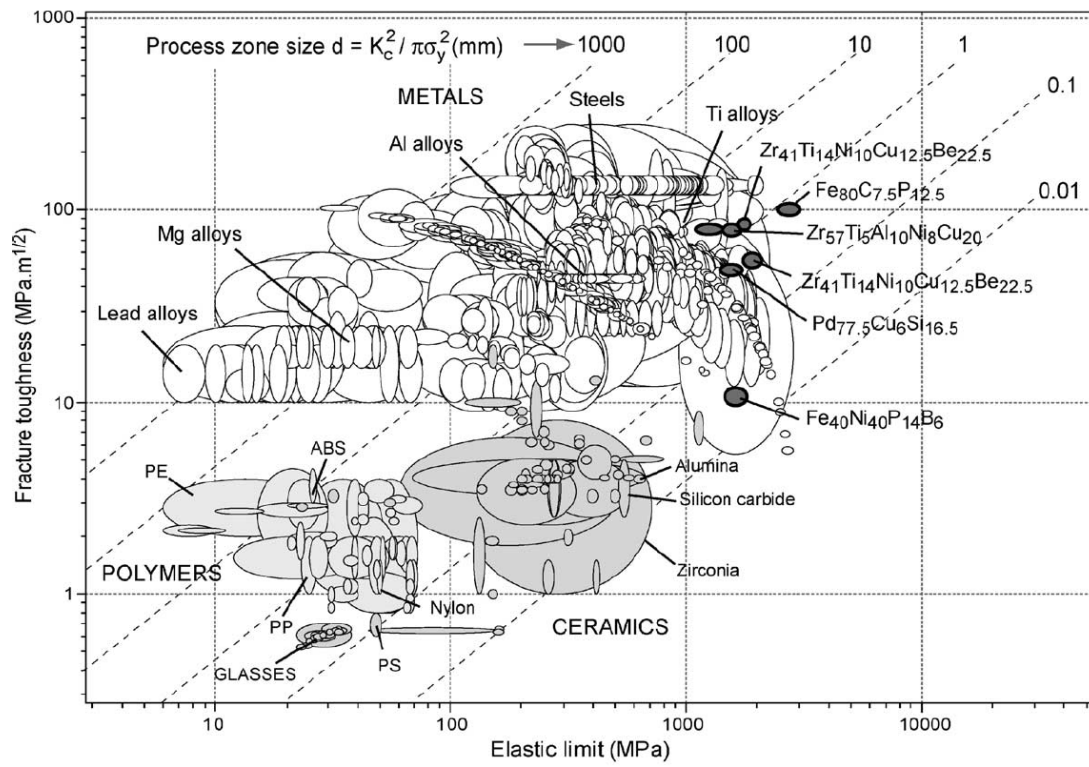


Figure 2.16 Toughness and elastic limit for the same materials. The contours show the process-zone size d in mm [73].

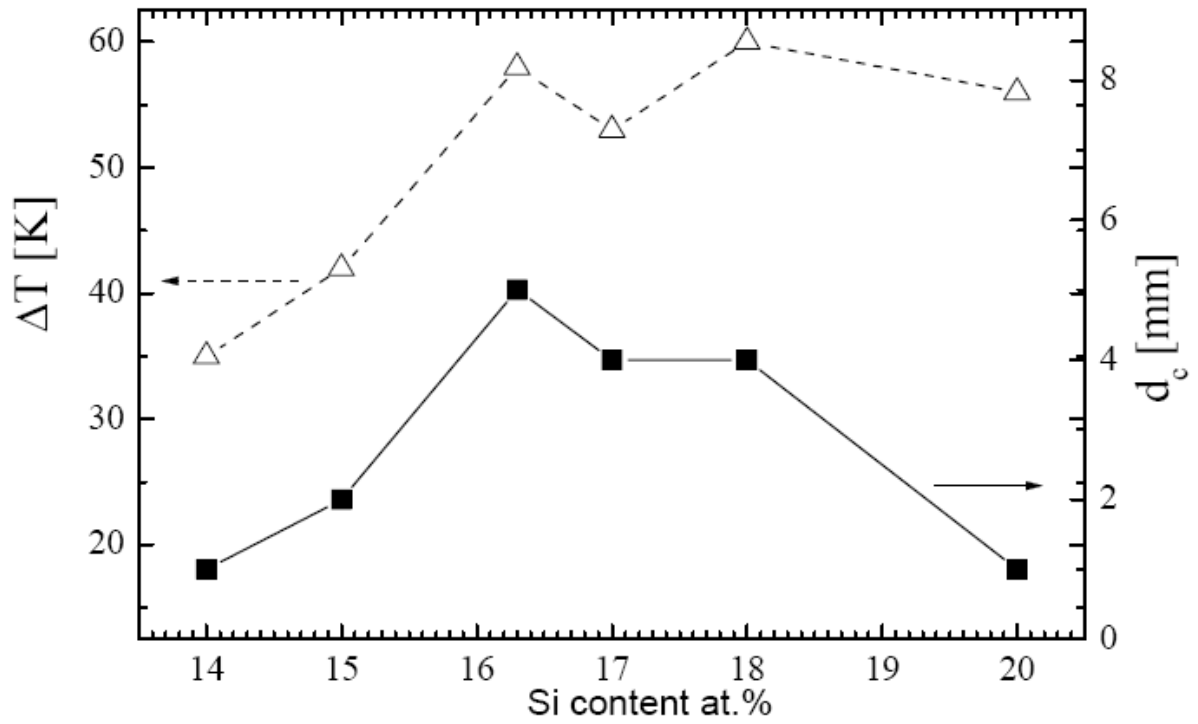


Figure 2.17 Composition dependence of ΔT and d_c for $(\text{Au}_{58.5}\text{Ag}_{6.6}\text{Pd}_{2.8}\text{Cu}_{32.1})_{86-x}\text{Si}_{14+x}$ for $x = 0\text{-}6\%$. A strong dependence on the Si content of both d_c and ΔT is observed. No obvious correlation of d_c and ΔT is seen [9].

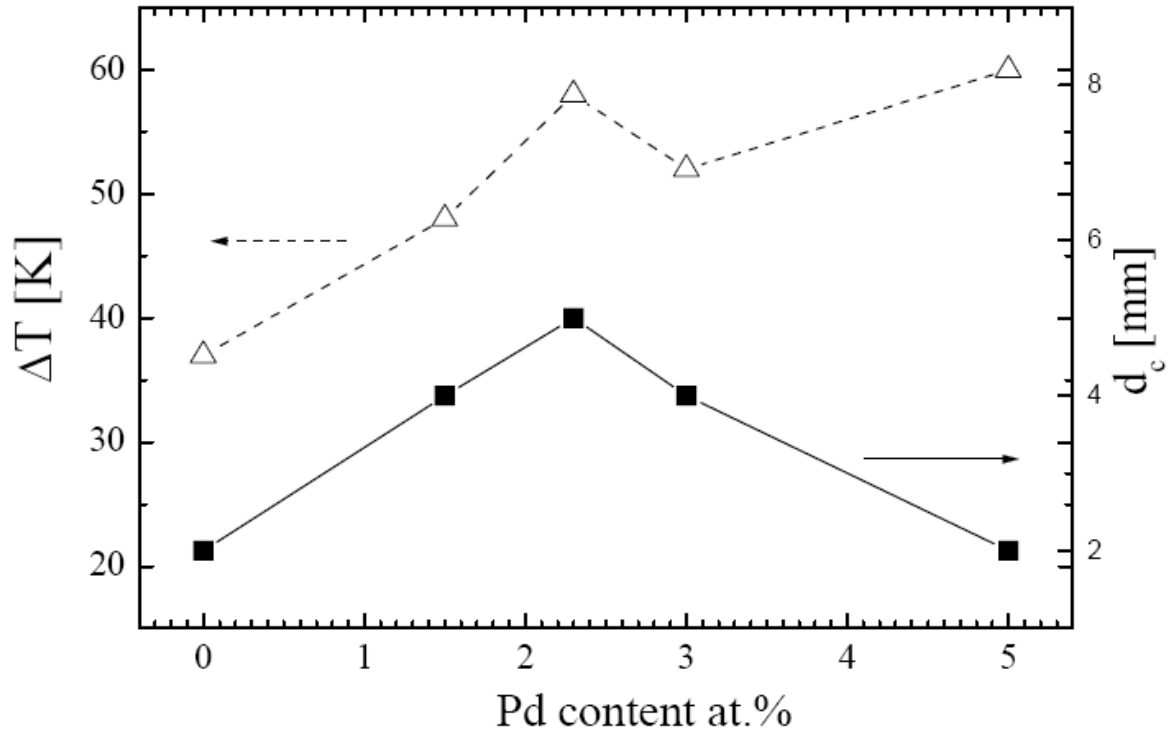


Figure 2.18 Position dependence of ΔT and d_c for $(\text{Au}_{60.1}\text{Ag}_{6.8}\text{Cu}_{33.1})_{83.7-y}\text{Pd}_y\text{Si}_{16.3}$ for $y = 0-5\%$. A strong dependence on the Pd content of both d_c and ΔT is observed. No obvious correlation of d_c and ΔT is seen [9].

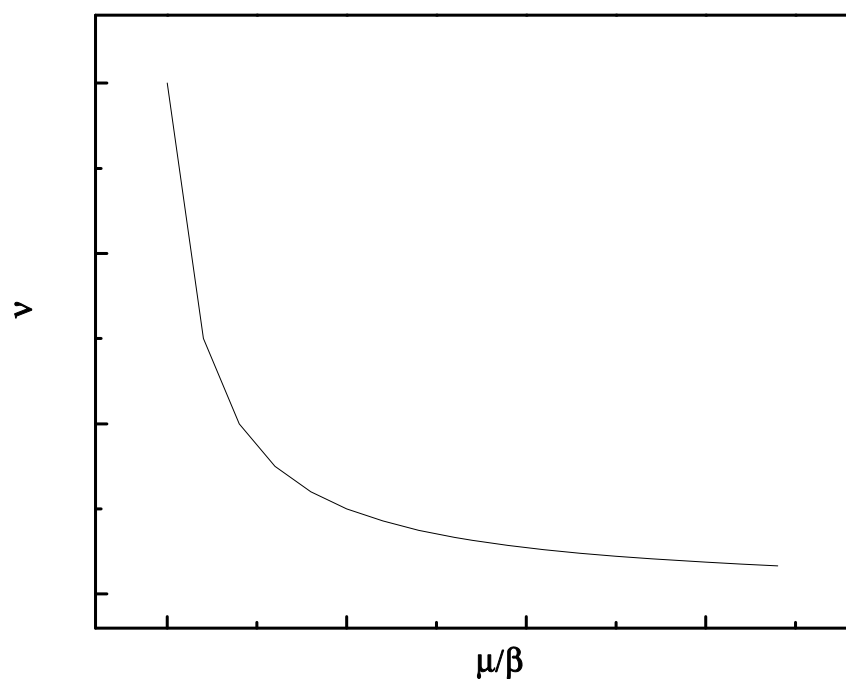
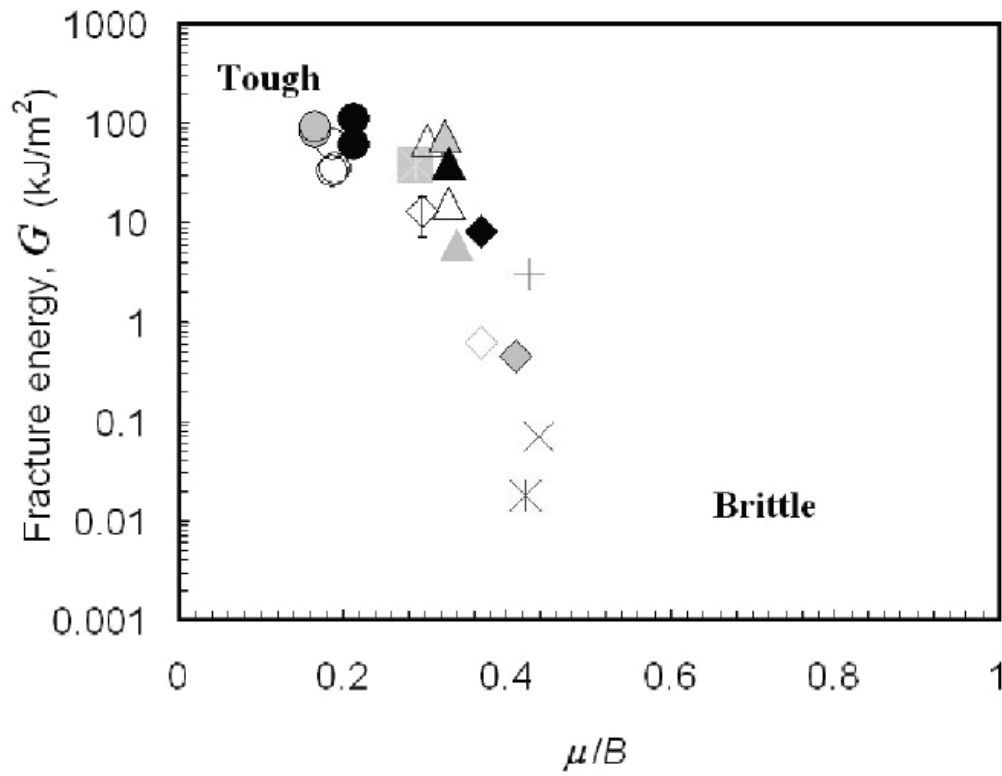


Figure 2.19 The relationship between ν and μ/β .



\times Mg ₆₅ Cu ₂₅ Tb ₁₀	$+$ Ce ₇₀ Al ₁₀ Ni ₁₀ Cu ₁₀	\times Fe ₅₀ Mn ₁₀ Mo ₁₄ Cr ₄ C ₁₆ B ₆
Δ Zr ₅₇ Ti ₅ Cu ₂₀ Ni ₈ Al ₁₀	Δ Zr ₄₁ Ti ₁₄ Cu _{12.5} Ni ₁₀ Be _{22.5}	\diamond Zr ₅₇ Nb ₅ Cu _{15.4} Ni _{12.6} Al ₁₀
\blacksquare Cu ₆₀ Zr ₂₀ Hf ₁₀ Ti ₁₀	\bullet Fe ₈₀ P ₁₃ C ₇	\circ Pd _{77.5} Cu ₆ Si _{16.5}
		\odot Pt _{57.5} Cu _{14.7} Ni _{5.3} P _{22.5}

Figure 2.20 The correlation of fracture energy G with elastic modulus ratio μ/B for all the as-cast (unannealed) metallic glasses for which relevant data are available (all compositions in at.%). Elastic constants were used to convert fracture toughness to fracture energy [79].

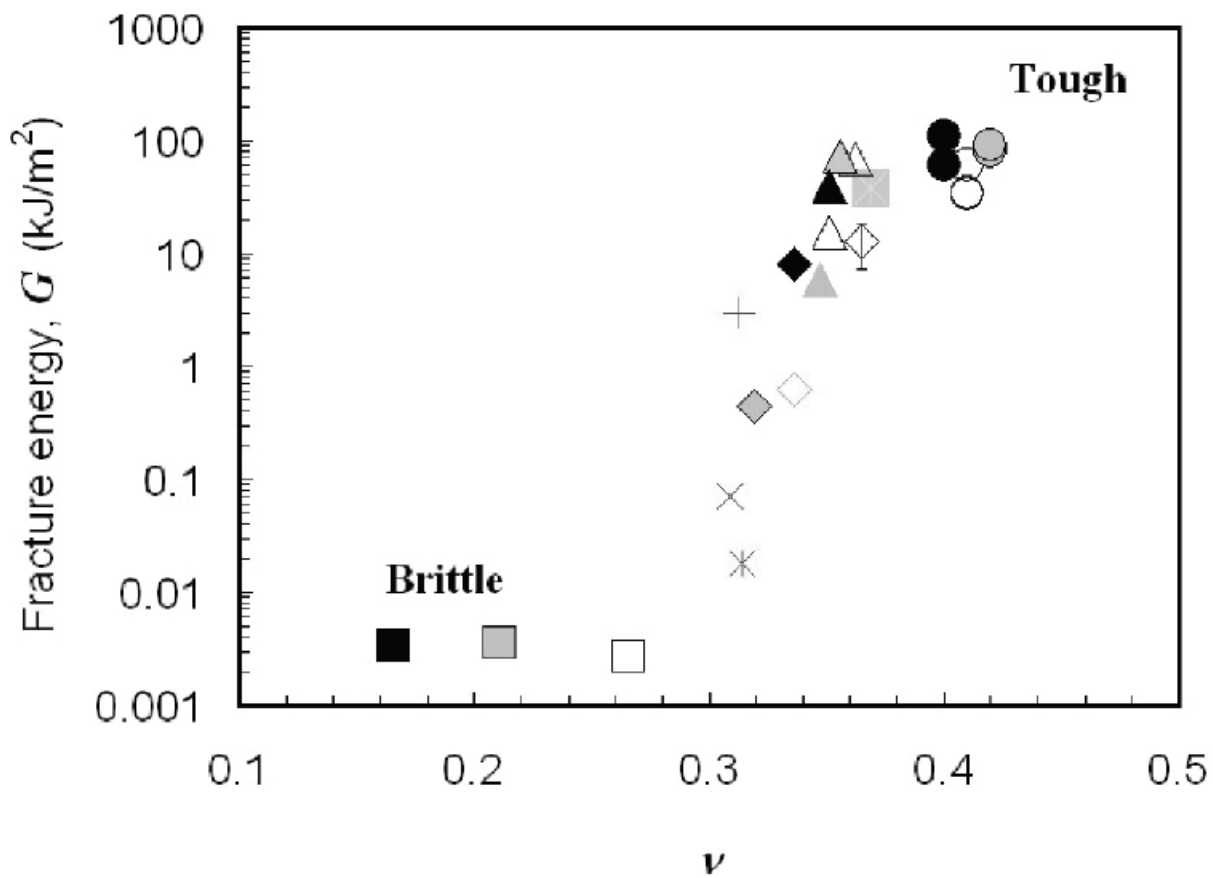


Figure 2.21 The correlation of fracture energy G with Poisson's ratio for all the data collected on metallic glasses (as-cast and annealed) as well as for oxide glasses [79].

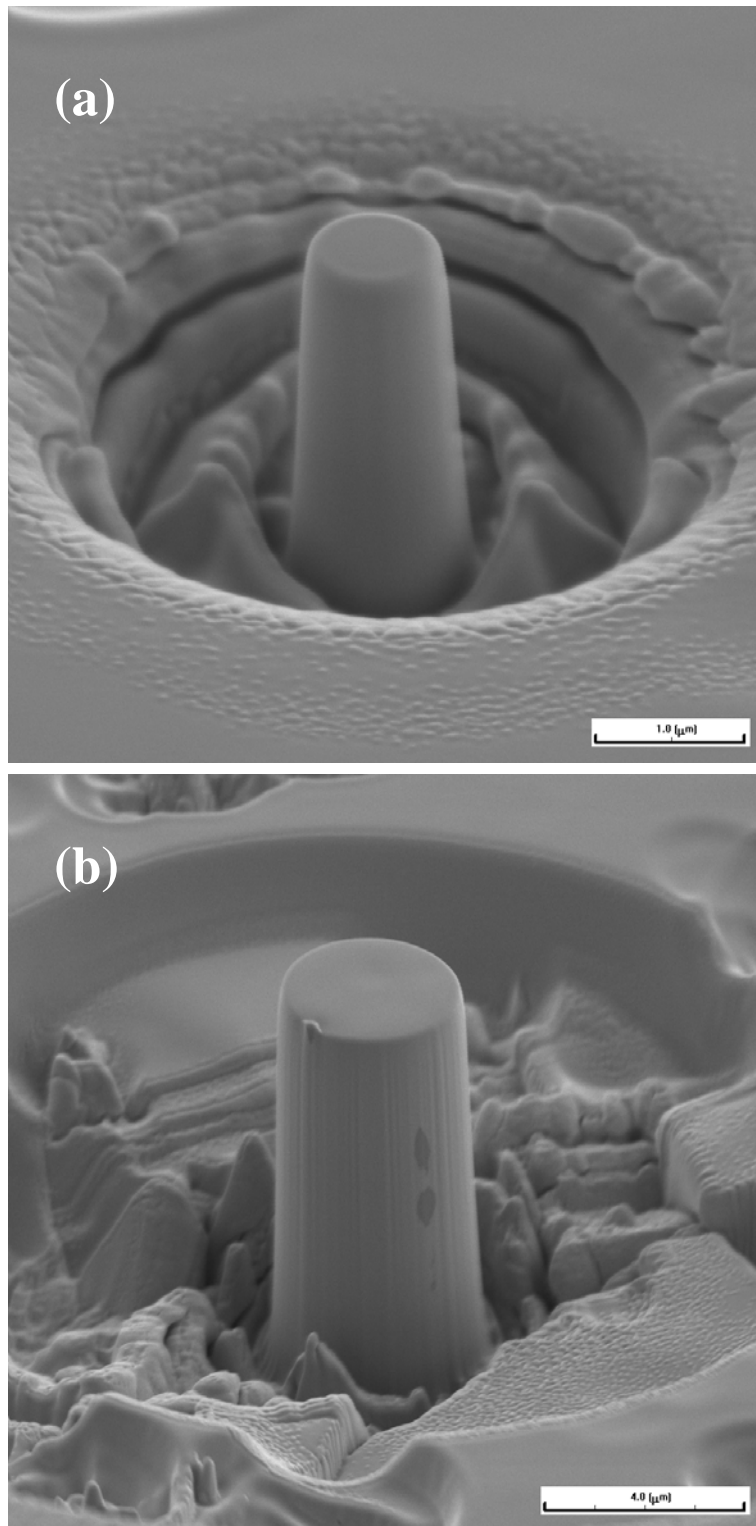


Figure 3.1 Au-BMG micropillars fabricated by focus ion beam technique: (a) 1 μm in diameter and (b) 3.8 μm in diameter.

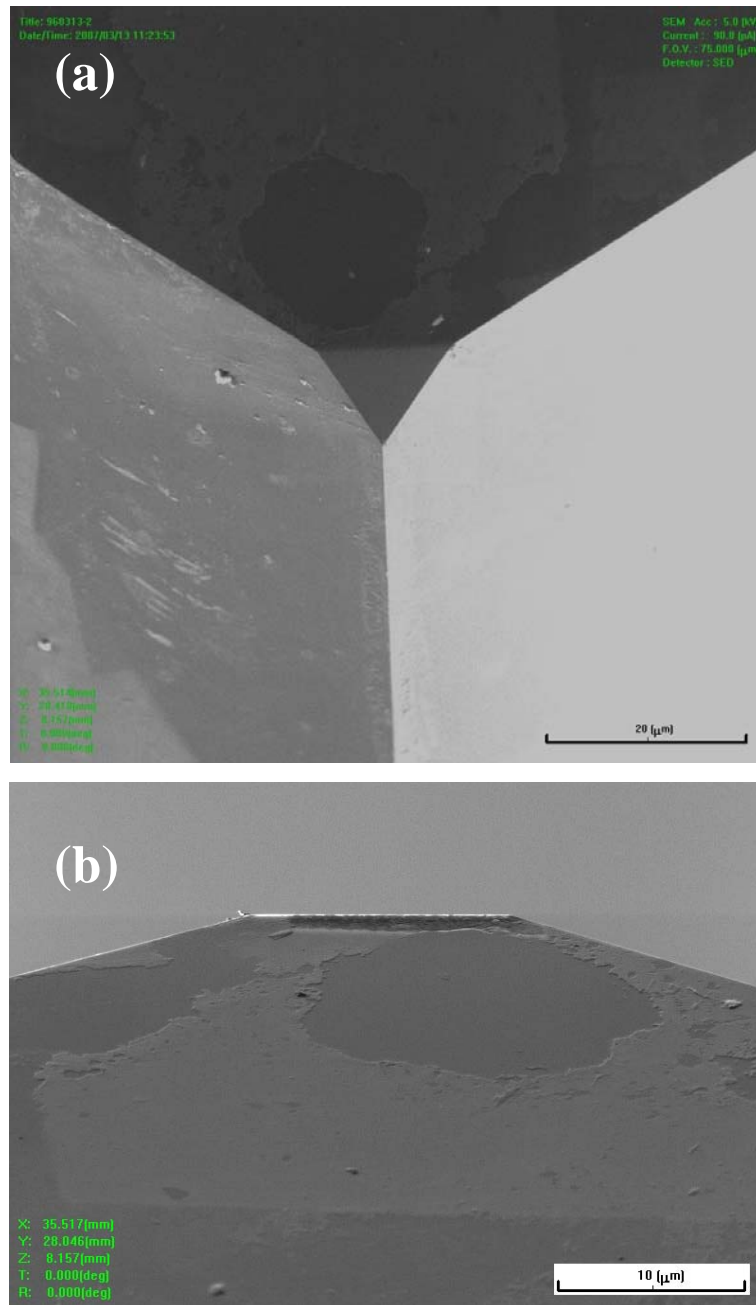


Figure 3.2 FIB-SEM micrographs of the flat-punch tip: a) top view and (b) side view.

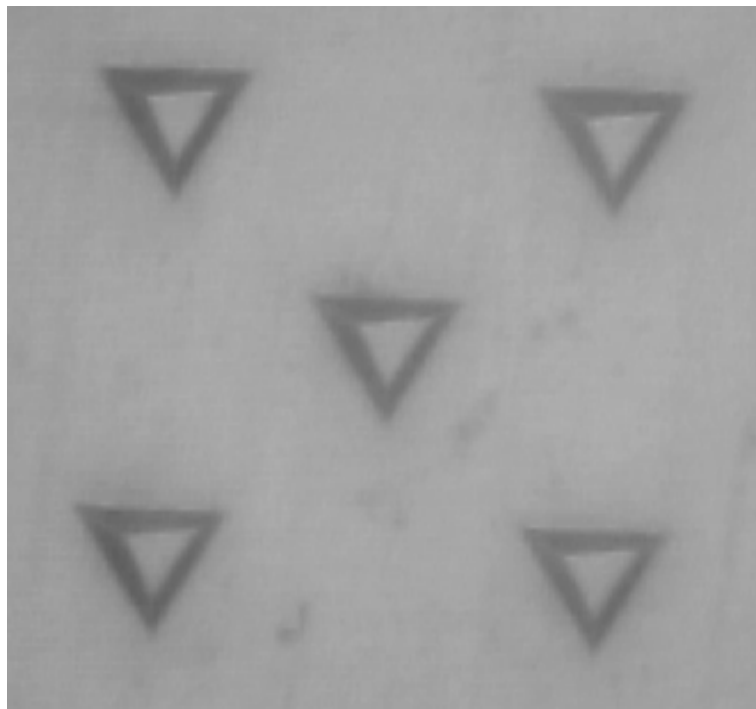


Figure 3.3 Triangle marks made by flat punch .

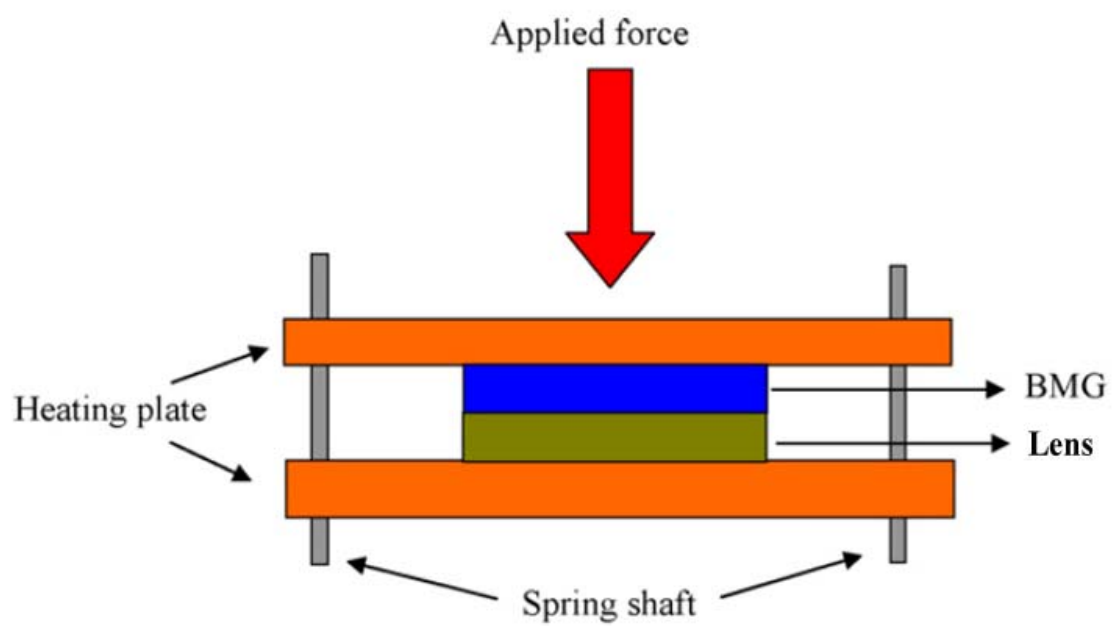


Figure 3.4 Hot embossing set-up for oil hydraulic system [92].

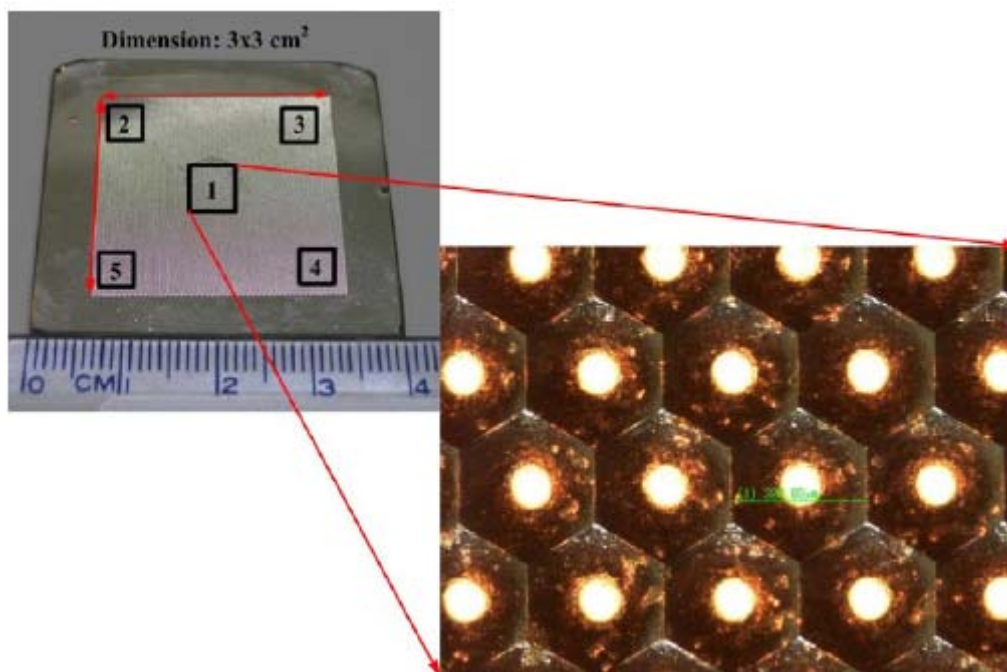


Figure 3.5 Ni-Co mold with gapless hexagonal micro-lens array. [92]

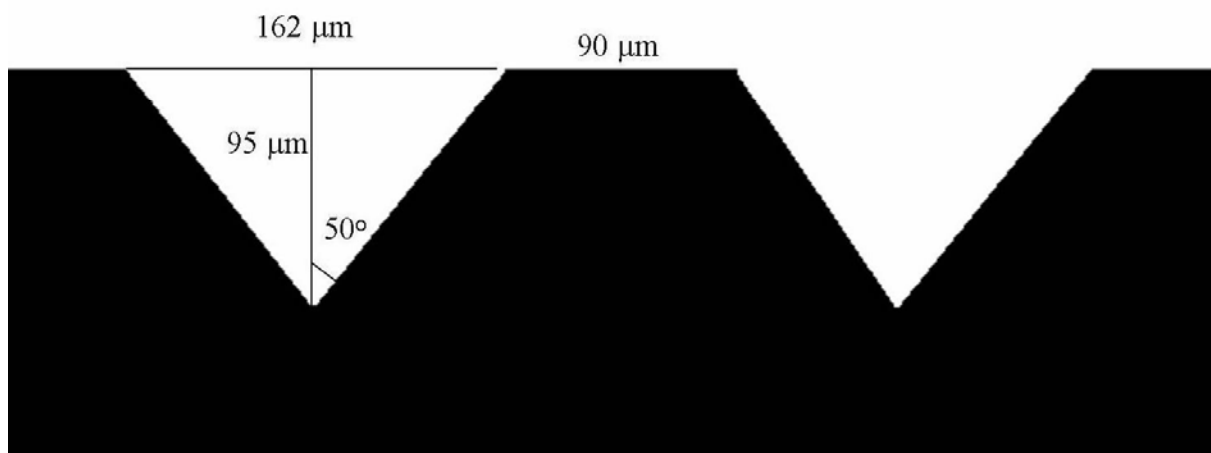


Figure 3.6 Profile of V-groove mold.



Figure 4.1 The appearance of the Au-based BMG rods with 2 and 3 mm.

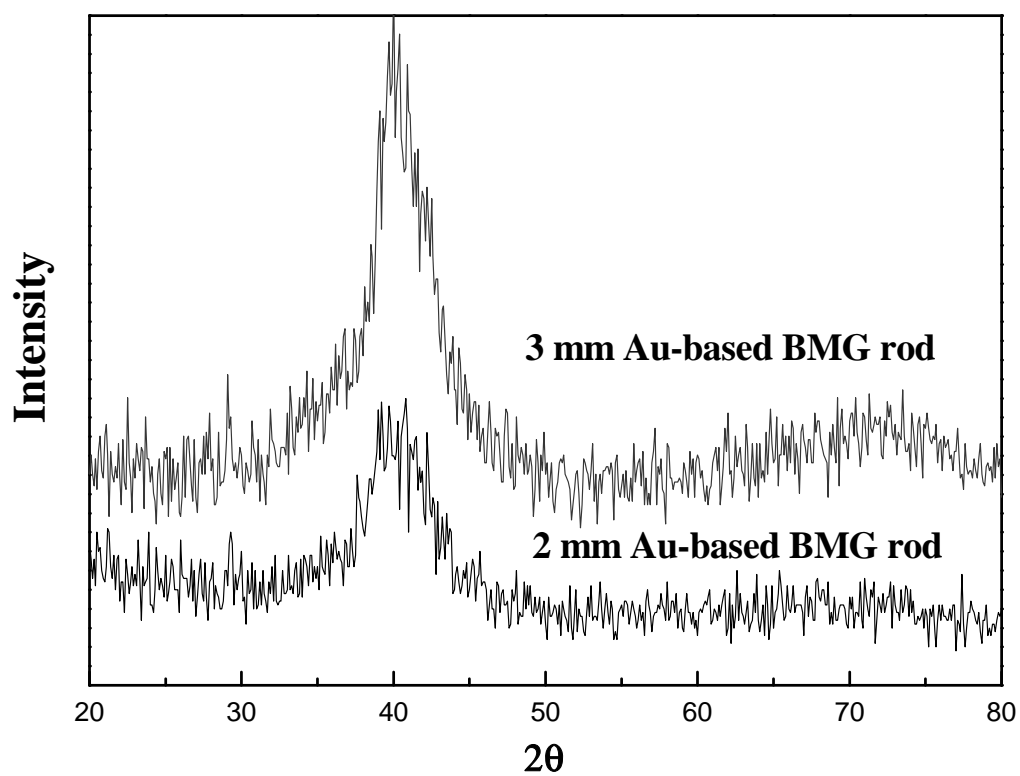


Figure 4.2 XRD pattern of the 3 mm and 2 mm Au-based amorphous alloys.

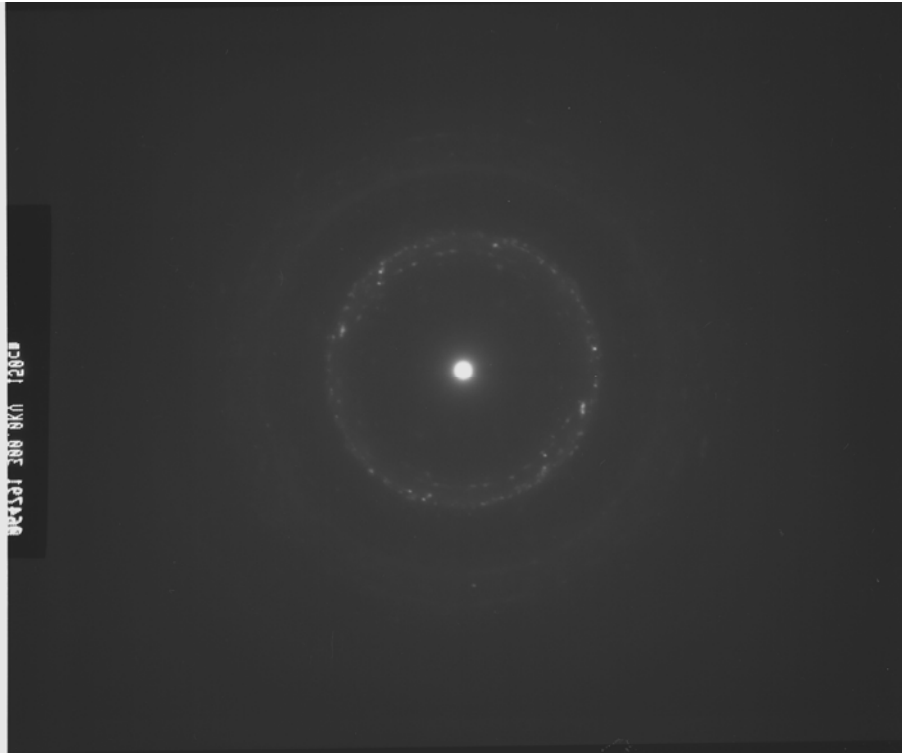


Figure 4.3 TEM diffraction pattern of the 3 mm diameter Au-based BMG.

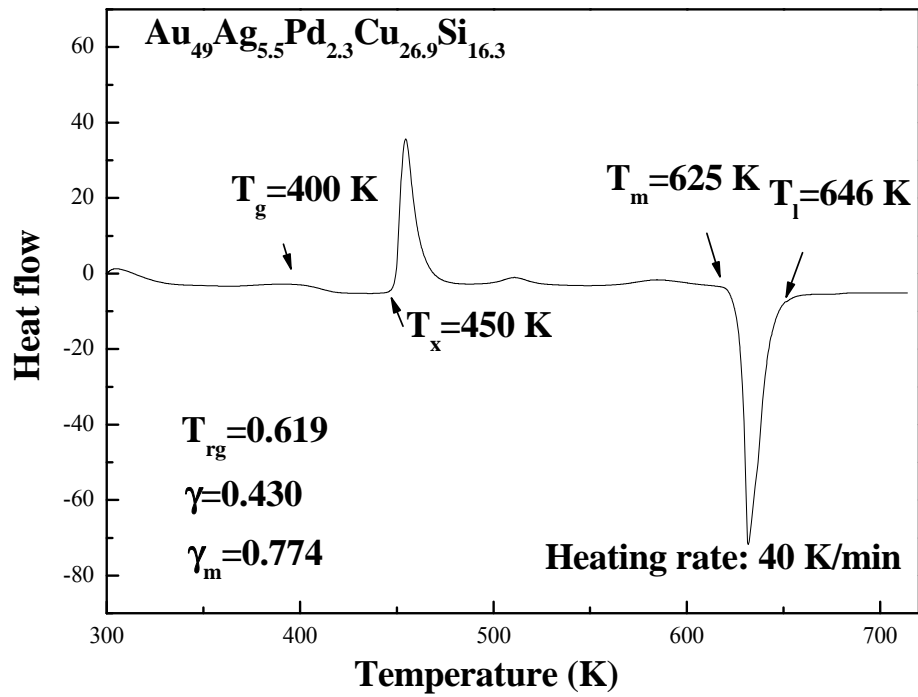


Figure 4.4 DSC plot of Au-based amorphous alloy with the heating rate of 40 K/ min.

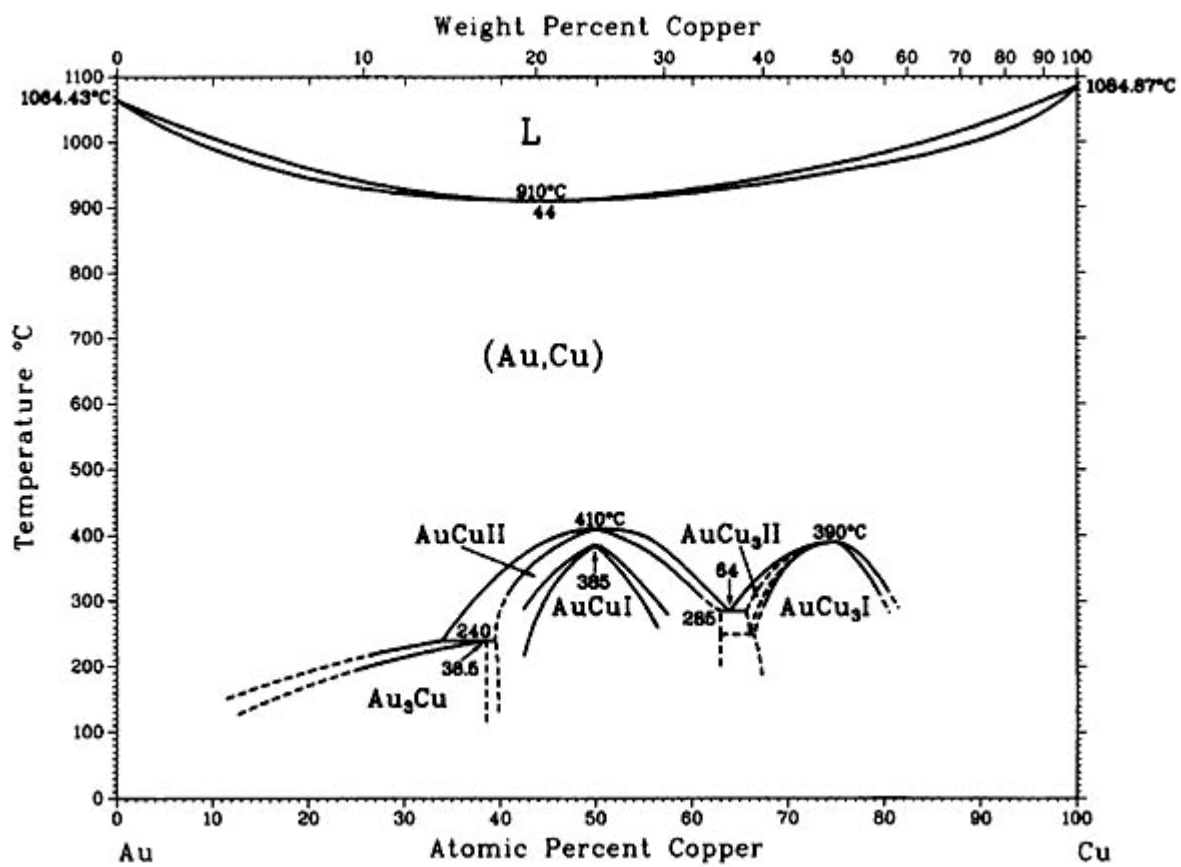


Figure 4.5 The Au-Cu binary phase diagram.

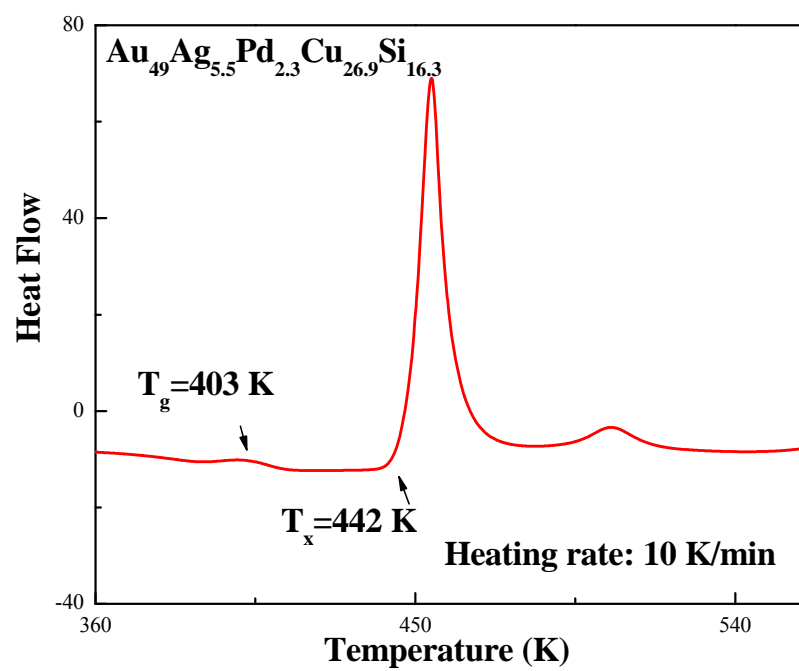


Figure 4.6 DSC plot of Au-based amorphous alloy with the heating rate of 10 K/min.

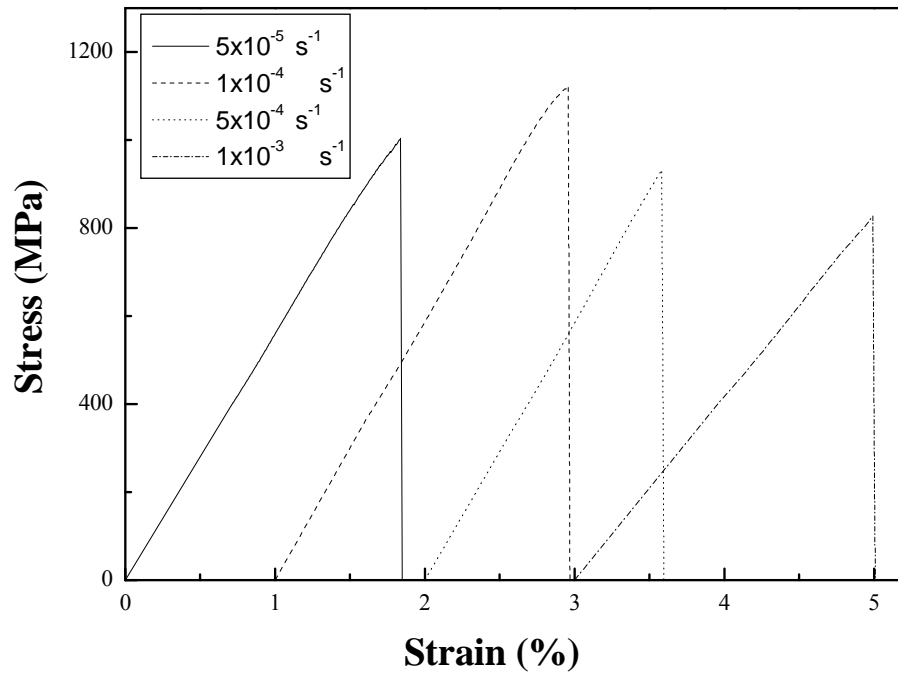


Figure 4.7 The compressive stress-strain curves for the $\text{Au}_{49}\text{Ag}_{5.5}\text{Pd}_{2.3}\text{Cu}_{26.9}\text{Si}_{16.3}$ BMG.

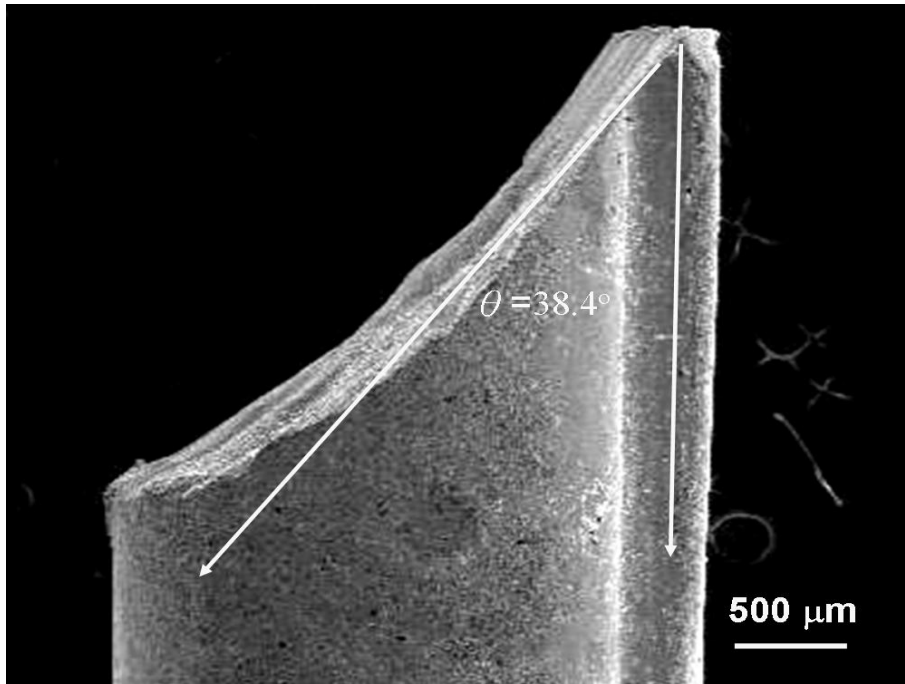


Figure 4.8 The outer appearance showing fracture plan inclination of the Au-based BMG with a strain rate of $5 \times 10^{-5} \text{ s}^{-1}$.

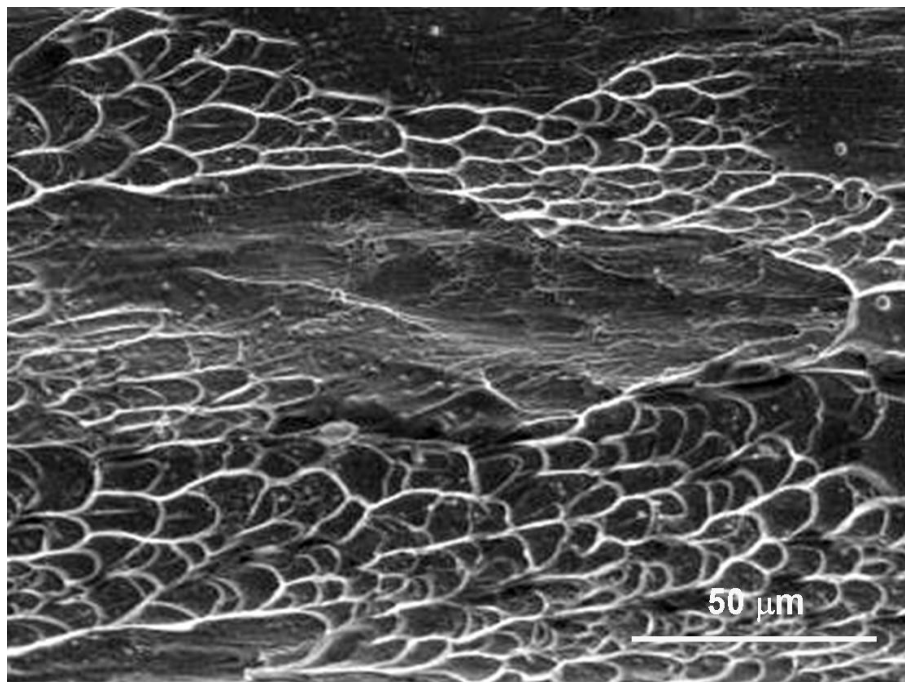


Figure 4.9 The fracture surface morphology of the Au-based BMG with a strain rate of $5 \times 10^{-5} \text{ s}^{-1}$.

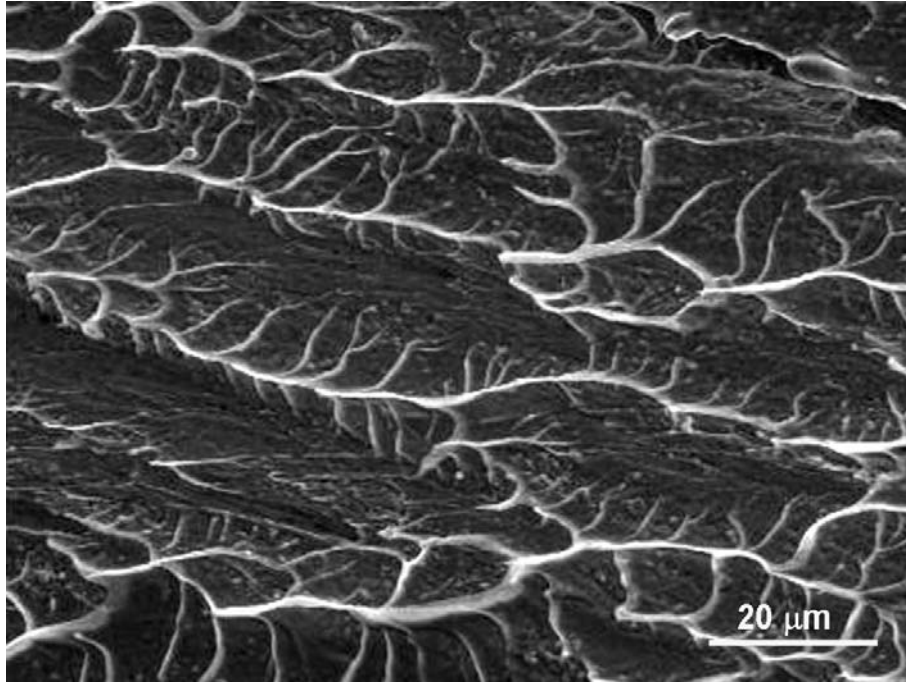


Figure 4.10 The fracture surface morphology of the Au-based BMG with a strain rate of $5 \times 10^{-5} \text{ s}^{-1}$.

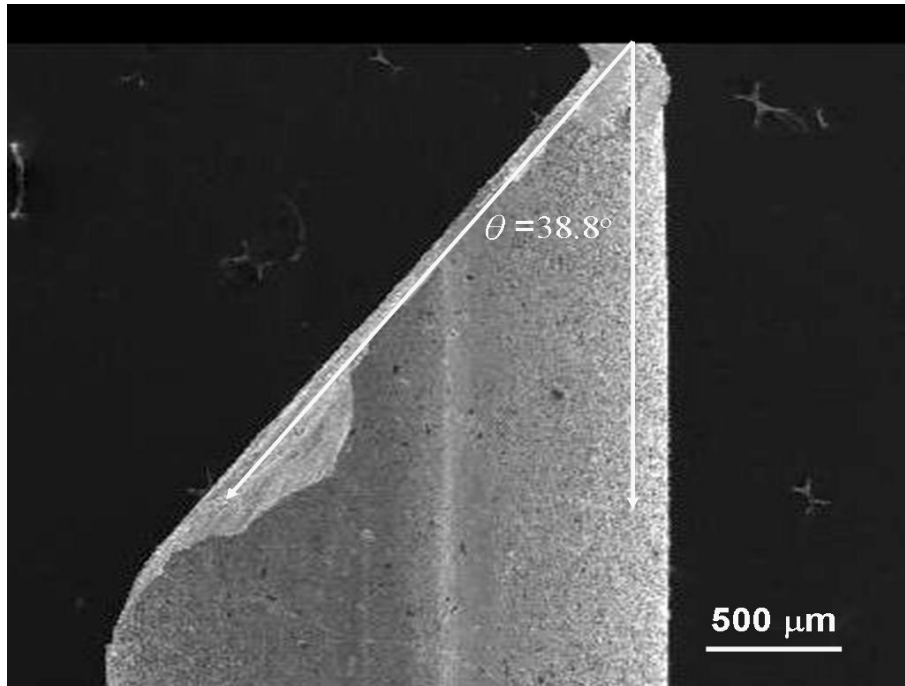


Figure 4.11 The outer appearance showing fracture plan inclination of the Au-based BMG with a strain rate of $1 \times 10^{-4} \text{ s}^{-1}$.

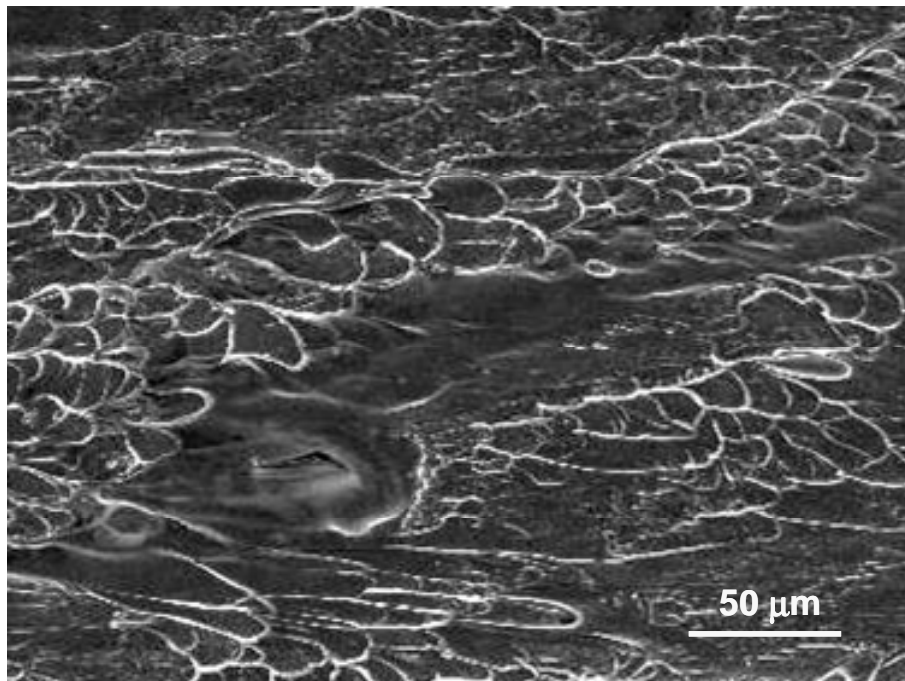


Figure 4.12 The fracture surface morphology of the Au-based BMG with a strain rate of $1 \times 10^{-4} \text{ s}^{-1}$.

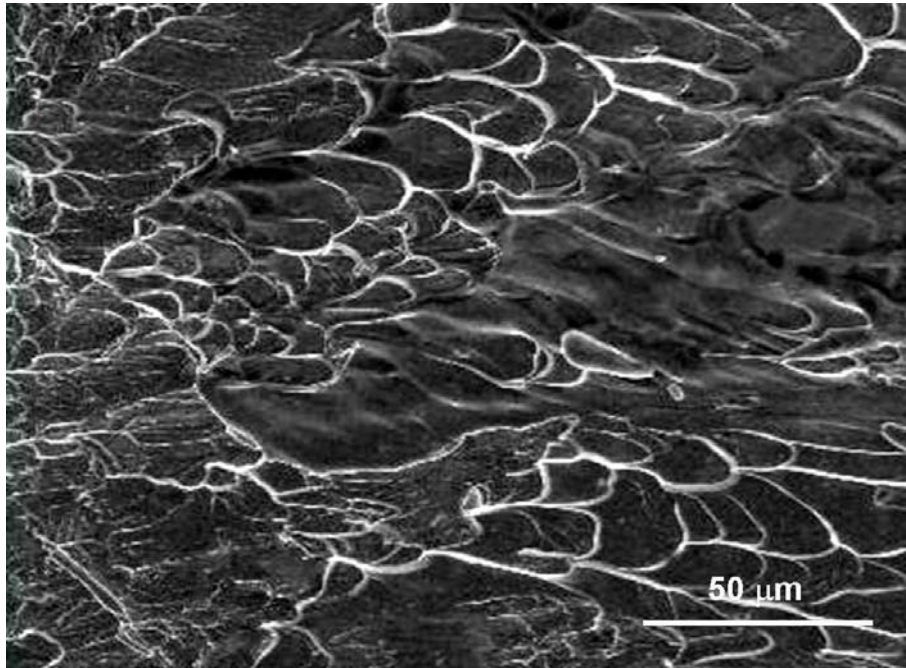


Figure 4.13 The fracture surface morphology of the Au-based BMG with a strain rate of $1 \times 10^{-4} \text{ s}^{-1}$.

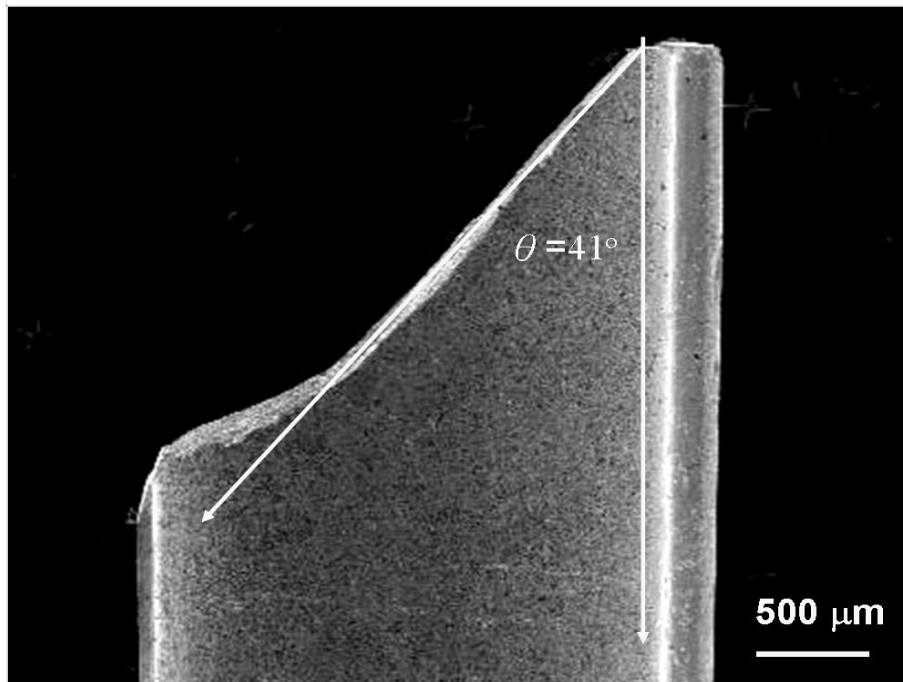


Figure 4.14 The outer appearance showing fracture plan inclination of the Au-based BMG with a strain rate of $5 \times 10^{-4} \text{ s}^{-1}$.

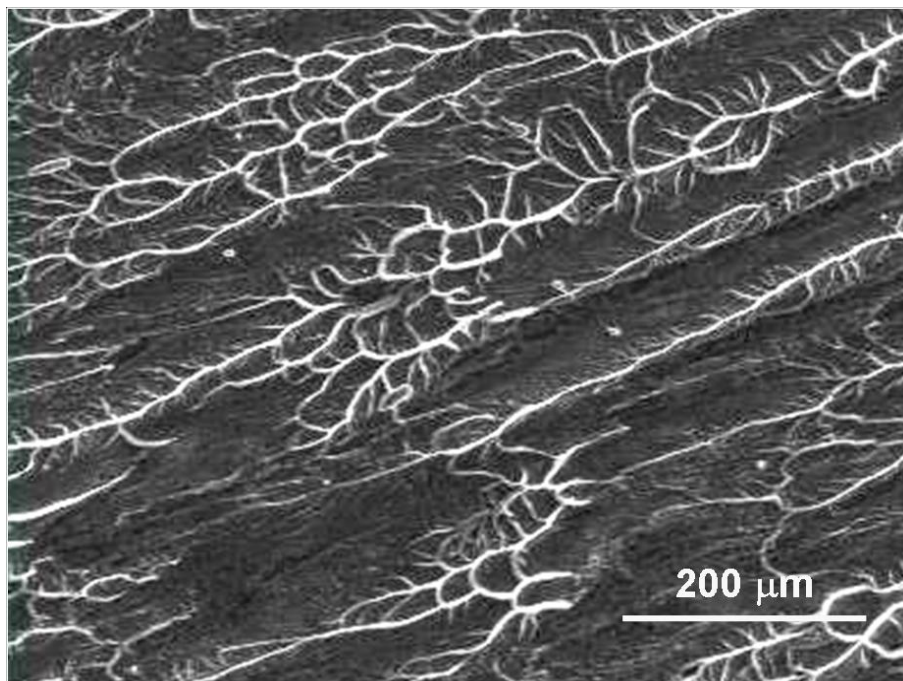


Figure 4.15 The fracture surface morphology of the Au-based BMG with a strain rate of $5 \times 10^{-4} \text{ s}^{-1}$.

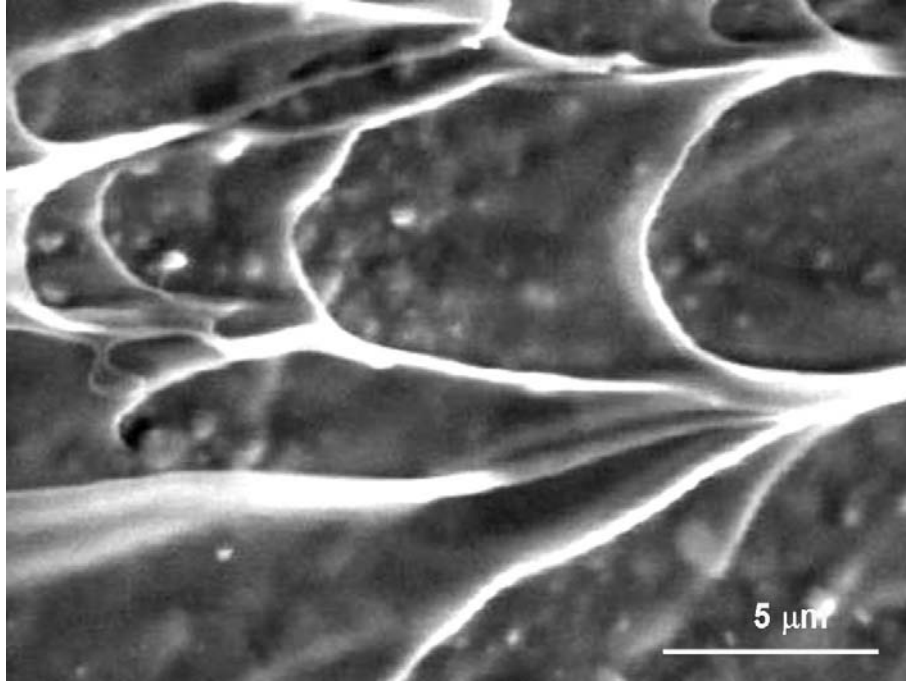


Figure 4.16 The fracture surface morphology of the Au-based BMG with a strain rate of $5 \times 10^{-4} \text{ s}^{-1}$.

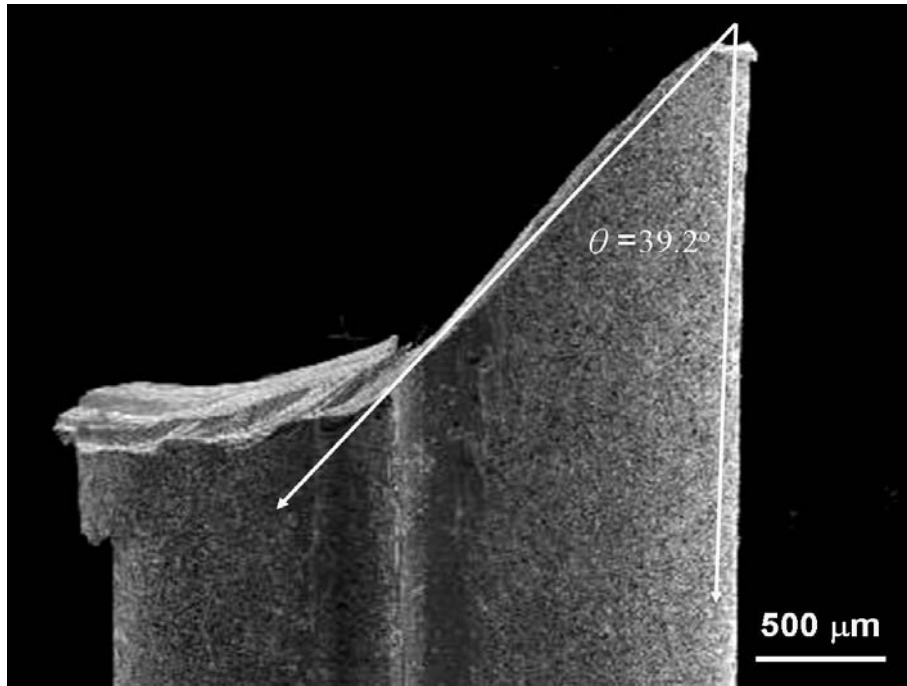


Figure 4.17 The outer appearance showing fracture plan inclination of the Au-based BMG with a strain rate of $1 \times 10^{-3} \text{ s}^{-1}$.

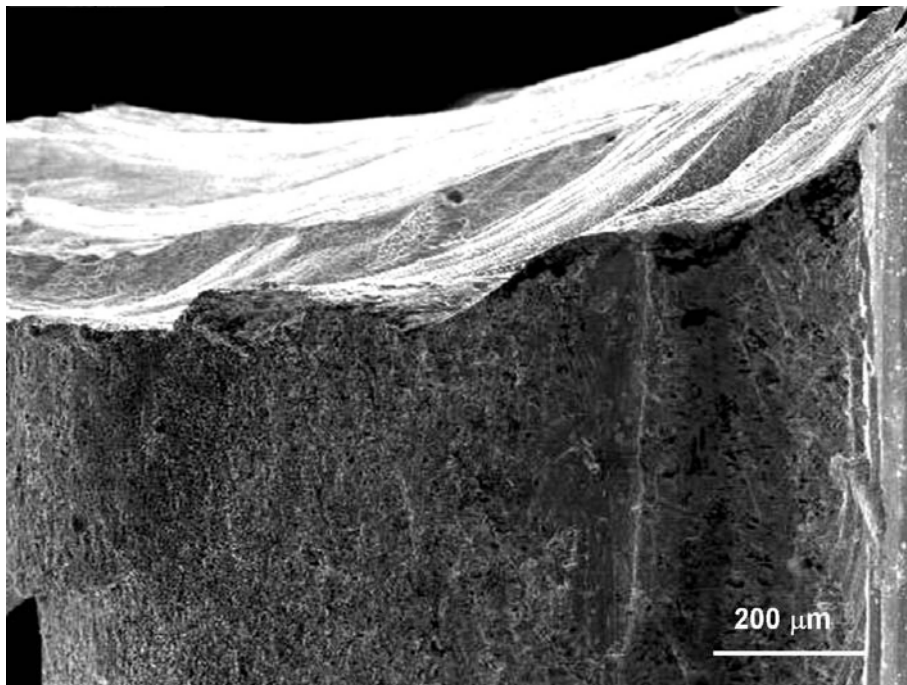


Figure 4.18 The outer appearance showing fracture plan of the Au-based BMG with strain a rate of $1 \times 10^{-3} \text{ s}^{-1}$.

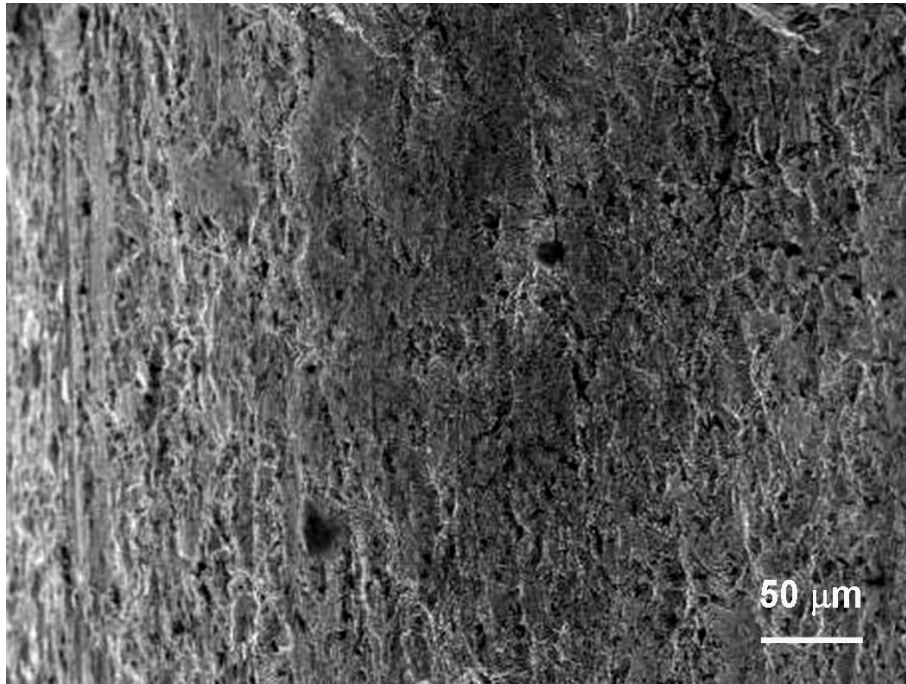


Figure 4.19 The outer appearance of the Au-based BMG with a strain rate of $1 \times 10^{-3} \text{ s}^{-1}$.

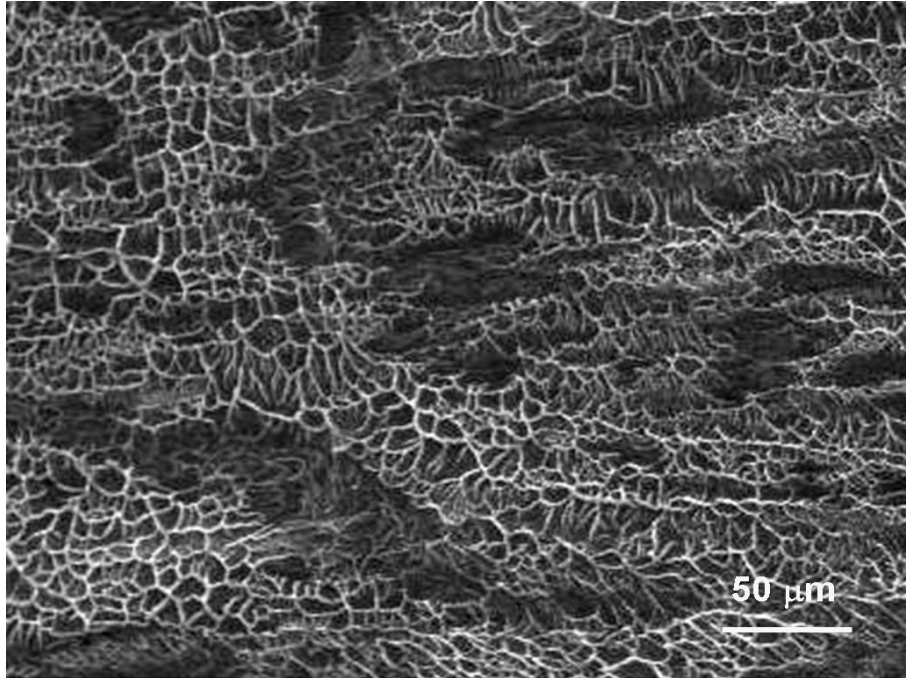


Figure 4.20 The fracture surface morphology of the Au-based BMG with a strain rate of $1 \times 10^{-3} \text{ s}^{-1}$.

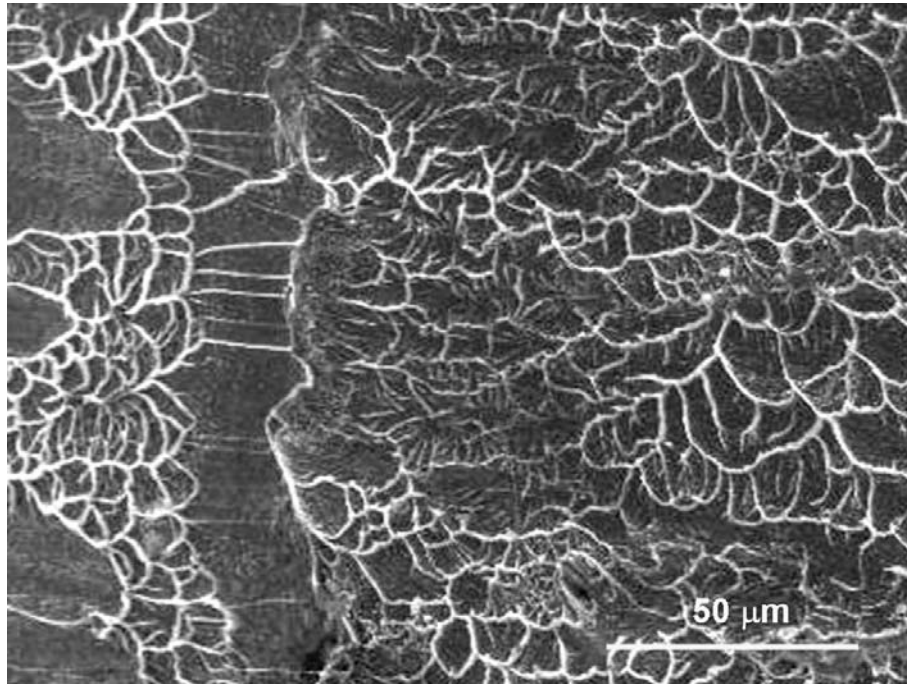


Figure 4.21 The fracture surface morphology of the Au-based BMG with a strain rate of $1 \times 10^{-3} \text{ s}^{-1}$.

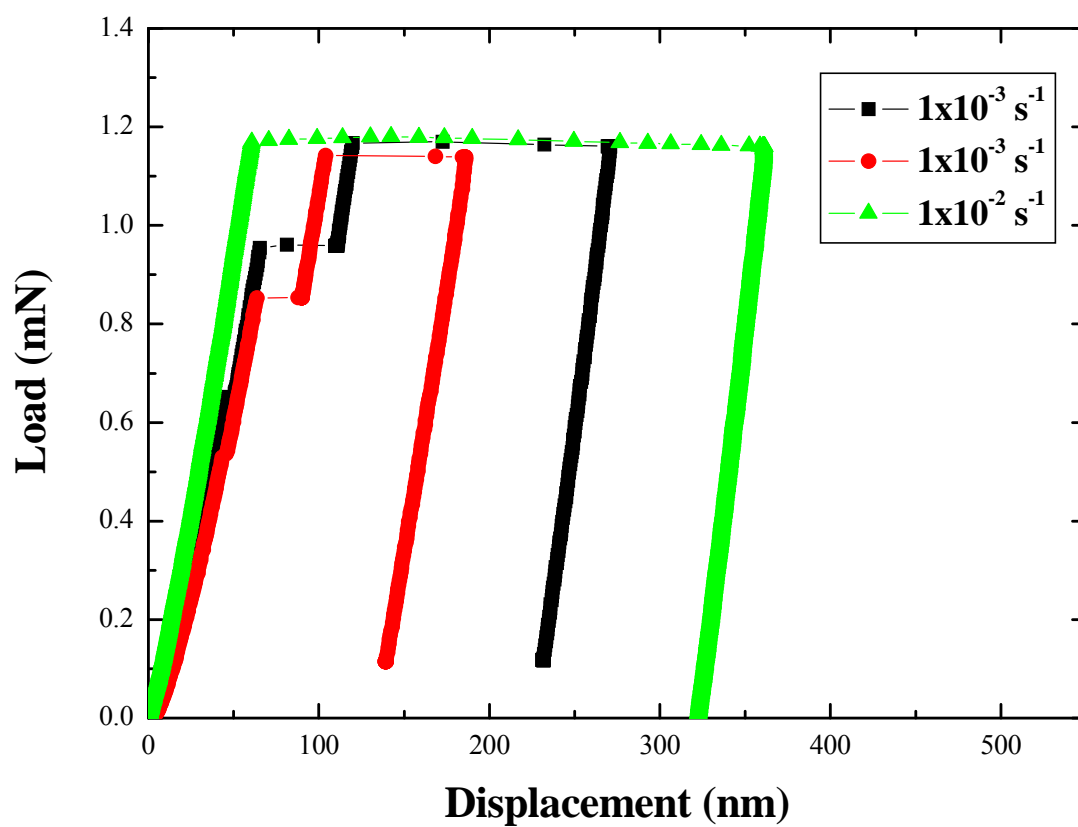


Figure 4.22 Compression load-displacement curves of the 1 μ m Au-BMG at different strain rates.

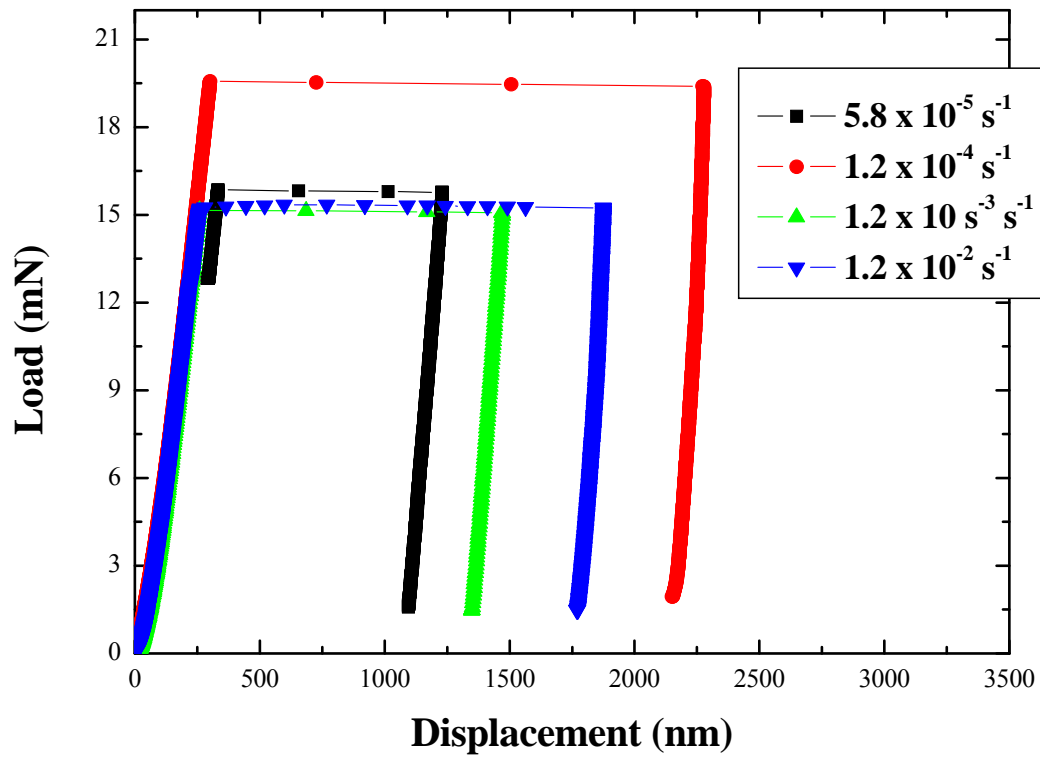


Figure 4.23 Compression load-displacement curves of the 3.8 μm Au-BMG at different strain rates.

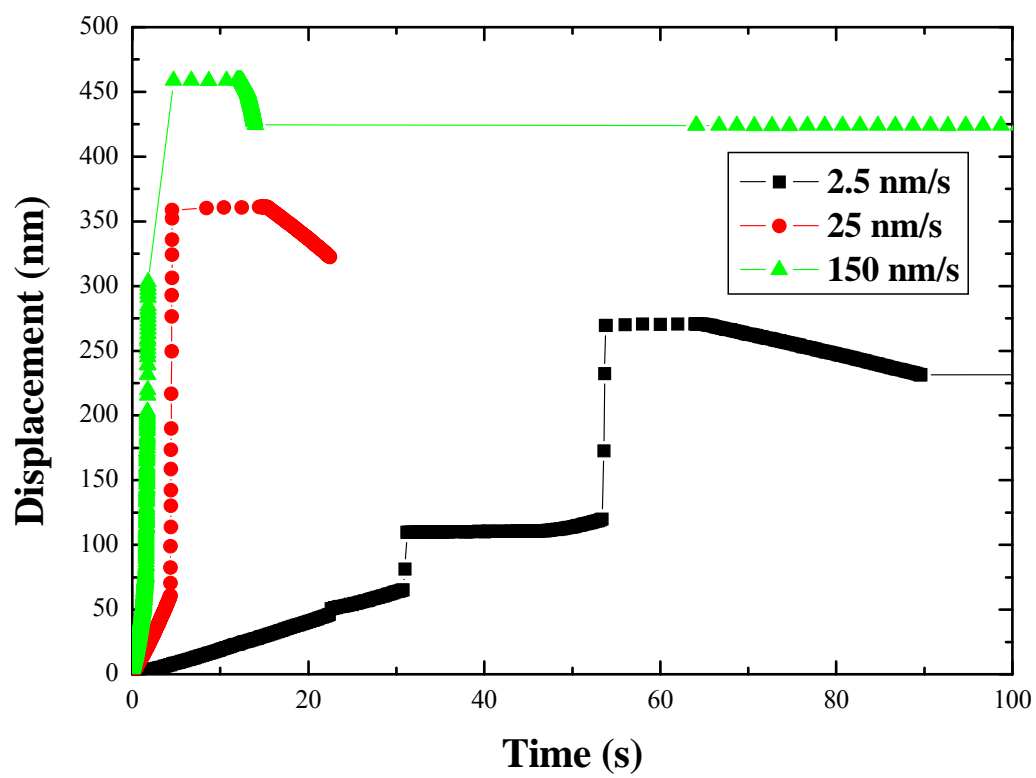


Figure 4.24 Time-and-displacement curves for the 1 μm Au BMG pillars.

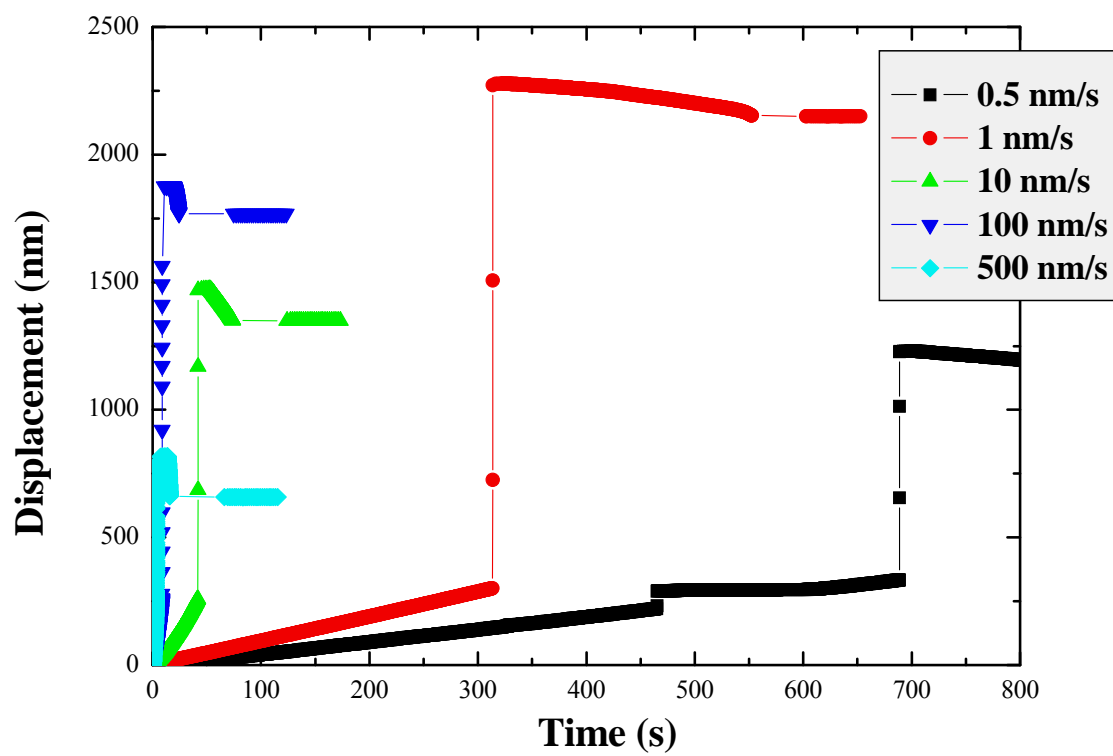


Figure 4.25 Time-and-displacement curves for the 3.8 μm Au BMG pillars.

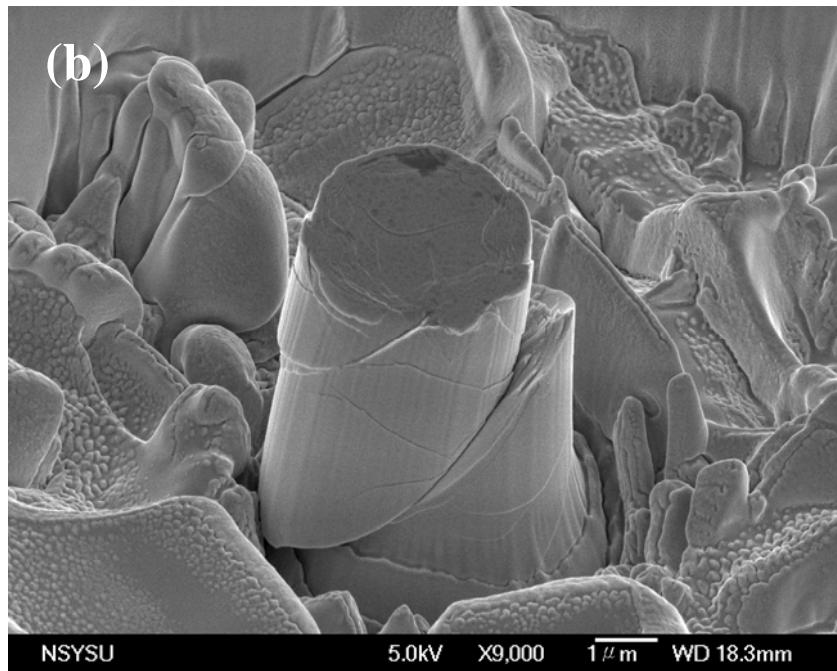
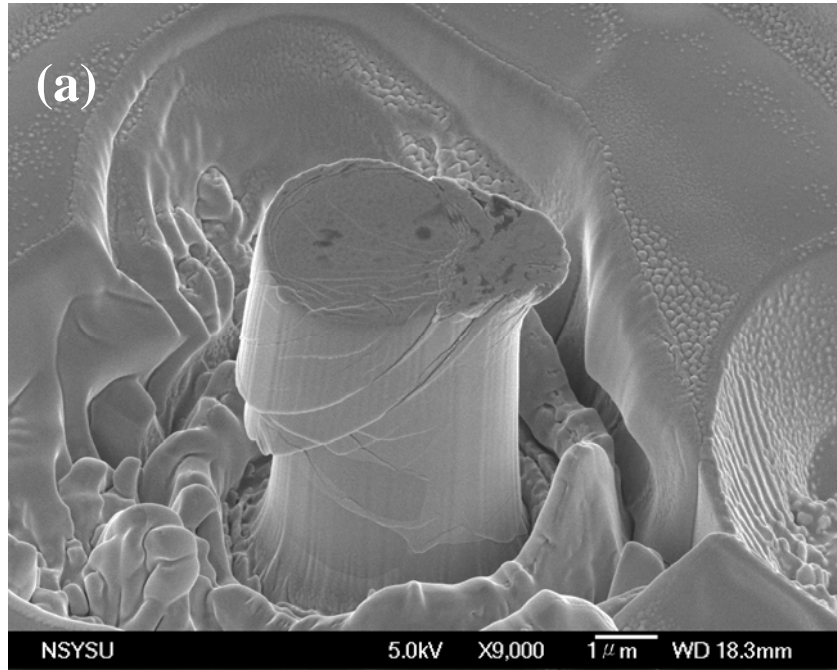
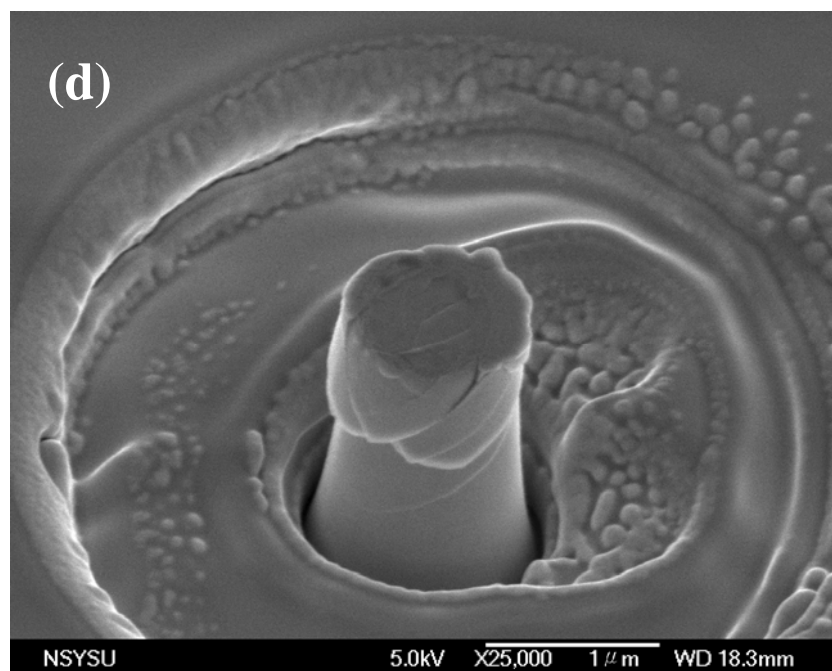
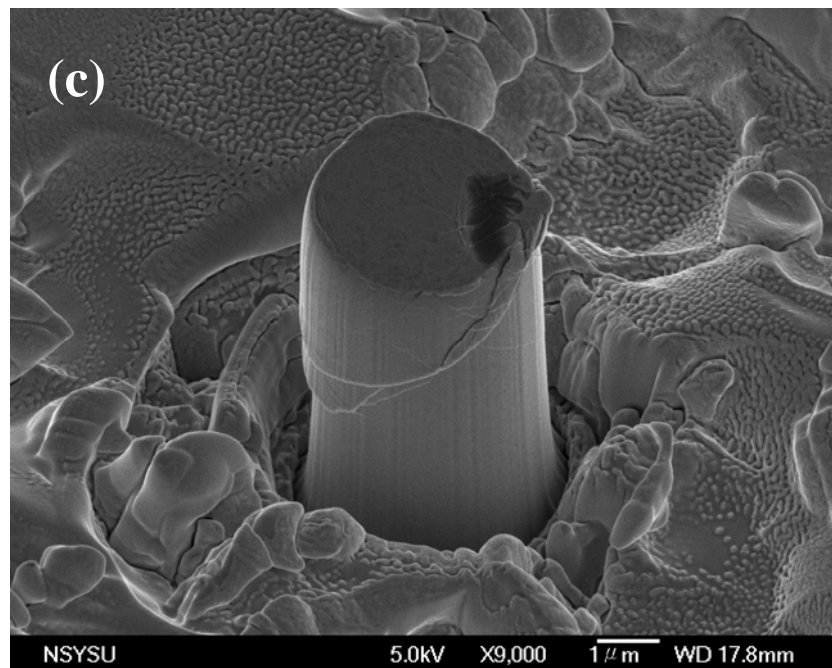
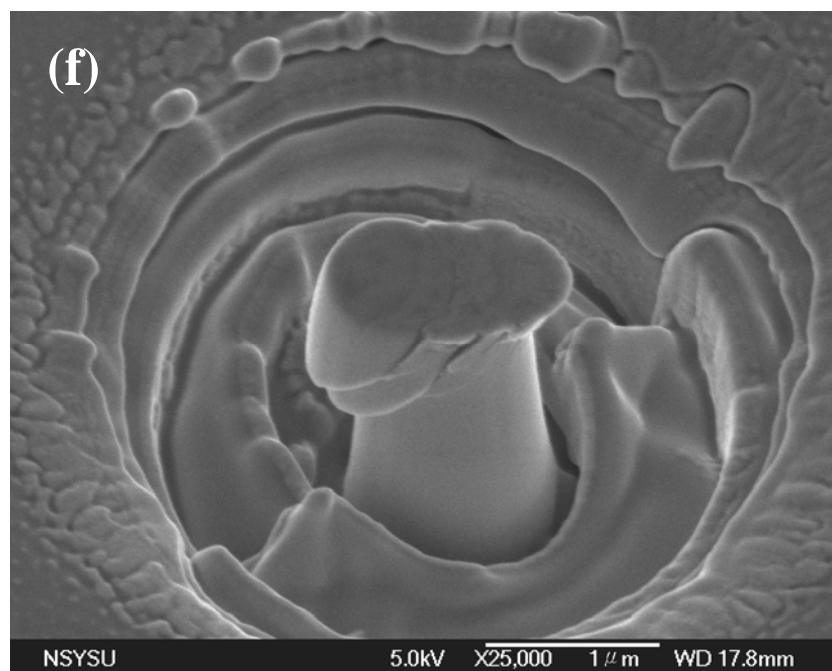
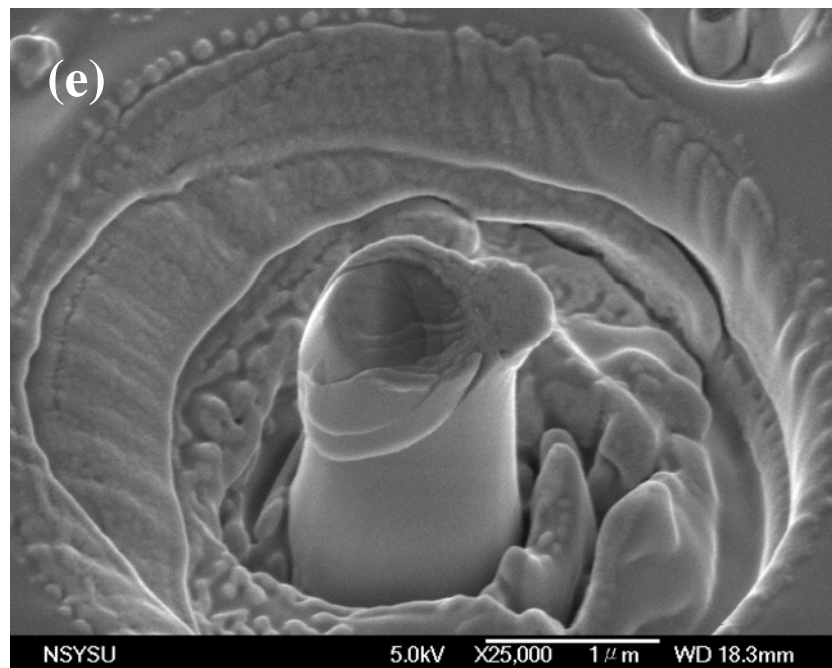


Figure 4.26 SEM micrographs showing the appearance of deformed pillars: (a) $3.8\ \mu\text{m}$, $\sim 1 \times 10^{-3}\ \text{s}^{-1}$, (b) $3.8\ \mu\text{m}$, $\sim 1 \times 10^{-2}\ \text{s}^{-1}$, (c) $3.8\ \mu\text{m}$, $\sim 6 \times 10^{-2}\ \text{s}^{-1}$, (d) $1\ \mu\text{m}$, $\sim 1 \times 10^{-3}\ \text{s}^{-1}$, (e) $1\ \mu\text{m}$, $\sim 1 \times 10^{-2}\ \text{s}^{-1}$, and (f) $1\ \mu\text{m}$, $\sim 6 \times 10^{-2}\ \text{s}^{-1}$.





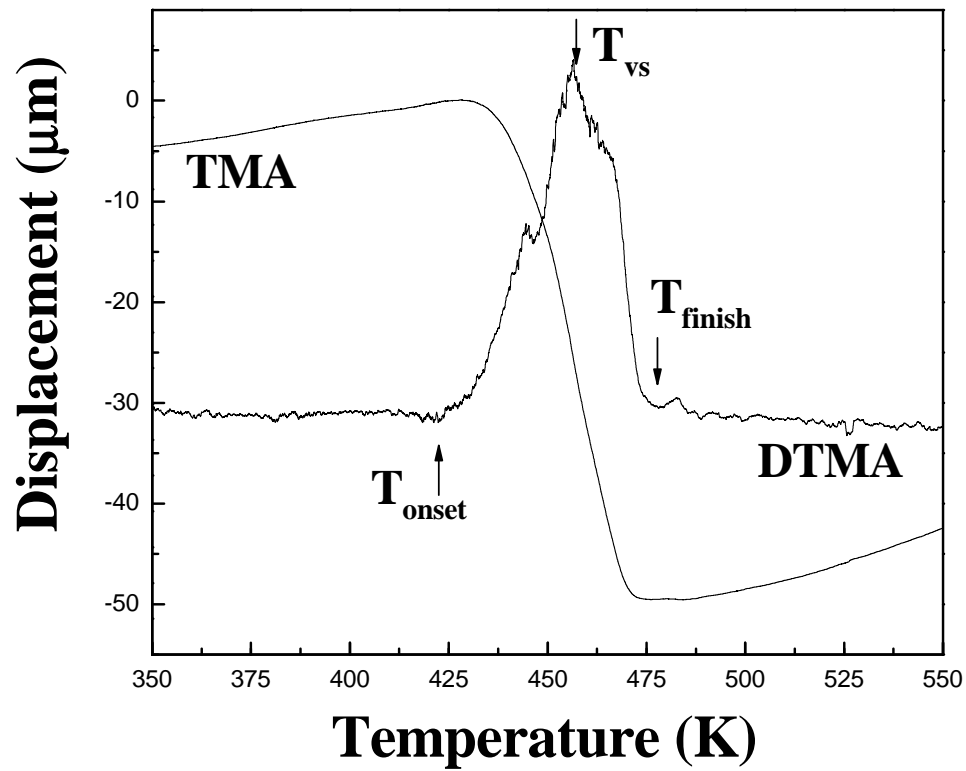


Figure 4.27 Typical TMA and DTMA curves measured at stress level of 7.1 kPa for the as-cast bulk Au-based BMG.

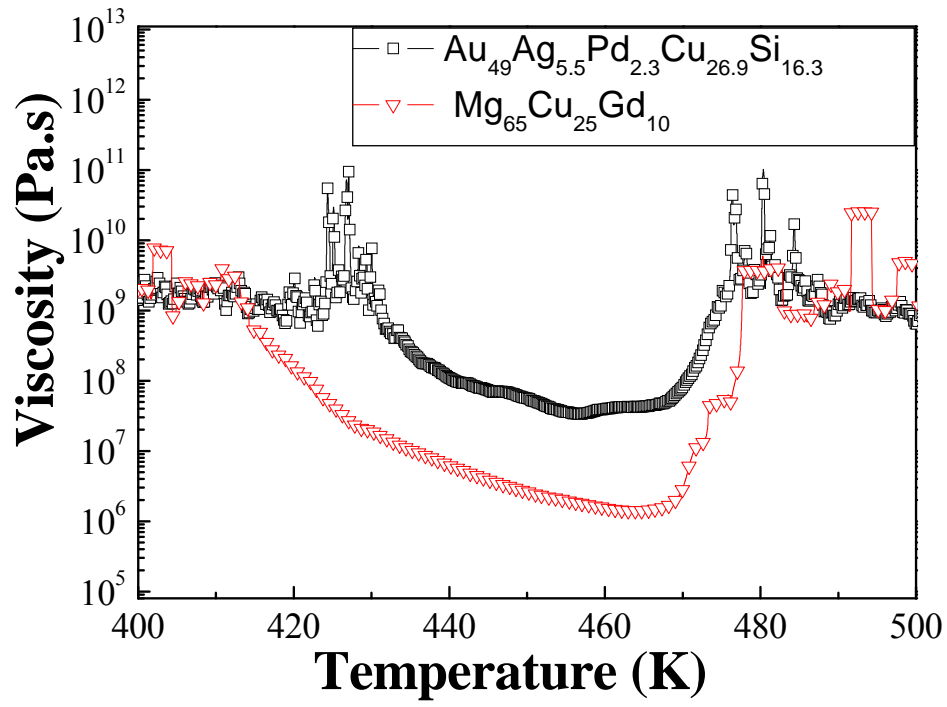


Figure 4.28 Measured viscosities of the Au-based and Mg-based BMG in the supercooled liquid region at a heating rate 10 K/min.

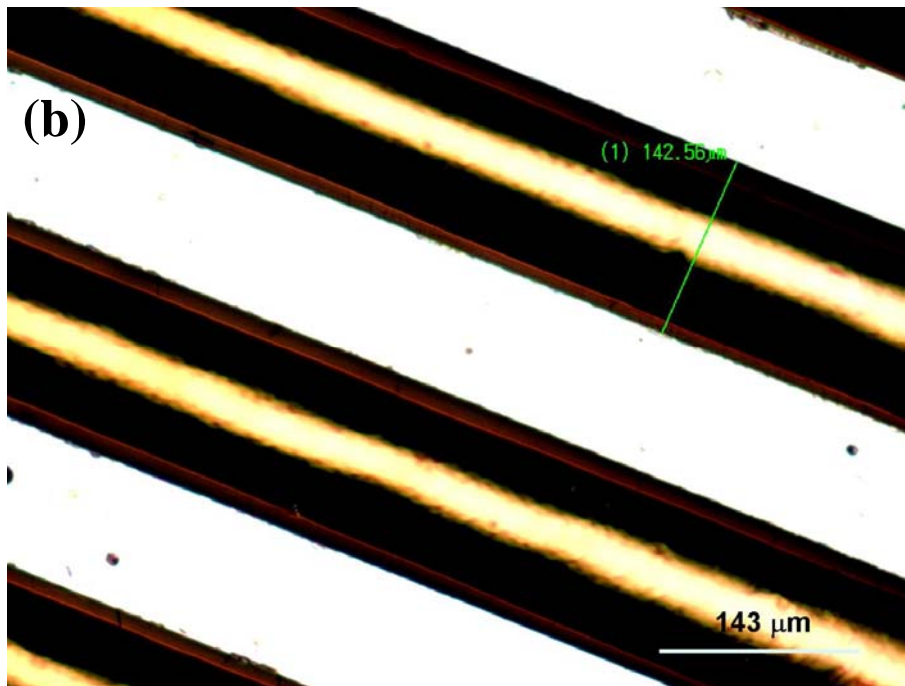
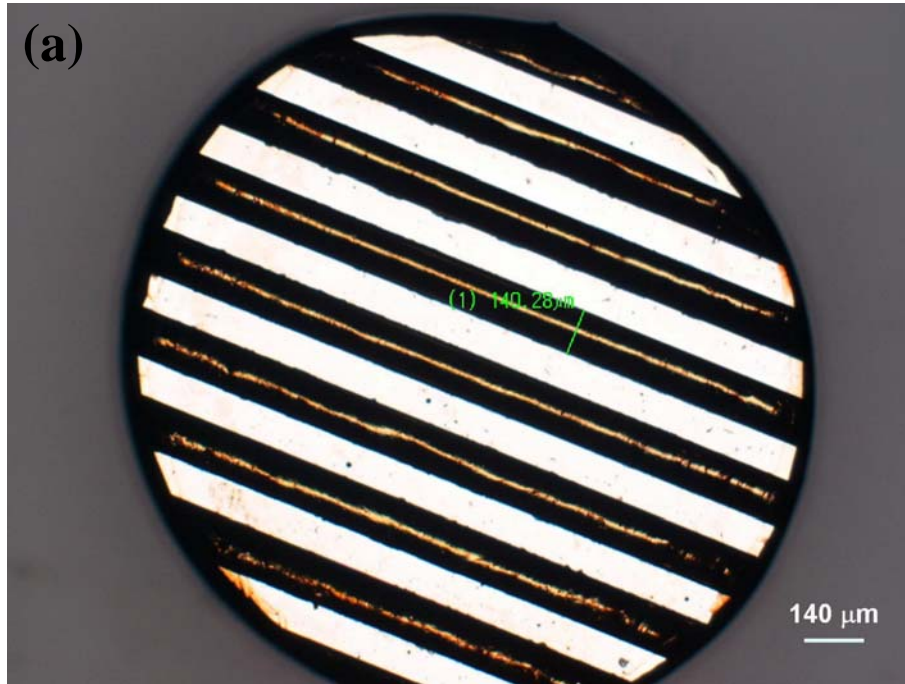


Figure 4.29 Replicated patterns by OM on the Au-based BMG materials imprinted at 177°C and 137 MPa for 1 min with (a) lower magnification by OM (b) higher magnification.

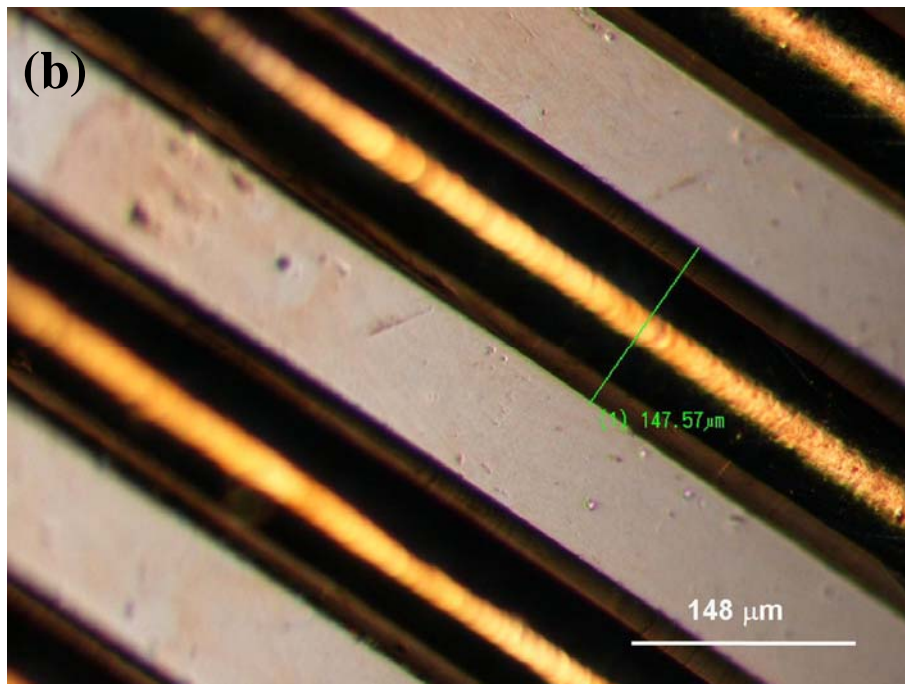
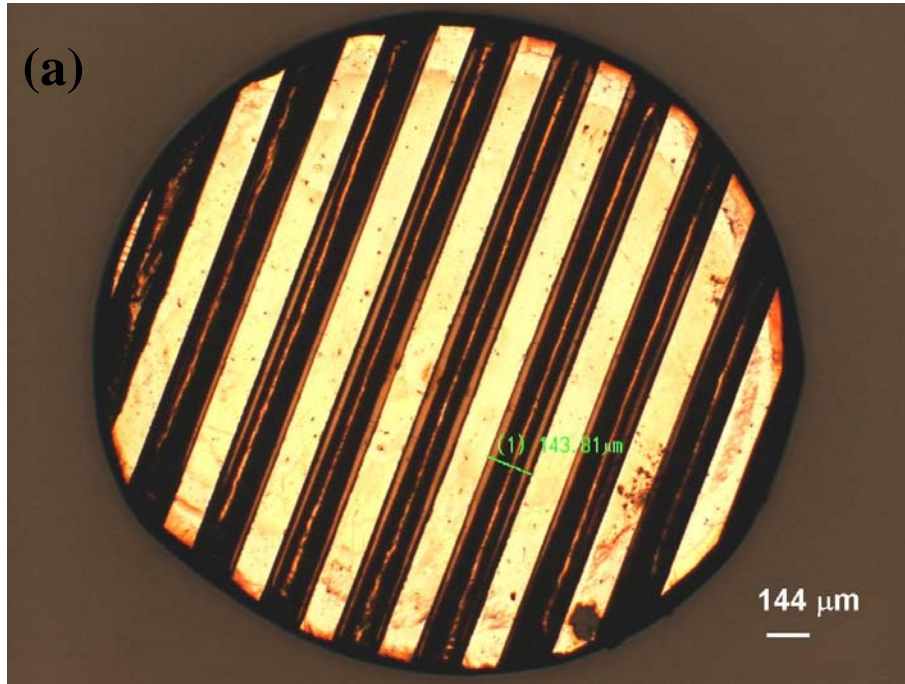


Figure 4.30 Replicated patterns by OM on the Au-based BMG materials imprinted at 177°C and 137 MPa for 5 min with (a) lower magnification by OM (b) higher magnification.

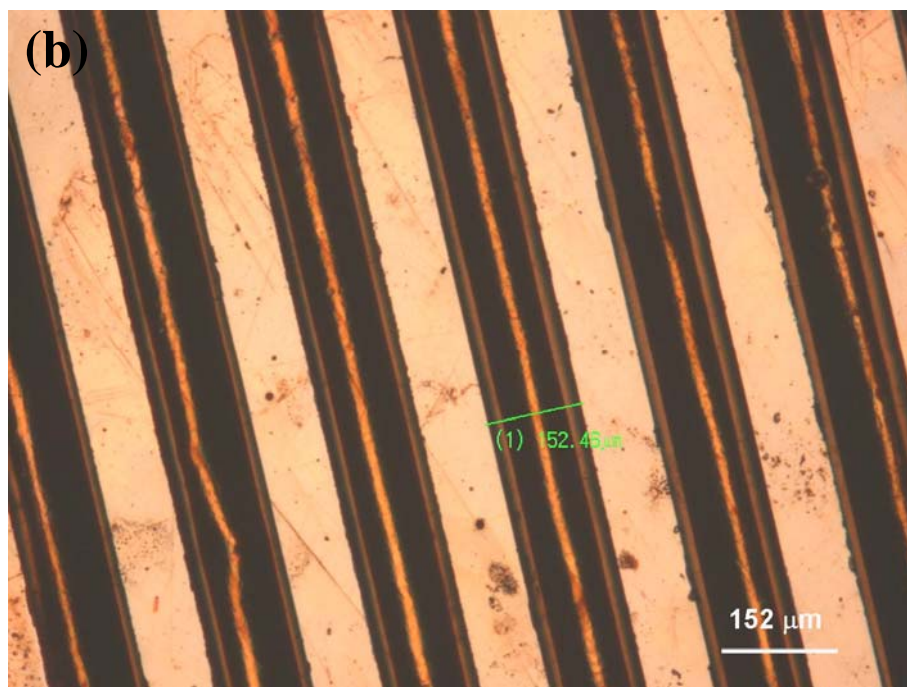
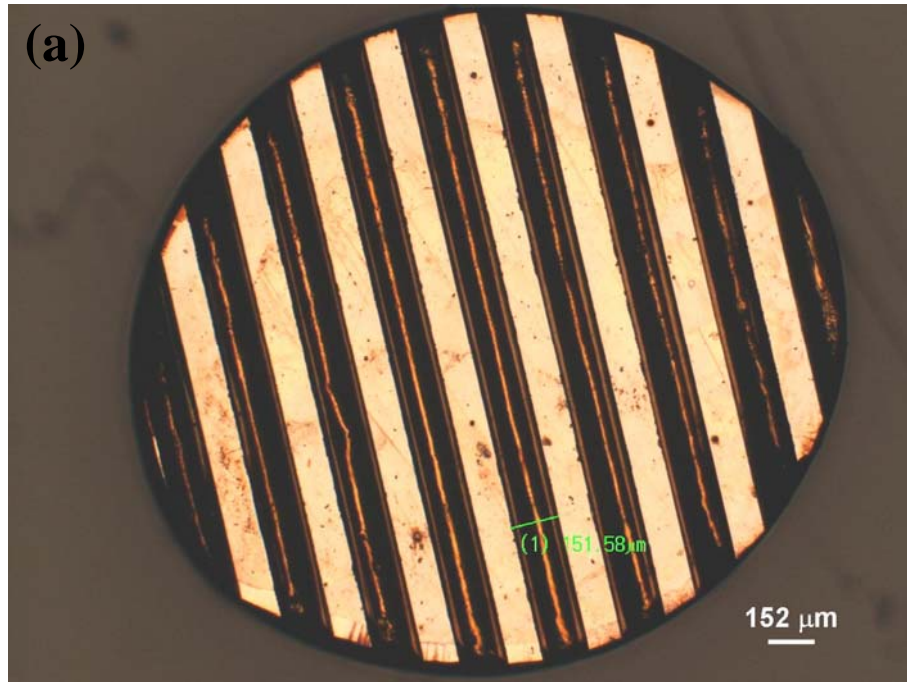


Figure 4.31 Replicated patterns by OM on the Au-based BMG materials imprinted at 177°C and 137 MPa for 10 min with (a) lower magnification by OM (b) higher magnification.

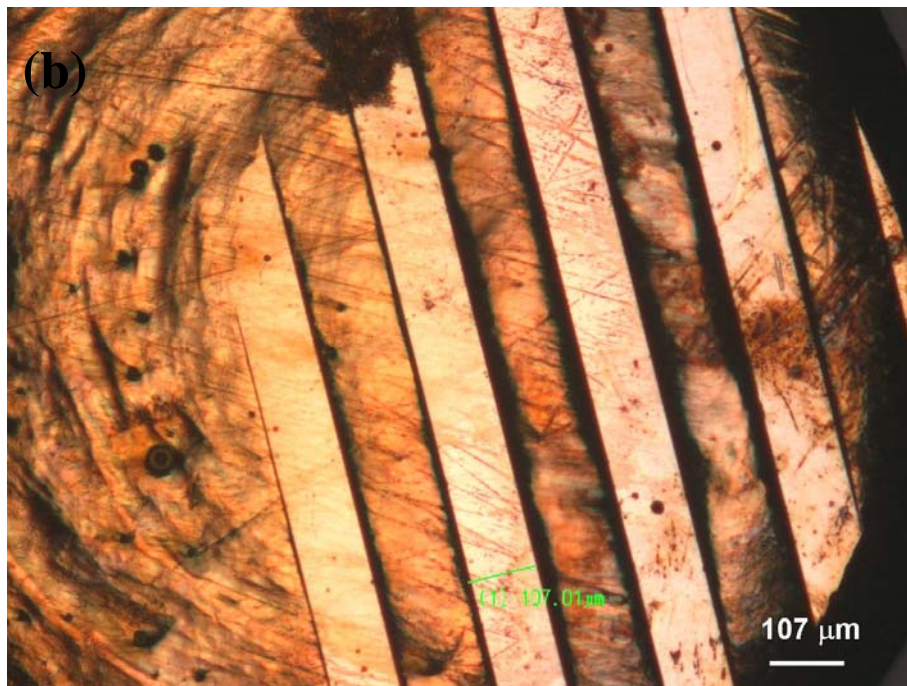
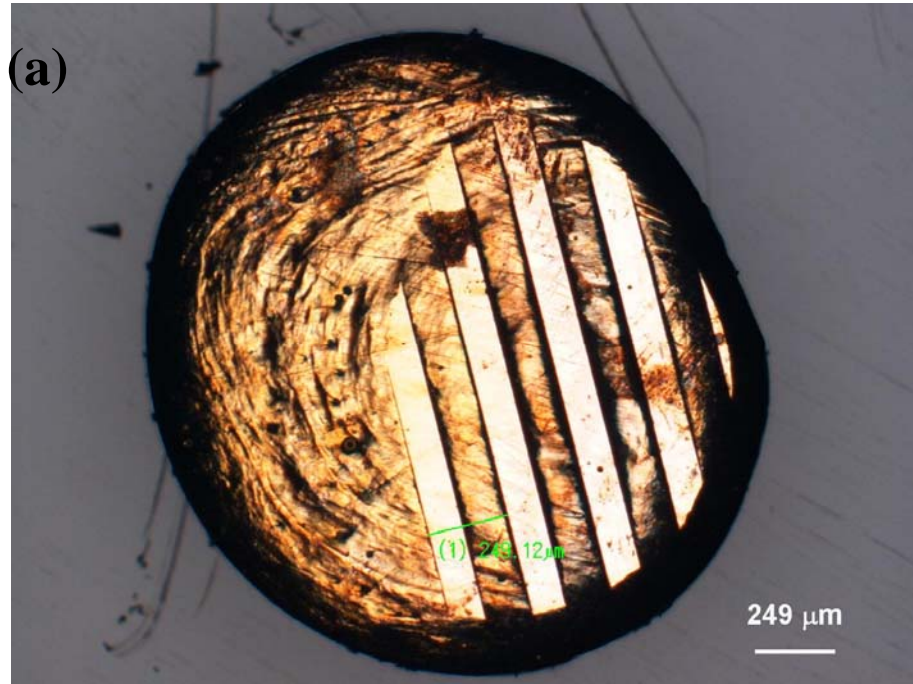


Figure 4.32 Replicated patterns by OM on the Au-based BMG materials imprinted at 177°C and 62 MPa for 10 min with (a) lower magnification by OM (b) higher magnification.

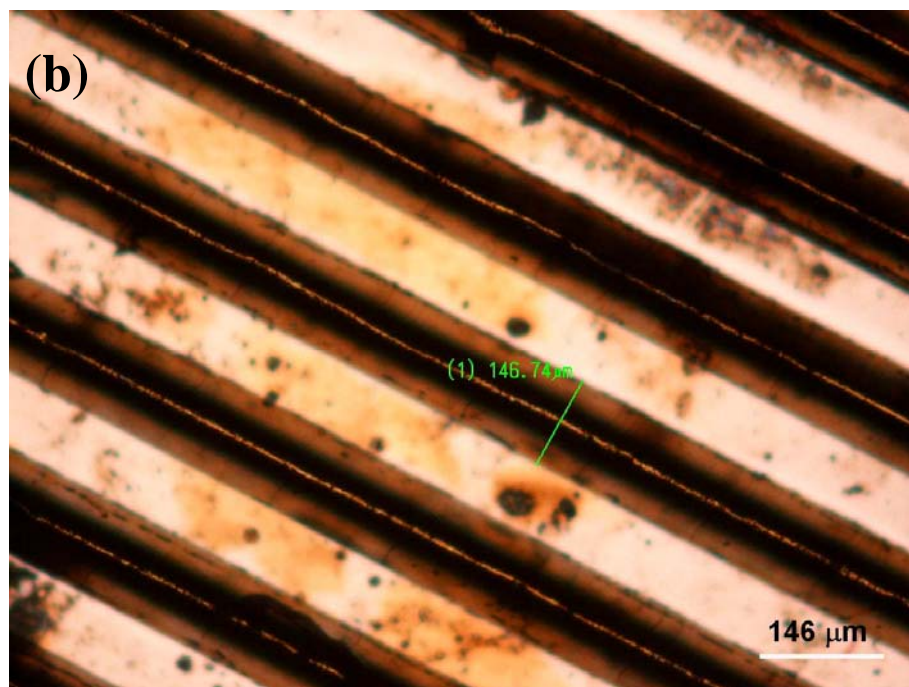
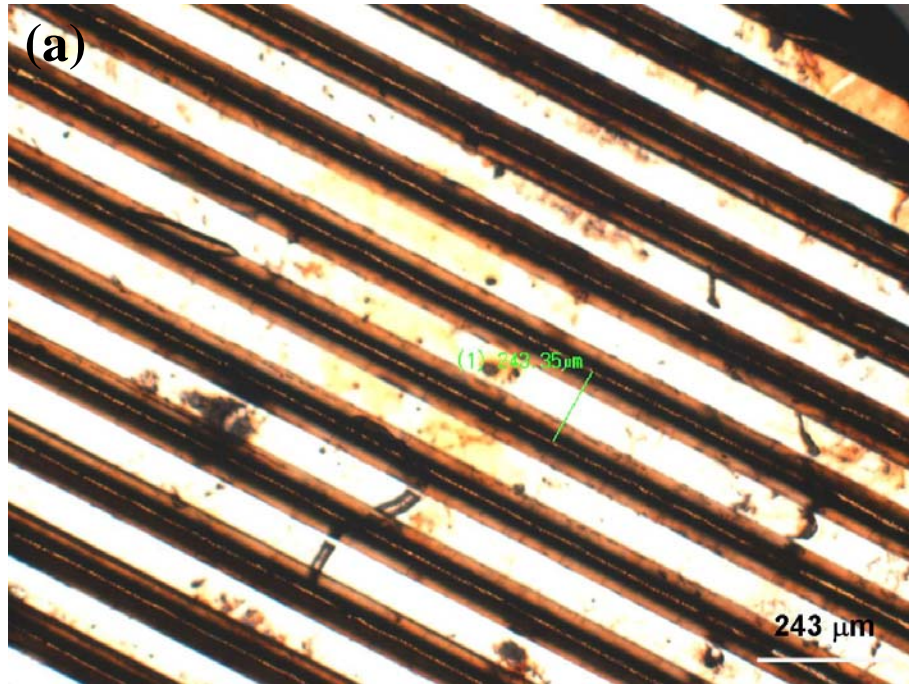


Figure 4.33 Replicated patterns by OM on the Au-based BMG materials imprinted at 177°C and 156 MPa for 10 min with (a) lower magnification by OM (b) higher magnification.

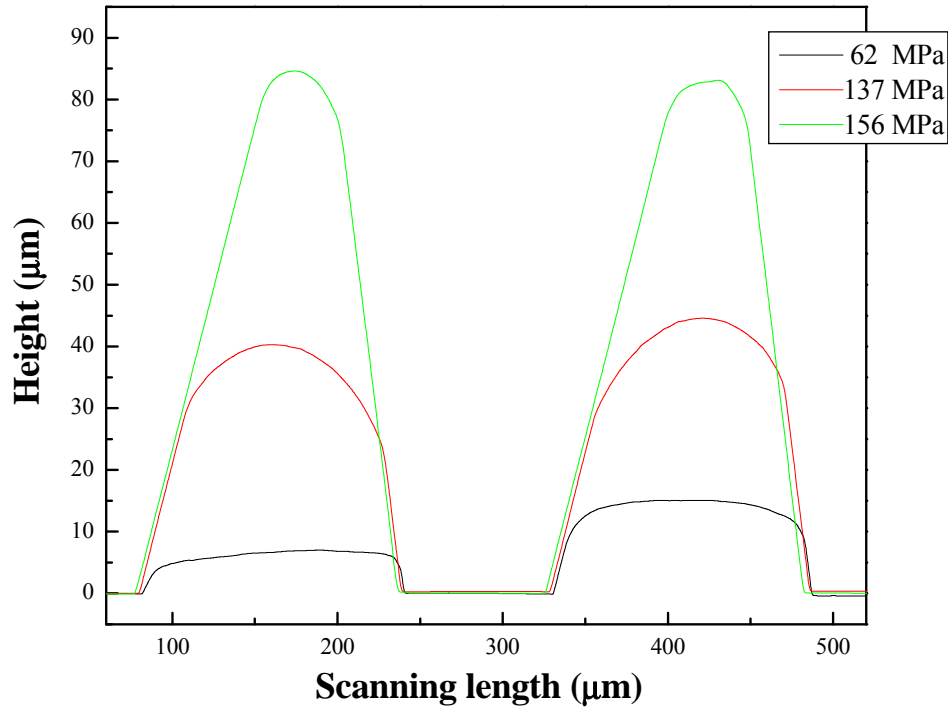


Figure 4.34 The morphological curves of V-groove imprinted Au-based BMG at 177°C and 62 MPa, 137 MPa, and 156 MPa, respectively, for 10 min by the α step.

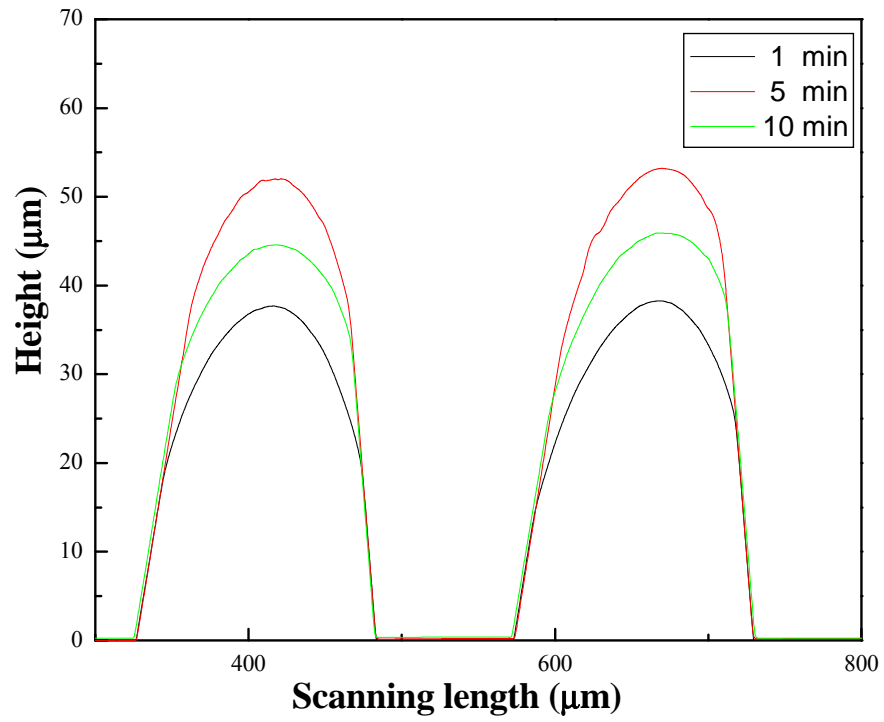
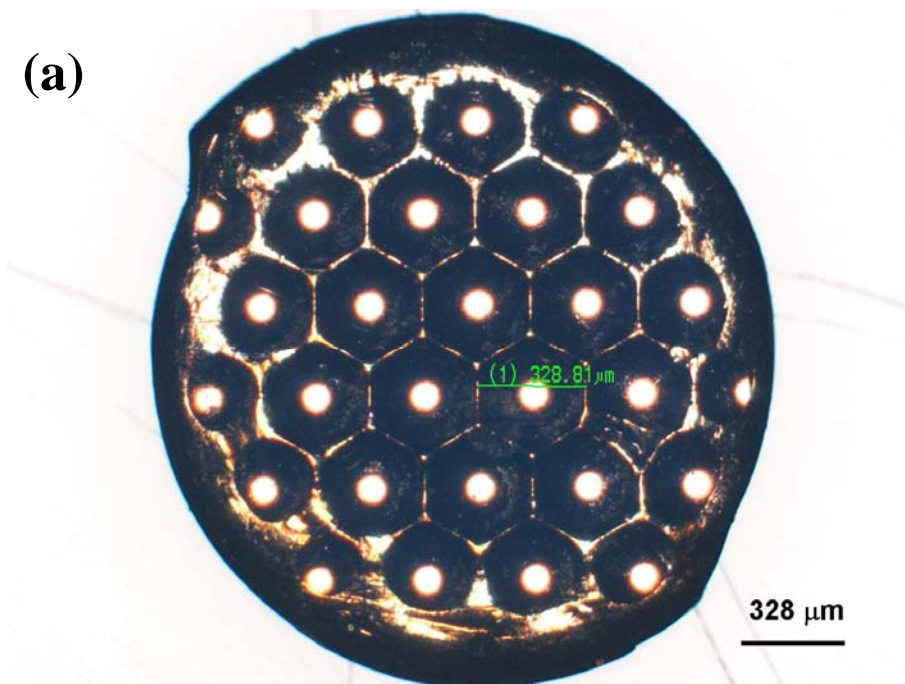


Figure 4.35 The morphological curves of V-groove imprinted Au-based BMG at 177°C and 137 MPa for 1, 5, 10 min, respectively, by the α step.



Figure 4.36 Replicated patterns by OM on the Au-based BMG materials imprinted at 177°C and 28 MPa for 10 min.

(a)



(b)

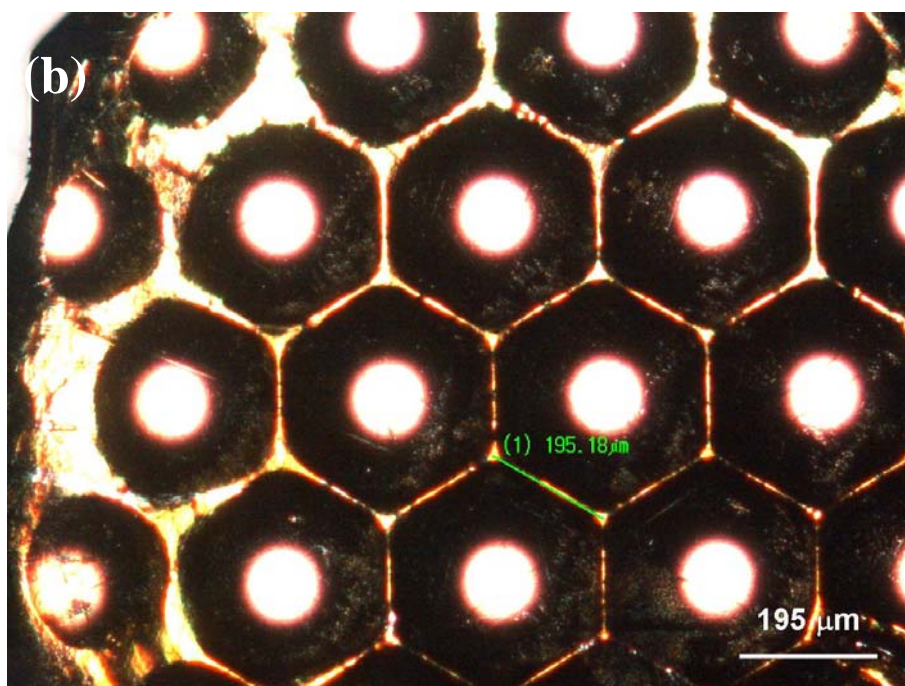


Figure 4.37 Replicated patterns by OM on the Au-based BMG materials imprinted at 177°C and 62 MPa for 10 min with (a) lower magnification (b) higher magnification .

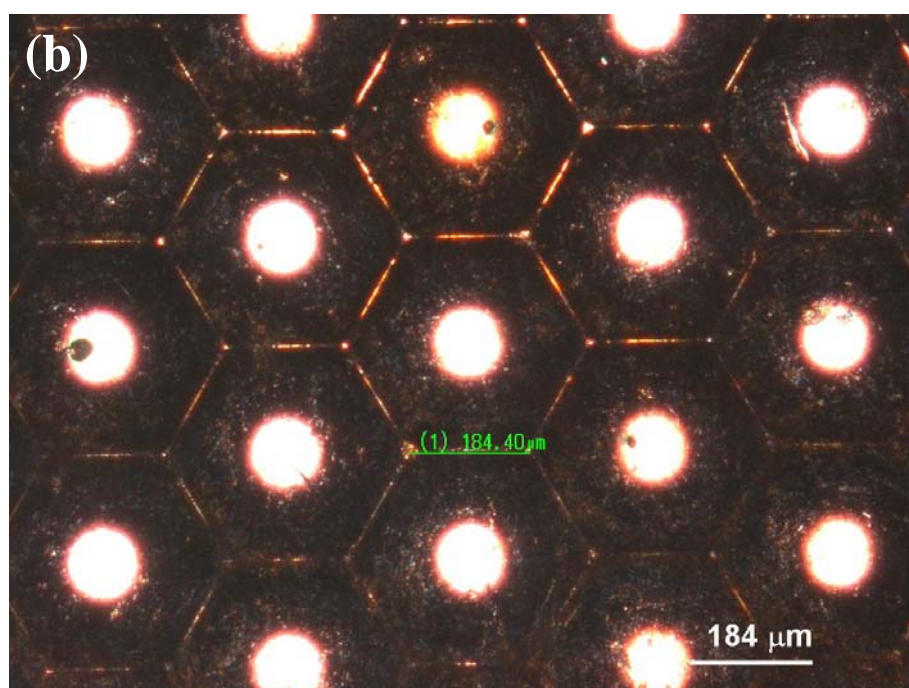
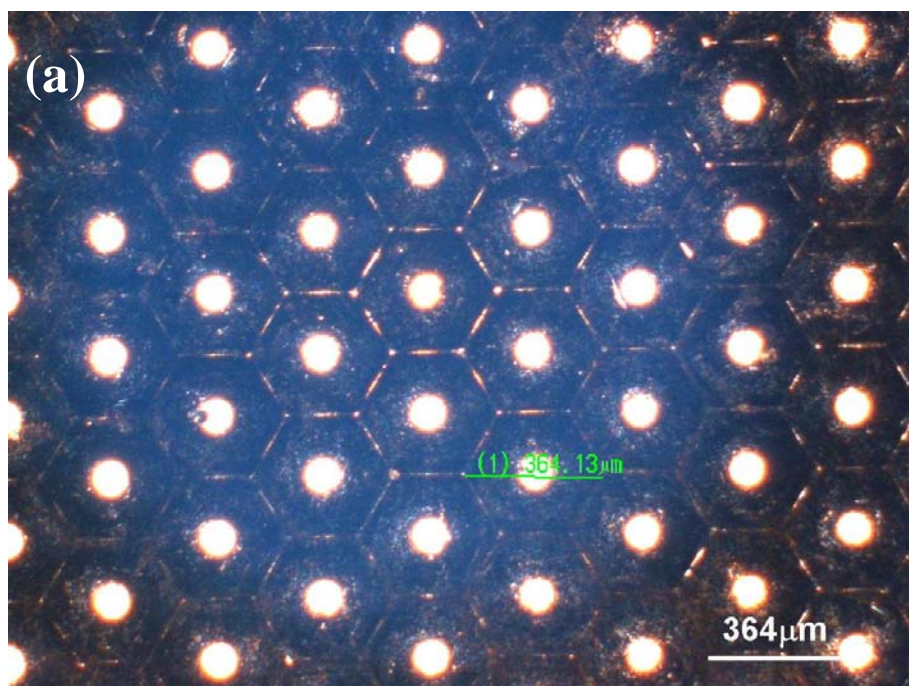


Figure 4.38 Replicated patterns by OM on the Au-based BMG materials imprinted at 177°C and 156 MPa for 10 min with (a) lower magnification (b) higher magnification .

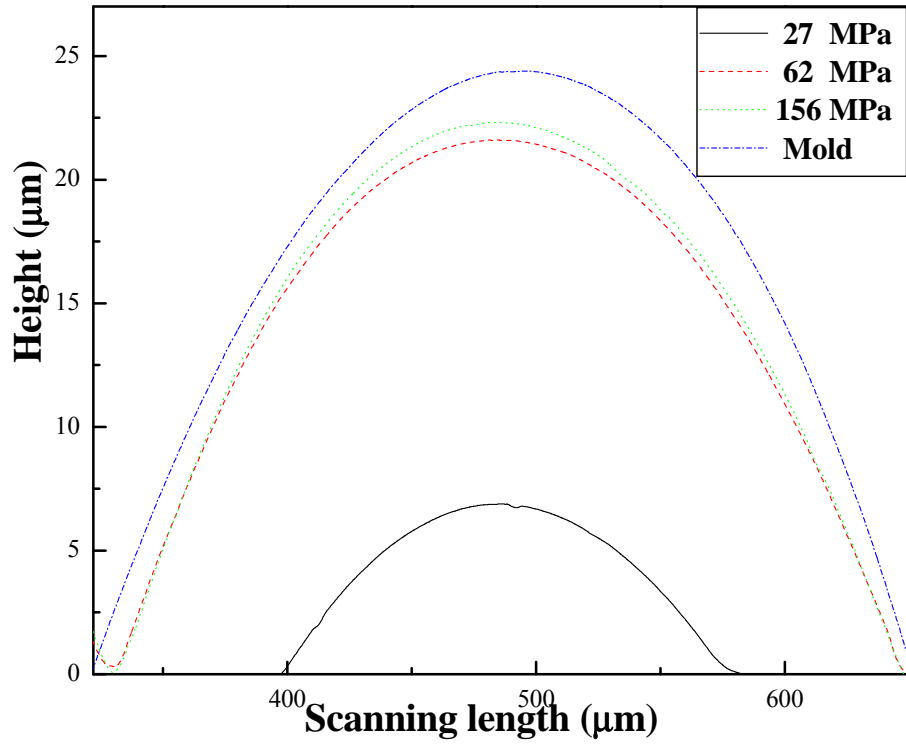


Figure 4.39 The morphological curves of micro-lens array on the Au-based BMG at 177°C and 27 MPa, 62 MPa, and 156 MPa, respectively, for 10 min by the α step.

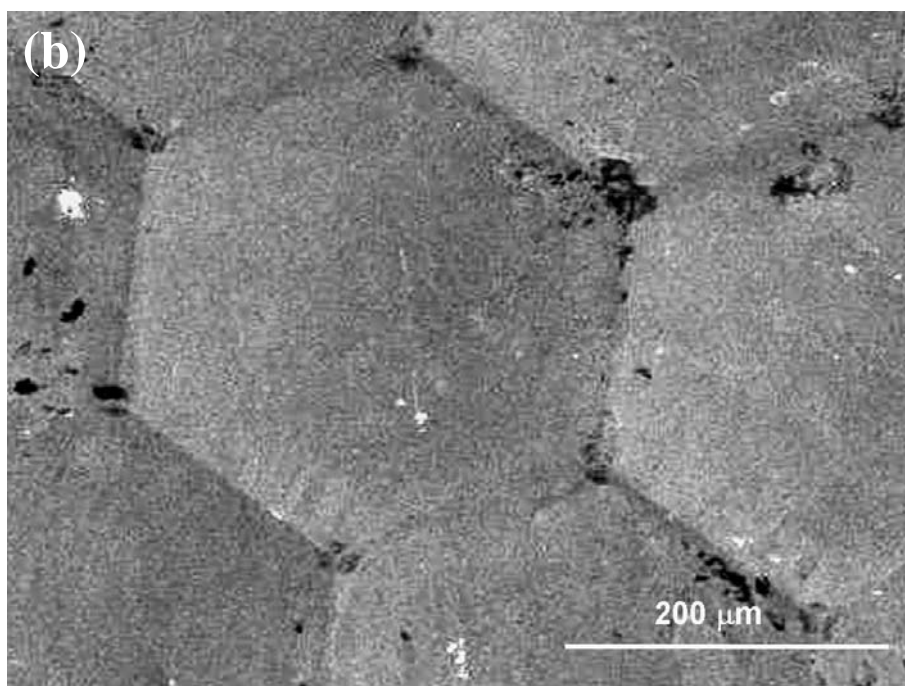
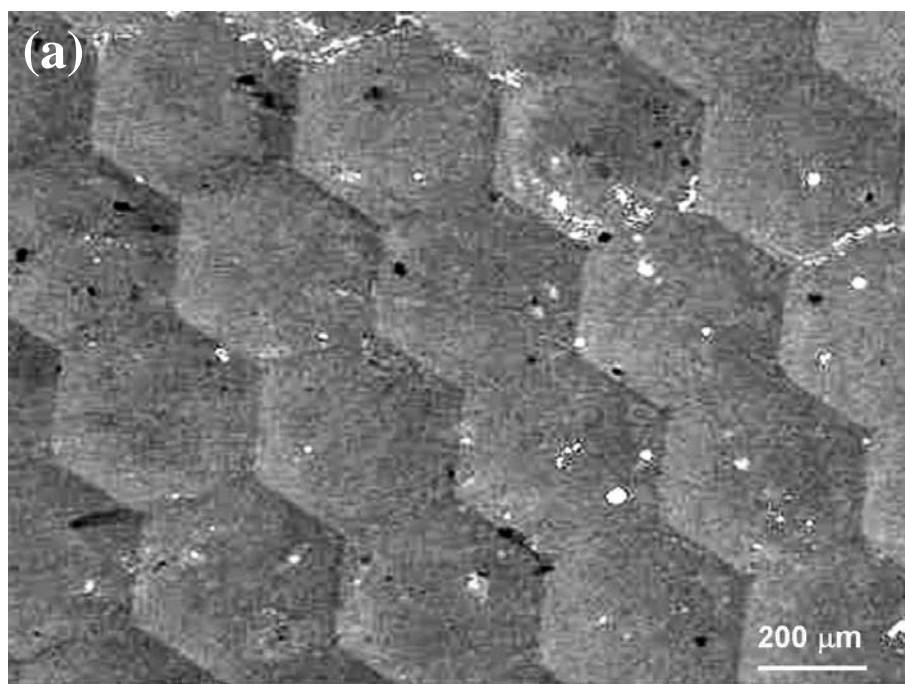


Figure 4.40 Replicated patterns by SEM on the Au-based BMG materials imprinted at 177°C and 156 MPa for 10 min with (a) lower magnification (b) higher magnification.

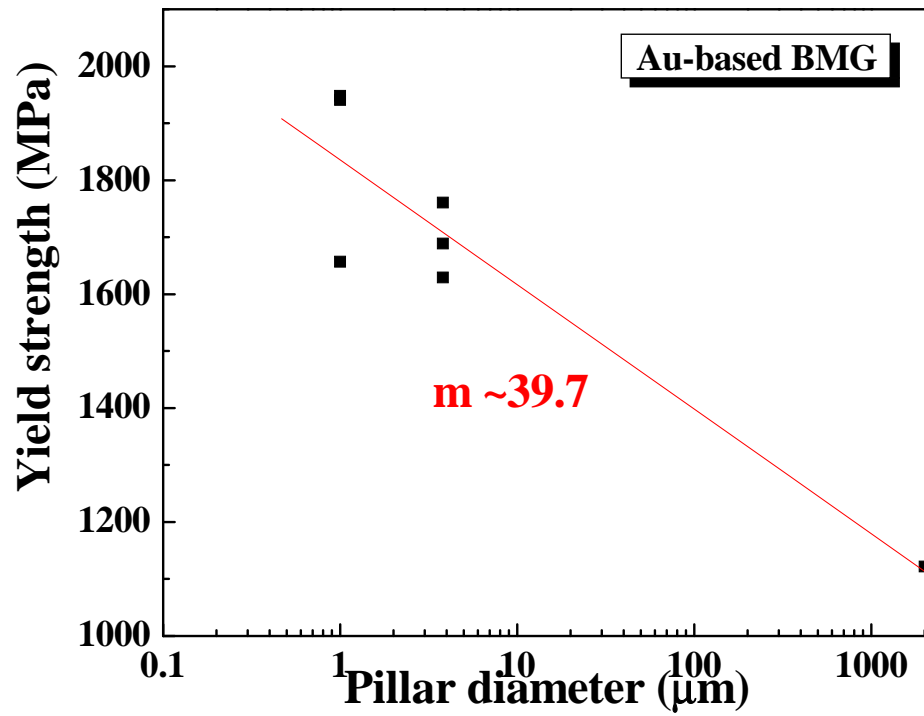


Figure 5.1 The strength-sample size relationship for the Au-based BMG with different pillar diameters from 2 mm down to 1 μm .

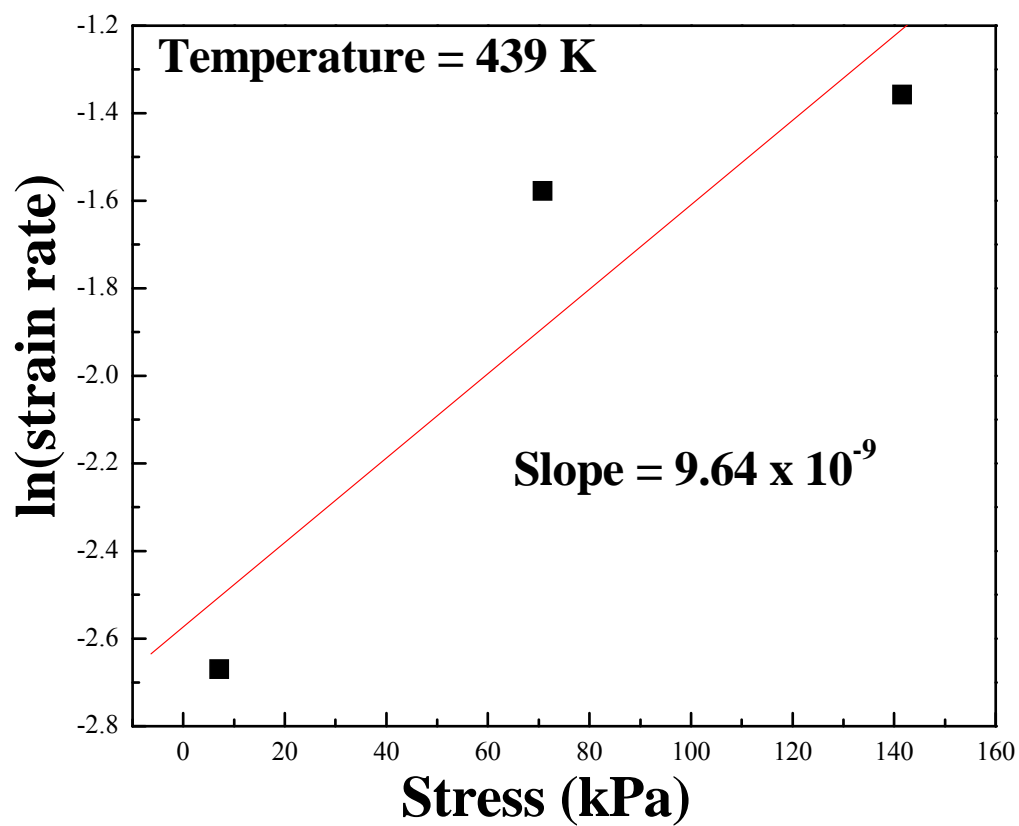


Figure 5.2 Determination of the STZ size of the Au-based alloys based on the TMA data.

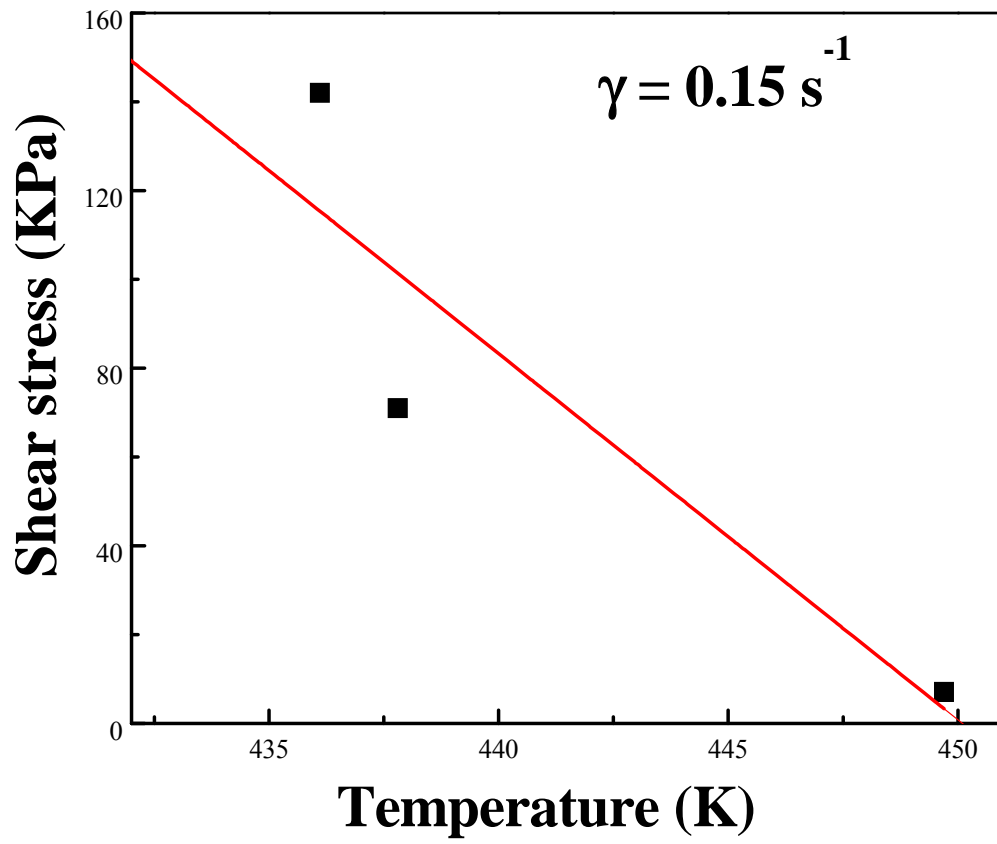


Figure 5.3 Extraction of the activation energy of the Au-based BMG during shear deformation within the supercooled temperature region.

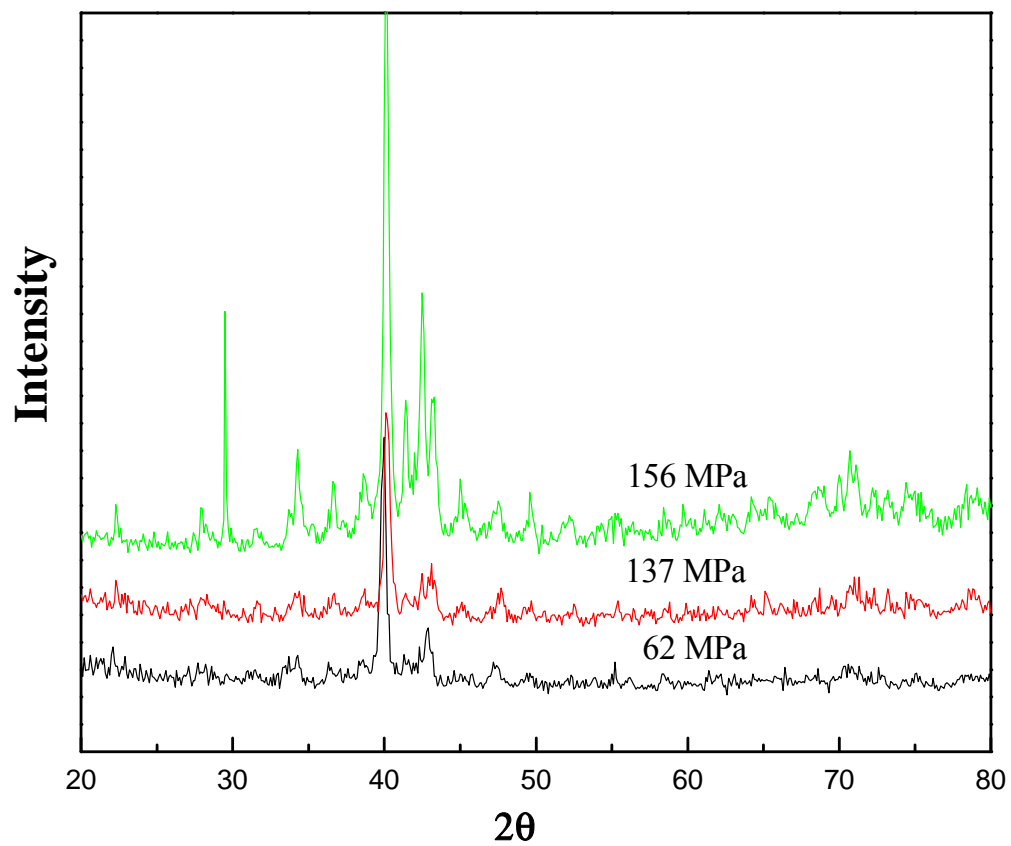


Figure 5.4 XRD pattern of the hot embossing Au-based BMG with different pressures 62 MPa, 137 MPa, and 156 MPa, respectively.